Infrared Spectroscopy and Monte Carlo Simulations of Doped Helium Nanodroplets

by

Kale Edward King

(Under the Direction of Gary Douberly)

Abstract

Helium nanodroplets isolation has been used to isolate the *n-*, *s-*, *i-*, and *tert*-butyl radicals in a minimally perturbative environment. The infrared spectra of these radicals were gathered in the CH stretching region of $2750-3125$ cm^{-1}. These spectra represent the first high-resolution spectra of *s*-butyl radical. The experimental spectra of all butyl radicals were compared to spectra modeled with a VPT2+K treatment of CCSD(T) quartic force fields, in order to assign the experimental vibrational bands. The experimental spectra were also used as a comparison to local mode computed spectra, in order to evaluate the extensibility of local mode treatments to the computed harmonic spectra of larger hydrocarbon radicals. In a separate investigation, Monte Carlo electrostatic deflection simulations of droplets doped with oligomers of hydrogen cyanide were carried out. These simulations indicated the ability of static, inhomogenous electric fields to deflect a beam of doped droplets in a size-specific manner. This indicates that construction of an instrument to separate a beam of droplets by size and probe droplet-size dependent effects on the dopant molecules is feasible.

Index words: [Helium Nanodroplet Isolation, Butyl Radical, Infrared Spectroscopy, Doped Nanodroplets, Inhomogenous Electric Fields, Monte Carlo Simulation]

Infrared Spectroscopy and Monte Carlo Simulations of Doped Helium Nanodroplets

by

Kale Edward King

B.S., University of West Florida, 2016

A Dissertation Submitted to the Graduate Faculty of the
University of Georgia in Partial Fulfillment of the Requirements for the Degree

Doctor of Philosophy

Athens, Georgia

2022

Infrared Spectroscopy and Monte Carlo Simulations of Doped Helium Nanodroplets

by

Kale Edward King

Major Professor: Gary E. Douberly

Committee: Michael A. Duncan

Melanie A. R. Reber

Electronic Version Approved:

Ron Walcott

Vice Provost for Graduate Education and Dean of the Graduate School

The University of Georgia

August 2022

Dedication

To G-Pop, Papa, Susan, and John. I miss you, and I hope I've made you proud.

Acknowledgments

First, I would like to thank my parents, Chris and Shelly. Mom: you gave me the love of books and learning, and taught me that there is inestimable value in a deep breath and a second look at a problem. Dad: you taught me how to work with my hands and that there is no skill that cannot be learned. What I learned from you both gave me the strength to reach where I am today. You have been unfailingly supportive through all the struggles and doubts that grad school brings. Thank you.

To Gary: thank you for bringing me into your lab. You gave me the latitude to build, break, or fix anything I could get my hands on. You also gave me the push to think and work beyond the purely experimental box I had placed myself in. I thank you for your guidance and for the faith you put into me and my work.

I would like to thank the members of the Douberly group, past and present. Joe: I think I learned more working with you, scraping our knuckles on vacuum pumps and mass spectrometers than I ever could have imagined before coming here. Alaina: I don't think I could have hoped for a better guide to working our instruments, even if someone else did set one of them on fire. Greg: I cannot thank you enough for the work we did together on the butyl radicals project. Travis: it was wonderful having someone to join the group alongside of and work with through the ups and downs of five-and-a-half years. To Ronald and Sachin, I would like to thank you for putting up with my rambling way of teaching and to pass on the instructions Joe gave to me: keep your boss in line and get graduated! I would like to give a special thanks to Peter Franke, who was and is a wonderful friend and colleague: you taught me the value of computational chemistry, good tea, and industrial music. For all these (and many more) I will always be grateful.

My thanks also go out to the graduate students in other labs that I found myself spending so much time with, particularly Nick and Walker from the Reber group, as well as Jason, Josh, and Brandon from the Duncan group. You all were wonderful friends and colleagues, and I am grateful for the times we spent together inside and out of the labs, good and bad, from late-night Deadlands games to the curious *indoor* rain that struck our labs in the winter of 2018.

I would also like to thank the mentors and instructors from my undergraduate years. Many thanks to Tim Royappa, who set me onto the path of becoming a chemist in the first place. My thanks also to Pamela Tanner, who gave me the first taste of instructing undergraduates, which would prove so useful in my as a lab instructor. I would like to give particular thanks to Chris and Karen Molek, who not only brought me into their respective labs and taught me many of the skills that have helped me immeasurably in my time here in graduate school, but also gave me the push and opportunity to think beyond a classroom or university building.

Contents

Chapter 1

Introduction

1.1 Superfluids Under the Old Regime

Liquid helium has been known since 1908, with Heike Kamerlingh Onnes reporting the first condensation of helium after a 13 hour odyssey with a six-stage cooling apparatus [1]. Given the sub-2 K temperatures reached, it is likely that this first condensation of liquid helium was also the first generation of superfluid helium, He II (as opposed to the higher-temperature, non-superfluid He I), though such a description would take another thirty years to develop.

1938 saw a flurry of activity around the discovery of the abnormally low viscosity of liquefied helium and the identification of superfluidity. Kapitza's research in Moscow [2] and Allen and Misener's research in Cambridge [3], simultaneously published, are usually credited with direct measurements of the viscosity of He II. A slew of other properties of this novel material were described in the short months afterward, from the fountain effect [4], to the flow of He II across surfaces. [5, 6].

Theoretical descriptions of superfluidity followed within the year. Less than two months after the experimental discovery was published, Fritz London offered a description of He II's behaviour as a product of degeneracy in a Bose-Einstein condensate [7]. Laszlow Tisza developed this idea into the "two-fluid" model (though this particular turn of phrase was not yet coined), in which he described the exchange of He II and standard liquid helium at interfaces where heat enters a liquid bath [8].

Probably the most famous personality associated with theoretical models of He II was Lev Landau. It was a near-run thing that Landau was able to contribute to the theory of superfluidity at all; in March of 1938, as London and Tisza were putting forth their descriptions of the two-fluid model in France, the Great Terror (in Russian the "Yezhovschina") was upending Soviet science and society [9]. Landau was arrested early that same March by the NKVD, the Soviet Union's infamous political police, on charges of "counter-revolutionary activity" and for possession of a leaflet critical of the Politburo [10]. After Landau had spent a year in a Moscow prison, Kapitza was able to secure his release, with the patronage of Vyacheslav Molotov and on the condition that he work with Kapitza on studies of low-temperature helium [11].

Landau would go on to describe his own [12] theory of the superfluidity of He II (in another brush with Stalin-era tragedy, his work would be received in the West a day after the German invasion of the Soviet Union). His model built off Tisza and London's two-fluid model with a major distinction: he made no mention of a Bose-Einstein condensate, instead introducing the concept of the non-superfluid component as a collection of phonons and rotons excited from the superfluid component. Additionaly, the Landau model describes a monotonic relation between the temperature of a He II system and the superfluid fraction, bounded by 100% superfluid at absolute zero and 100% "normal" fluid at the He I/He II phase transition. By 1949, two distinct and well-defined explanations of the behavior of liquid helium existed, with the applicability of Bose-Einstein statistics as the main point of contention [13, 14].

After the end of the second World War came the confirmation of the two-fluid model of He II. In 1946, Elpheter Andronikashvilli carried out an experiment with torsional pendulums submerged in He II, in which he measured the period of the pendulum at a series of temperatures below the transition from He I to He II [15]. Andronikashvili's later experiments detailed efforts to put the superfluid portion of a vessel of liquid helium into motion, from which it was determined that the superfluid behaved akin to a rotating solid object, rather than as a standard liquid with some measurable viscosity.

1.2 The Nanodroplet Revolution

The first detection of clusters formed from helium expanded into a vacuum ocurred in 1961 [16]. Later mass spectrometric study discovered magic numbers for helium clusters of various sizes that differed between ^{3}He and ^{4}He, perhaps suggesting some difference in condensation between nuclear species of helium [17]. A proper droplet beam was first reported in 1986 [18].

As superfluidity in He II had been historically described as a phenomenon in bulk material, question arose over whether clusters and droplets could be accurately described as a superfluid, and, if they could, at what size did they exhibit superfluid behavior. Early computational studies predicted finite-size clusters up to 728 atoms to exhibit properties similar to those in bulk liquid helium [19, 20]. Further theoretical studies determined evaporation rates of pure droplets at finite temperatures, predicting that droplets in the 100-10000 atoms in size evaporate very slowly, around one atom per thousand seconds, and predicted an internal temperature of $0.45\ K$ [21].

Infrared spectroscopy of sulfur hexafluoride in droplets of helium revealed an intriguing result: rather than having the broad character associated with vibrational transitions associated with molecules embedded in a traditional liquid or a more rigidly bound rare gas cluster, the $946\ cm^{-1}$ transition measured was rotationally resolved [22, 23]. Using a model of the system as SF_6He_8, with a helium atom at each octahedral face of SF_6 and fitting to the measured rotational bands gave measure to a rotational temperature inside the droplet of $0.37\ K$. These results put forth strong evidence of the superfluidity of helium droplets, at least those produced in expansions with average droplet sizes in the thousands of atoms. This evidence was strongly corroborated by the discovery of a phonon wing appearing approximately $6\ cm^{-1}$ to the blue of the $S_1 \leftarrow S_0$ electronic transition in glyoxal, representing a fundamental excitation of the superfluid droplet that would not have appeared in a normal fluid [24].

Possibly the most intriguing manifestation of superfluidity in small ^{4}He clusters came from the "Microscopic Andronikashvili Experiment." In this experiment, ^{3}He droplets were formed and doped with carbonyl sulfide (OCS). As increasing amounts of ^{4}He were doped in the ^{3}He/OCS systems, the vibra-

tional band of OCS at $2061.71\ cm^{-1}$ regained rotational resolution not seen in the droplets with only ^{3}He/OCS [25]. The onset of rotational resolution onset at 60 ^{4}He atoms, and only sharpened afterwards. This came as a strong experimental indication that superfluidity in helium was linked to its nuclear spin, as well as providing a size regime for the onset of superfluidity in collections of ^{4}He.

A great deal of the characterization and description of the processes in helium droplets comes from the experimentation of J.P. Toennies and his group at the Max Planck Institute in Gottingen. His group described the prototypical gas expansion source around which the majority of helium droplets are designed, down to the near-ubiquitous $5\ \mu m$ nozzle [26]. Toennies and co-workers categorization of the distinct pressure/temperature regimes, along with methods of ionization and charge transport inside droplets [27–29] would prove vital for later experiments on droplets, as would methods for and descriptions of the doping of foreign atoms and molecules inside droplets [30, 31].

1.3 What Can Be Done With Helium Nanodroplets?

The helium nanodroplet has been an incredible environment for exploring the chemistry and physics of a wide variety of systems. This ranges from the construction of metal nanoparticle catalysts [32], to the spectroscopy of large biomolecular ions [33], to investigations of bimolecular reactions [34], to myriad more studies that exploit or probe the unique properties of the nanodroplet environment. The focus of this thesis involves infrared spectroscopy of hydrocarbons and hydrocarbon radicals, as well as the droplet size dependent effects that arise in the range of small nanodroplets.

1.3.1 Infrared Spectroscopy in ^{4}He Nanodroplets

With these unique superfluid properties, low temperature, and transparency to all light short (or perhaps long) of the vacuum ultraviolet, nanodroplets have proven fertile ground as a matrix for spectroscopy [35]. Where solid, rare-gas matrices may produce noticeable cage effects on products trapped within them, significantly shifting band origins and perturbing rotational structure, helium nanodroplets offer a partic-

ularly "soft" environment to trap and probe molecular species. The pick-up process by which droplets are doped also allows for the construction of tailored molecular or radical systems, such as radical peroxides [36], that would otherwise be difficult to form.

Nanodroplets have been particularly useful for studies of hydrocarbon radicals. These radicals often have quite complex spectra as a consequence of unpaired electrons and the bevy of interactions that can occur with such [37]. The spectra can be complicated even further by the many rotational states accessible even at moderate temperatures. Doping these radicals into droplets greatly reduces the complexity of these spectra by dissipating the bulk of rotational excitations and acting as a $0.37\ K$ cryostat [38]. This low temperature inside the droplet also halts many of the breakdowns, rearrangements, and reactions that have historically complicated the matrix-isolation spectra of hydrocarbon radicals [39]. Infrared spectra of a range of these hydrocarbon radicals have been measured in helium nanodroplets, from the humble methyl radical, to larger ring structures, to complexes of radicals and oxygen molecules, and quite a bit in-between[35, 40, 41].

More extensive details of the trapping and action spectroscopy process, with emphasis on the vibrational spectroscopy of neutral radicals and closed-shell molecules are given in Chapter 2. The spectroscopy of C-H stretching in a particular set of hydrocarbon radicals, namely the butyl radicals, is given in Chapter 3, as well as the C-H stretching spectra of those alkenes that may contaminate the radical spectra.

1.3.2 Size-dependent Studies of Droplets

One of the outstanding questions around droplets involves the small perturbations they impart onto embedded molecules. In addition to the relatively minor (sub 0.1%) shifts to vibrational bands, a significant reduction of rotational constants, by a factor of 3-4 is known for molecules doped inside droplets [42]. This effect does not appear to be constant, however, in the range of small clusters of 1-100 helium atoms, nor does it converge to the value observed in larger droplets [43]. This leads to the question: at what cluster or droplet size does this effect converge?

An examination of this requires some method of selecting specific droplet sizes with a well-characterized dopant. This has been done previously through the expansion of seeded beams of carbonyl sulfide mixed into gaseous helium [44] and pickup of ^{4}He and carbonyl sulfide into ^{3}He droplets [25], but both of these methods have an effective upper limit of around 100 atoms, as it becomes difficult to narrowly specify a range of cluster sizes through these methods as average cluster size increases. Instead, it may be possible to separate these doped droplets through electrostatic deflection. Deflection of large droplets has been demonstrated before, through the action of inhomogeneous electric fields on doped droplets [45]. With fields of this kind, it may be possible to deflect a beam of small clusters and droplets in a size-dependent manner and probe specific droplet sizes spectroscopically. Chapter 4 details a computational investigation into the deflection of beams of hydrogen cyanide doped droplets and clusters through a recently developed electrostatic deflector, as a base for the design of an instrument.

References

(1) Dahl, P. F. Kamerlingh Onnes and the Discovery of Superconductivity: The Leyden Years, 1911-1914. *Hist. Stud. Phys. Sci.* **1984**, *15*, 1–37.

(2) Kapitza, P. Viscosity of liquid helium below the λ-point. *Nature* **1938**, *141*, 74.

(3) Allen, J. F.; Misener, A. Flow of liquid helium II. *Nature* **1938**, *141*, 75–75.

(4) Allen, J.; Jones, H. New phenomena connected with heat flow in helium II. *Nature* **1938**, *141*, 243–244.

(5) Daunt, J. G.; Mendelssohn, K. Transfer of helium II on glass. *Nature* **1938**, *141*, 911–912.

(6) Daunt, J.; Mendelssohn, K. Transfer effect in liquid helium II. *Nature* **1938**, *142*, 475–475.

(7) London, F. The λ-phenomenon of liquid helium and the Bose-Einstein degeneracy. *Nature* **1938**, *141*, 643–644.

(8) Tisza, L. Transport phenomena in helium II. *Nature* **1938**, *141*, 913–913.

(9) Figes, O., *The Whisperers : Private Life in Stalin's Russia*, 1st ed.; Metropolitan Books: New York, NY, 2007.

(10) Gorelik, G. The top-secret life of lev landau. *Sci. Am.* **1997**, *277*, 72–77.

(11) Pitaevskii, L. 50 years of Landau's theory on superfluidity. *J. Low Temp. Phys.* **1992**, *87*, 127–135.

(12) Landau, L. Theory of the Superfluidity of Helium II. *Phys. Rev.* **1941**, *60*, 356–358.

(13) Landau, L. On the Theory of Superfluidity. *Phys. Rev.* **1949**, *75*, 884–885.

(14) Tisza, L. On the Theory of Superfluidity. *Phys. Rev.* **1949**, *75*, 885–886.

(15) Andronikashvili, E. L.; Malmaladze, Y. G. Quantization of Macroscopic Motions and Hydrodynamics of Rotating Helium II. *Rev. Mod. Phys.* **1966**, *38*, 567–625.

(16) Becker, E.; Klingelhöfer, R.; Lohse, P. Strahlen aus kondensiertem Helium im Hochvakuum. *Z. Naturforsch. A.* **1961**, *16*, 1259–1259.

(17) Stephens, P. W.; King, J. G. Experimental Investigation of Small Helium Clusters: Magic Numbers and the Onset of Condensation. *Phys. Rev. Lett.* **1983**, *51*, 1538–1541.

(18) Buchenau, H.; Goetting, R.; Scheidemann, A.; Toennies, J. In *Conference Proceedings of the 15th International Symposium on Rarefied Gas Dynamics*, 1986, pp 197–207.

(19) Pandharipande, V. R.; Zabolitzky, J. G.; Pieper, S. C.; Wiringa, R. B.; Helmbrecht, U. Calculations of Ground-State Properties of Liquid ^{4}He Droplets. *Phys. Rev. Lett.* **1983**, *50*, 1676–1679.

(20) Sindzingre, P.; Klein, M. L.; Ceperley, D. M. Path-integral Monte Carlo study of low-temperature ^{4}He clusters. *Phys. Rev. Lett.* **1989**, *63*, 1601–1604.

(21) Brink, D.; Stringari, S. Density of States and Evaporation Rate of Helium Clusters. *Z. Phys. D* **1990**, *15*, 257–263.

(22) Fröchtenicht, R.; Toennies, J.; Vilesov, A. High-resolution infrared spectroscopy of SF6 embedded in He clusters. *Chem. Phys. Lett.* **1994**, *229*, 1–7.

(23) Hartmann, M.; Miller, R. E.; Toennies, J. P.; Vilesov, A. Rotationally Resolved Spectroscopy of SF_6 in Liquid Helium Clusters: A Molecular Probe of Cluster Temperature. *Phys. Rev. Lett.* **1995**, *75*, 1566–1569.

(24) Hartmann, M.; Mielke, F.; Toennies, J. P.; Vilesov, A. F.; Benedek, G. Direct Spectroscopic Observation of Elementary Excitations in Superfluid He Droplets. *Phys. Rev. Lett.* **1996**, *76*, 4560–4563.

(25) Grebenev, S.; Toennies, J. P.; Vilesov, A. F. Superfluidity Within a Small Helium-4 Cluster: The Microscopic Andronikashvili Experiment. *Science* **1998**, *279*, 2083–2086.

(26) Buchenau, H.; Knuth, E. L.; Northby, J.; Toennies, J. P.; Winkler, C. Mass spectra and time-of-flight distributions of helium cluster beams. *J. Chem. Phys.* **1990**, *92*, 6875–6889.

(27) Fröchtenicht, R.; Henne, U.; Toennies, J. P.; Ding, A.; Fieber-Erdmann, M.; Drewello, T. The photoionization of large pure and doped helium droplets. *J. Chem. Phys.* **1996**, *104*, 2548–2556.

(28) Buchenau, H.; Toennies, J. P.; Northby, J. A. Excitation and ionization of 4He clusters by electrons. *J. Chem. Phys.* **1991**, *95*, 8134–8148.

(29) Scheidemann, A.; Schilling, B.; Toennies, J. P. Anomalies in the reactions of helium(1+) with sulfur hexafluoride embedded in large helium-4 clusters. *J. Phys. Chem.* **1993**, *97*, 2128–2138.

(30) Scheidemann, A.; Toennies, J. P.; Northby, J. A. Capture of neon atoms by ^{4}He clusters. *Phys. Rev. Lett.* **1990**, *64*, 1899–1902.

(31) Lewerenz, M.; Schilling, B.; Toennies, J. P. Successive capture and coagulation of atoms and molecules to small clusters in large liquid helium clusters. *J. Chem. Phys.* **1995**, *102*, 8191–8207.

(32) Wu, Q.; Ridge, C. J.; Zhao, S.; Zakharov, D.; Cen, J.; Tong, X.; Connors, E.; Su, D.; Stach, E. A.; Lindsay, C. M.; Orlov, A. Development of a new generation of stable, tunable, and catalytically active nanoparticles produced by the helium nanodroplet deposition method. *J. Phys. Chem. Lett.* **2016**, *7*, 2910–2914.

(33) Thomas, D. A.; Chang, R.; Mucha, E.; Lettow, M.; Greis, K.; Gewinner, S.; Schöllkopf, W.; Meijer, G.; von Helden, G. Probing the conformational landscape and thermochemistry of DNA dinucleotide anions via helium nanodroplet infrared action spectroscopy. *Phys. Chem. Chem. Phys.* **2020**, *22*, 18400–18413.

(34) Lugovoj, E.; Toennies, J. P.; Vilesov, A. Manipulating and enhancing chemical reactions in helium droplets. *J. Chem. Phys.* **2000**, *112*, 8217–8220.

(35) Choi, M. Y.; Douberly, G. E.; Falconer, T. M.; Lewis, W. K.; Lindsay, C. M.; Merritt, J. M.; Stiles, P. L.; Miller, R. E. Infrared spectroscopy of helium nanodroplets: novel methods for physics and chemistry. *Int. Rev. Phys. Chem.* **2006**, *25*, 15–75.

(36) Franke, P. R.; Brice, J. T.; Moradi, C. P.; Schaefer, H. F.; Douberly, G. E. Ethyl + O2 in Helium Nanodroplets: Infrared Spectroscopy of the Ethylperoxy Radical. *J. Phys. Chem. A* **2019**, *123*, 3558–3568.

(37) Herzberg, G., *Molecular Spectra and Molecular Structure*, 2nd ed.; Prentice-Hall physics series; Van Nostrand: New York, 1950 - 1979.

(38) Toennies, J. P.; Vilesov, A. F. Superfluid Helium Droplets: A Uniquely Cold Nanomatrix for Molecules and Molecular Complexes. *Angew. Chem. Int. Ed.* **2004**, *43*, 2622–2648.

(39) Andrews, L. Infrared Spectra of Free Radicals and Chemical Intermediates in Inert Matrices. *Annu. Rev. Phys. Chem.* **1971**, *22*, 109–132.

(40) Brown, A. R.; Franke, P. R.; Douberly, G. E. Helium Nanodroplet Isolation of the Cyclobutyl, 1-Methylallyl, and Allylcarbinyl Radicals: Infrared Spectroscopy and Ab Initio Computations. *J. Phys. Chem. A* **2017**, *121*, 7576–7587.

(41) Leavitt, C. M.; Moradi, C. P.; Acrey, B. W.; Douberly, G. E. Infrared laser spectroscopy of the helium-solvated allyl and allyl peroxy radicals. *J. Chem. Phys.* **2013**, *139*, 234301.

(42) Callegari, C.; Lehmann, K. K.; Schmied, R.; Scoles, G. Helium nanodroplet isolation rovibrational spectroscopy: Methods and recent results. *J. Chem. Phys.* **2001**, *115*, 10090–10110.

(43) McKellar, A. R. W.; Xu, Y.; Jäger, W. Spectroscopic Studies of OCS-Doped 4He Clusters with 9-72 Helium Atoms: Observation of Broad Oscillations in the Rotational Moment of Inertia. *J. Phys. Chem. A* **2007**, *111*, 7329–7337.

(44) McKellar, A. R. W.; Xu, Y.; Jäger, W. Spectroscopic Exploration of Atomic Scale Superfluidity in Doped Helium Nanoclusters. *Phys. Rev. Lett.* **2006**, *97*, 183401.

(45) Merthe, D. J.; Kresin, V. V. Electrostatic Deflection of a Molecular Beam of Massive Neutral Particles: Fully Field-Oriented Polar Molecules within Superfluid Nanodroplets. *J. Phys. Chem. Lett.* **2016**, *7*, 4879–4883.

Chapter 2

Experimental Methods

2.1 Droplet Production

In the most general terms, helium nanodroplets are formed by the flow of high pressure (on the order of tens of bar), low temperature (from roughly five to forty-five Kelvin) helium through a pinhole nozzle into a vacuum. Two general schema of droplet production are known to arise in these conditions: the breakup of a liquid spray into droplets and the condensation of gaseous helium into droplets and clusters [1]. The breakup pathway produces a beam of droplets with a larger average size of $10^5 - 10^6$ He atoms, while the condensation pathway produces a smaller beam of $10^2 - 10^4$ He atoms [2]. The average size of a droplet in a beam (and, implicitly, the pathway to droplet formation) is determined by three factors: the diameter of the nozzle through which the helium flows into vacuum, the temperature of the nozzle, and the pressure the helium is held at before expansion [3]. Additionally, the velocity of the droplet beam is governed by the temperature of the nozzle: lower nozzle temperatures generate slower-moving droplets, while higher nozzle temperatures generate faster-moving droplets [4]. These usually fall within the range of $200 - 400\ \frac{m}{s}$, with an average distribution of $1 - 3\%$ of the beam velocity [5].

In practice, the diameter of the nozzle is rarely an intentionally varied parameter, most often being fixed at $5\ \mu m$, as is the case in the experiments detailed here. The temperature of the nozzle and the pressure of the helium upstream of it are more commonly varied to produce beams of the droplet size

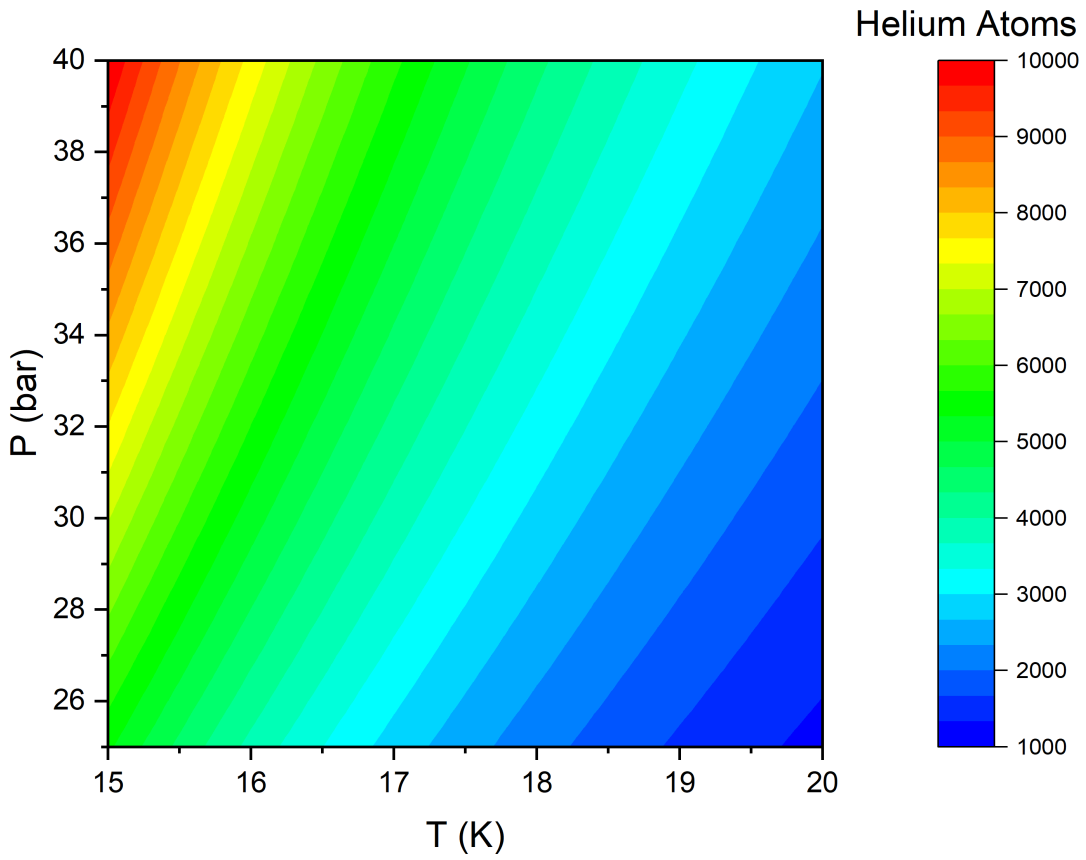

Figure 2.1: A two-dimensional surface of average droplet sizes within the scope of common temperatures and backing pressures for a $5\ \mu m$ nozzle, as computed with Paul Raston's Mathematica code [6].

desired. For the experiments detailed here, the nozzle temperature was adjusted by coupling a closed-cycle helium compressor/cold head system to the nozzle to chill the nozzle to a minimum of $12\ K$ and using a resistive heater to raise the nozzle to the desired temperature. The helium gas pressure was varied with a gas regulator upstream of the nozzle. The beams formed in the experiments detailed in the next chapter arose from the condensation of expanding gaseous helium, with an average droplet size on the order of 10^3 helium atoms.

The range of droplet sizes in a beam formed through the expansion of gaseous helium follow a log-normal distribution [7]. The probability distribution of a droplet containing any particular number of helium droplets can be modeled with the equation:

$$P(N) = \frac{1}{N\sigma\sqrt{2\pi}} \exp \frac{-(\ln N - \mu)^2}{2\sigma^2} \tag{2.1}$$

$$\bar{N} = \exp \mu + \frac{\sigma^2}{2} \tag{2.2}$$

$$\sigma = \ln \left[\left(\frac{S}{\bar{N}} \right)^2 + 1 \right]^{\frac{1}{2}} \tag{2.3}$$

$$\mu = \ln \bar{N} - \frac{\sigma^2}{2} \tag{2.4}$$

$$S = \exp \left(\mu + \frac{\sigma^2}{2} \right) \left(\exp \sigma^2 - 1 \right)^{\frac{1}{2}} \tag{2.5}$$

where N refers to the number of He atoms in a droplet, $\bar{N}$ represents the average number of He atoms in droplets in the beam, σ is the standard deviation of the natural logarithm of droplet sizes, μ is the mean of the natural logarithm of droplet sizes, and S is the variance of droplet sizes. The mean droplet size, $\bar{N}$, is governed by the empirical scaling law:

$$\ln \bar{N} = 2.44 + 2.55 \ln \Gamma \tag{2.6}$$

where Γ is a dimensionless parameter governed by the gas pressure, nozzle diameter, and nozzle temperature [6, 8].

2.2 Droplet Doping

Atoms, molecules, and clusters are doped into droplets through inelastic collision with droplets moving along the beam axis. Helium is not a particularly appealing solvent in absolute terms, but it is a much

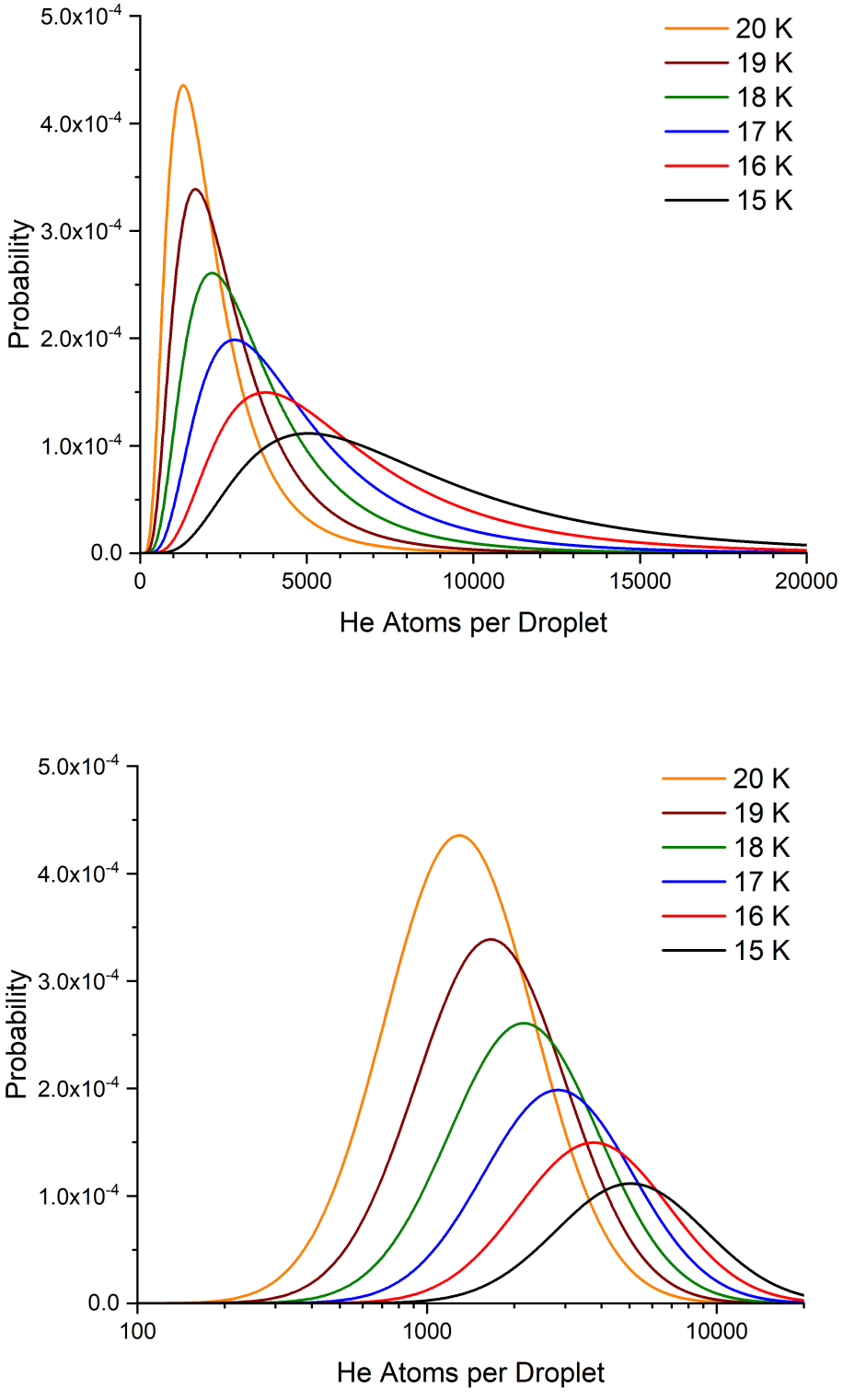

Figure 2.2: Droplet size probabilities at a small range of nozzle temperatures.

better solvent than vacuum, so particles that enter the droplet are trapped and carried with the droplet until its destruction [9]. If one can design a method to introduce a particle of interest into the path of the droplet beam, one can dope that particle into a droplet.

In the experiments conducted, two methods were used to introduce dopants of interest into the droplets. The first method involves the spray of pyrolysed products directly into the beam and will be detailed later. The second method, the "pick-up-cell," involves leaking a dopant gas into a differentially-pumped region along the axis of the beam and passing the droplet beam through this region. The pressure of the dopant in this region is controlled by a finely tunable metering valve and can be adjusted to introduce the desired number of dopants into the droplet. For droplet beams composed of droplets of moderate to large size, the number of dopant pick-ups can be modeled with a Poisson distribution,

$$P(k) = \frac{\lambda^k}{k!} e^{-\lambda} \tag{2.7}$$

where k represents the number of pick-up events [10]. The λ term represents a confluence of factors that and can be described as

$$\lambda(N) = \eta L \pi (2.22 N^{1/3})^2 \tag{2.8}$$

where η represents the density of gas in the pick-up region, L represents the length of the pick-up region, and the $\pi(2.22N^{1/3})^2$ term refers to the two-dimensional cross-section of the droplet as determined by N, the number of helium atoms in the droplet. It is then useful to combine these equations so that the pickup is determined as a function of both pickup number and droplet size

$$P(k, N) = \frac{(15.5 \eta L N^{2/3})^k}{k!} e^{-(15.5 \eta L N^{2/3})} \tag{2.9}$$

When pickup occurs, it results in the dissipation of the dopant's excited modes (electronic, vibrational, rotational, translational) through evaporation of He atoms off the surface of the droplet. These evaporating atoms carry off energy from the droplet-dopant system, maintaining an internal temperature of $0.37\ K$ within the confines of the droplet [11, 12]. Evaporation occurs when the excited modes of a

dopant transfer energy into excitations of the droplet itself, which eventually transfer energy to atoms on the droplet's surface. As one would expect, this quenches all modes not thermally populated at $0.37\ K$, bringing the dopant into its ground electronic and vibrational states, with only the first few, if any, rotational modes populated. When multiple pickups occur in the same droplet, clusters of dopants form at the center of the molecule [9, 10] and can then undergo further reactions, such as hydrogen bonding [13, 14] or barrierless reactions between radicals [15, 16].

2.3 Radical Formation through Pyrolysis

Since the helium droplet has been so successfully used in the trapping and analysis of radicals, it is useful to touch on the methods used to produce these radicals and introduce them into the droplets. The latter of these is fairly basic: radicals are introduced into the droplets by collision with the droplet beam. The process is rather similar to that which occurs in a pick-up-cell, with the caveat that the gaseous radicals are effusively sprayed into the vacuum chamber, rather than confined into a static region. When the orifice of the pyrolysis source is brought to the range of $0.5 - 2.5\ mm$ from the droplet beam at an approximately perpendicular orientation, the intersection of the droplet beam and the radical spray is great enough to dope a significant amount of the radical spray into the beam.

The production of radicals occurs through the thermolysis of gaseous precursor molecules trickling into a vacuum chamber the droplet beam is passing through. Two heated sources are used for this process: a quartz tube with tantalum wrapped around its exterior and a silicon carbide tube.

In the first, tantalum wrapped quartz, source, the pyrolytic action occurs when precursors come into contact with the heated quartz tube. The heating of the tube occurs when current is passed through the tantalum wire from two water-cooled copper electrodes, with one electrode attached to each end of the tantalum wire. Power is provided through a variable-output AC converter (colloquially known as a "variac") that is stepped-down by a factor of 10 and then passed through the electrodes and tantalum wire. The final current in the tantalum wire is variable in the range of $20 - 30\ A$, which heats the quartz to the

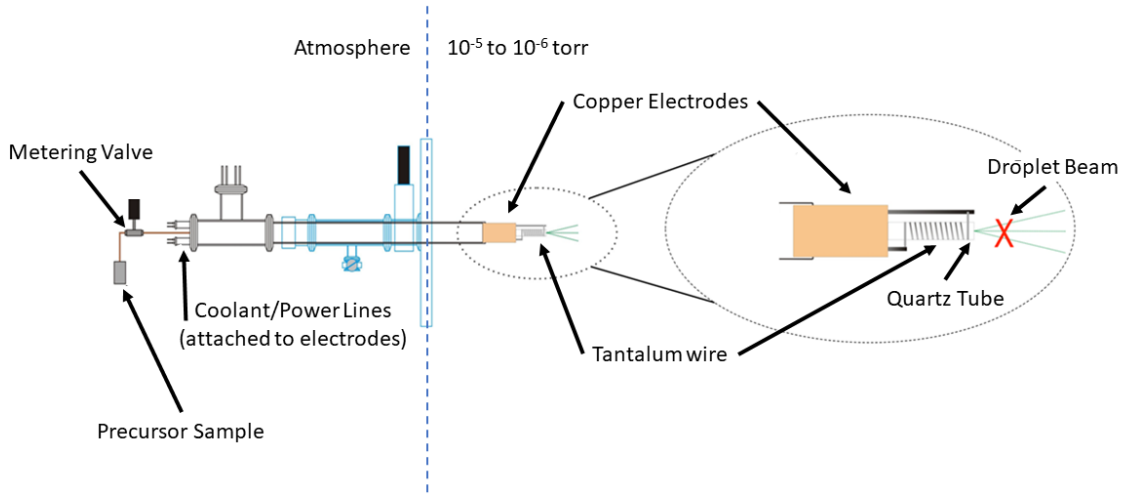

Figure 2.3: A diagram of the tantaum-quartz pyrolysis source. The red cross indicates the path of the droplet beam into the page.

range of $500 - 800\ K$. Precursor molecules are directed into this quartz tube with a smaller Teflon tube, which is is in turn attached to the precursor sample through a needle valve.

The second, silicon carbide, source also produces radicals through collision with a heated element, in this case the silicon carbide tube. The source is heated by directly passing current through the silicon carbide tube, which is attached to water-cooled copper electrodes. These electrodes are connected in series to a current-limiting resistor, which is connected to a variac. Precursors are introduced into this system through a needle metering valve connected to a stainless steel line, which connects to a quartz insulating tube, which then connects into the silicon carbide tube. The silicon carbide tube can reach temperatures of $1500\ K$ without degradation (and even higher temperatures immediately *before* degradation), which allows for the pyrolysis of a wide range of precursors.

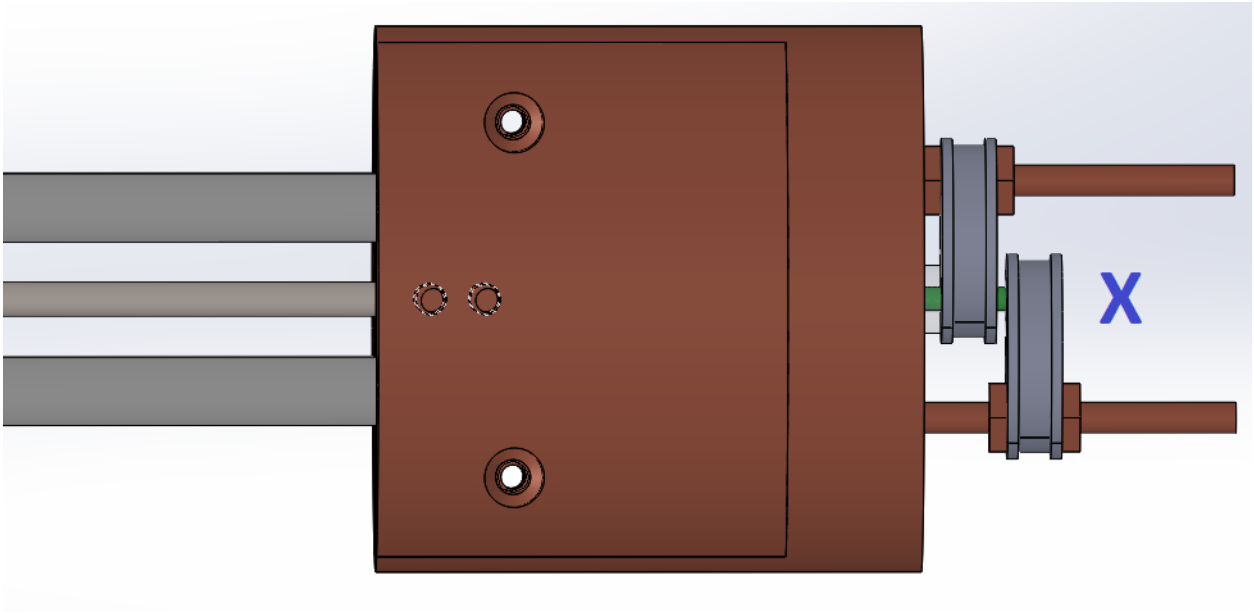

Figure 2.4: A CAD image of the silicon carbide pyrolysis source. The grey cylinder is the stainless tube the precursor is introduced through, the copper colored shapes are the water-cooled electrodes, and the green cylinder is the resistively-heated silicon carbide tube (color changed in this image for clarity). The blue cross represents the path of the droplet beam into the page.

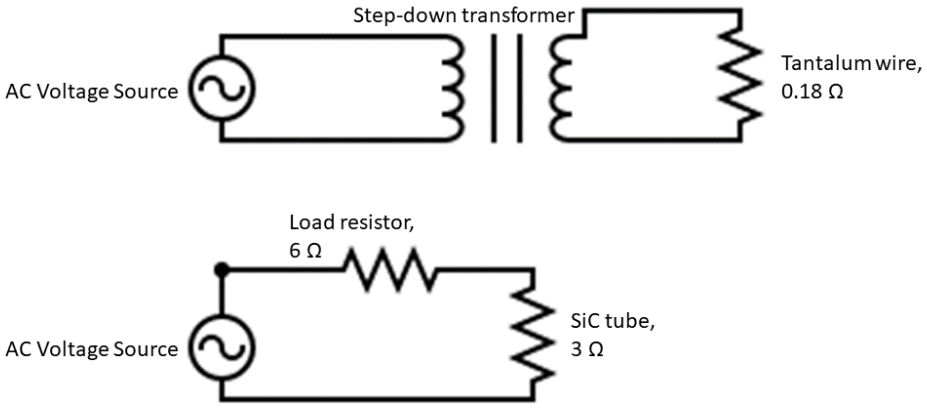

Figure 2.5: Circuit diagrams for the tantalum-quartz (upper) and silicon carbide (lower) sources.

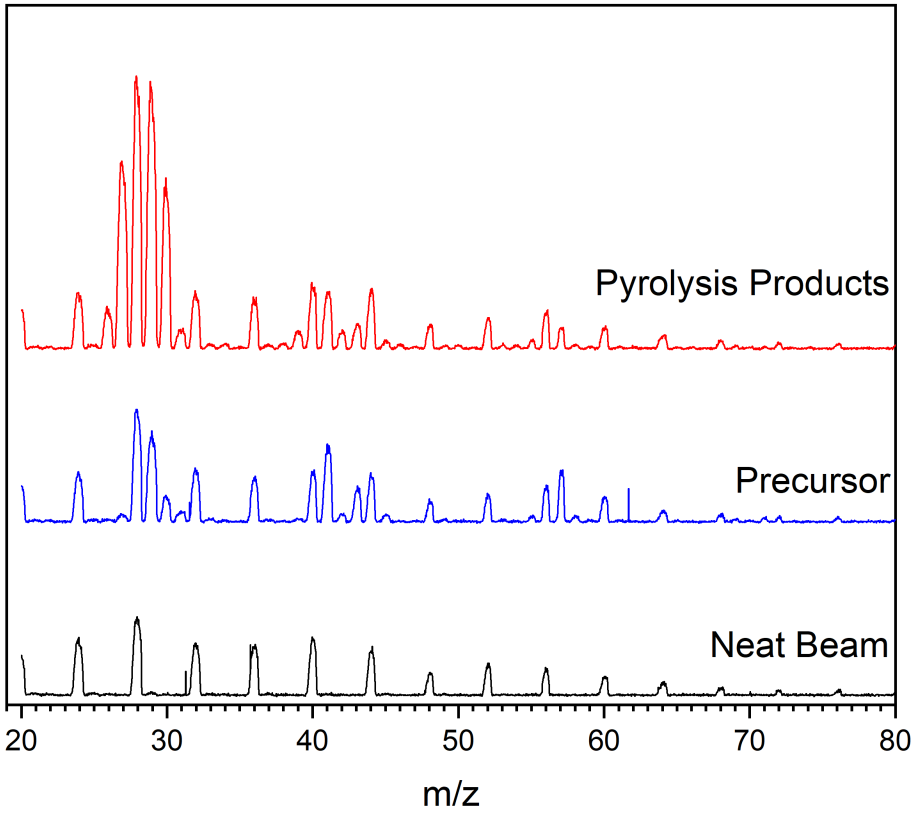

Figure 2.6: Mass spectra of a neat droplet beam, a beam doped with a nitrite precursor (n-pentyl nitrite), and a beam doped with the pyrolysis products of n-pentyl nitrite when passed through the tantalum-quartz pyrolysis source. The peaks that appear after pyrolysis correspond to new species created as the precursor breaks down. Monitoring one of those peaks that are associated with the radical of interest, such as 39 m/z, allows for species-selective spectroscopy, as detailed in the following sections.

2.4 Ionization of Droplets and Dopants

Doped droplets are usually analyzed by one of two methods: electron-impact mass spectrometry and helium cooled bolometers. The former method was the one used to collect spectra of butyl radicals and associated neutrals and will be discussed here. The helium bolometer method will be discussed in a later chapter, as it becomes relevant.

Helium droplets, like gaseous helium, can be ionized by photons or electrons of at least $24.6\ eV$ [17, 18]. This ionization occurs on the surface of the droplet, which then migrates through the droplet [2]. If the droplet is pure, a helium dimer cation will eventually form, which releases a substantial amount of energy, evaporating roughly $3 * 10^3$ helium atoms. This process can be observed in a mass spectrometer, such as in Figure 2.7, as a progression of peaks spaced 4 a.m.u. apart, representing a helium dimer cation with some number of helium atoms electrostatically bound to it. If the droplet has been doped, this charge has a chance to transfer to the dopant [19]. As the ionization potential of helium is usually much greater than that of the dopant, a substantial amount of excess energy is deposited into internal modes of the newly ionized dopant, which then transfer energy to and evaporate the rest of the droplet, with any leftover energy contributing to fragmentation of the dopant.

The size of a droplet has varied effects on the ionization of the droplet and any potential dopants. Larger droplets are less likely to transfer ionization to the embedded dopant, as the droplet has a greater amount of time to form He_2^+, which prevents charge transfer to the dopant [19]. Conversely, larger droplets are more likely to be ionized in the first place as a consequence of their larger geometric cross section [17]. In practice, a happy medium is found when the beam is composed of droplets with an average size of $2 - 5 * 10^3$ helium atoms.

2.5 Action Spectroscopy in Droplets

In the most general terms, action spectroscopy of dopants is effected by inducing evaporation of the droplet. This evaporation is induced by using a tunable light source to excite some transition in the dopant,

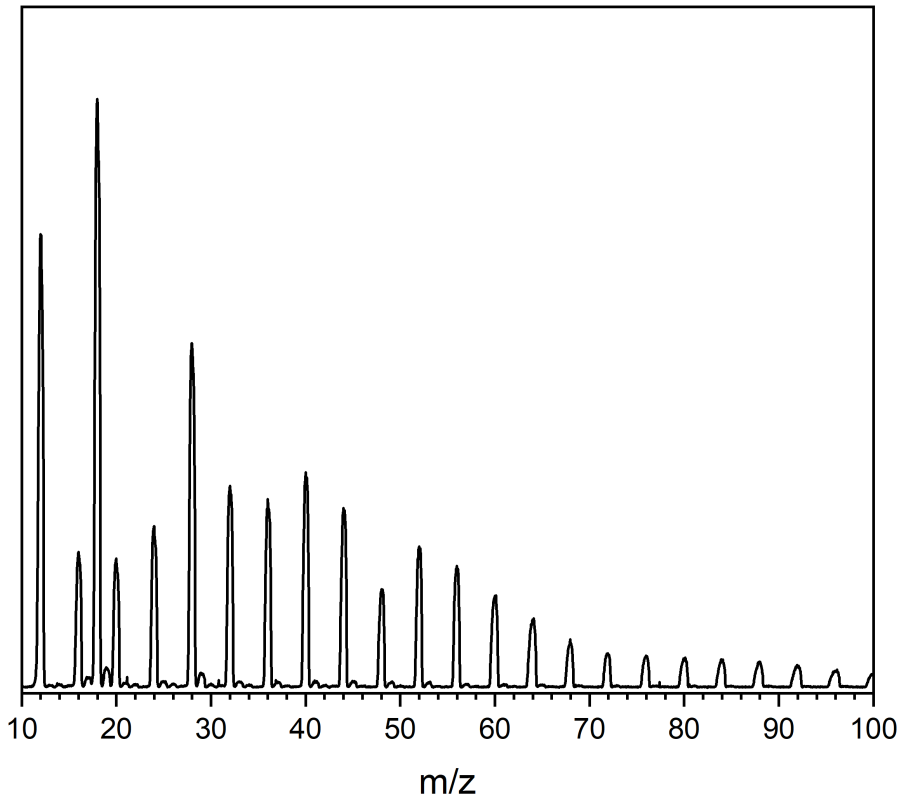

Figure 2.7: A mass spectrum of a beam of pure helium droplets, ionized through impact with 70 eV electrons. Note the evenly-spaced progression of peaks every 4 m/z. The peak at 18 m/z is from residual water in the vacuum system the spectrum was taken in.

which transfers energy into the droplet, which then evaporates helium atoms off the surface of the droplet and reduces the droplet's overall mass and geometric cross section [20]. For a moderate to large sized droplet most often used in a spectroscopy experiment, of roughly 1000 atoms or greater, the evaporation carries off $5\ cm^{-1}$ per atom, so that, for example, a $3100\ cm^{-1}$ vibrational excitation will lead to an evaporation of 620 helium atoms. As the size of a droplet and its signal on the detector are directly related, this evaporation reduces the signal measured when compared to a doped beam not subject to irradiation. When the light source is chopped and the detector signal is coupled into a lock-in amplifier, it is possible to measure a difference in signal with light passing through the droplets versus when the droplets are not irradiated. By tuning the chopped light source over a frequency range and logging the signal at the lock-in amplifier, a spectrum of the dopants is recorded.

For our experiment, an Extrel quadropole mass spectrometer (QMS) with an electron impact ionization source is used as a detector. This is a useful tool even in the absence of a light source, as it allows for the identification of which chemical species are doped into the droplets and the quality of the droplet beam. When a chopped light source is present, a dip in signal on the mass spectrometer occurs when the light induces some transition in the dopant and reduces the droplet's geometric cross-section. By selecting a particular mass to charge ratio, a specific dopant can be isolated [20, 21], a particularly useful feature when a dopant production process (such as pyrolysis) creates byproducts that are not of interest in the experiment, but which still may find their way into droplets. When a single mass-to-charge ratio is selected, the signal is passed from the Extrel QMS into a Stanford Systems pre-amplifier, which then passes signal into a set of Stanford Systems lock-in amplifiers, which are synchronized to a chopper that modulates the light source.

As a particular mass-to-charge ratio is monitored, the idler beam of an Argos Aculight tunable continuous wave optical parametric oscillator (OPO) is used as a light source. This beam is tunable over the range of $2750 - 3100\ cm^{-1}$, with over $1\ W$ of output available [22]. This beam is counterpropogated along the axis of the droplet beam, so that the laser and droplet beam have the greatest amount of overlap possible. Infrared spectra are gathered by taking a measurement of the lock-in amplifier signal as a function

of the frequency of the idler beam. The frequency of the idler output is monitored in real time by picking off a small portion of the beam and passing it into a Bristol wavemeter.

The Aculight OPO system is pumped with $5 - 15\ mW$ of $1064\ nm$ light from a Koheras AdjustiK continuous wave Yb-doped fiber laser. This fiber laser is tunable over a $6\ cm^{-1}$ range by changing the temperature and piezoelectric strain applied to the system. The output of this fiber laser is passed into and IPG photonics fiber amplifier, which amplifies the output of the Koheras laser to $15\ W$. This amplified light is directed into a bow-tie cavity in the OPO that has a magnesium oxide doped periodically poled lithium niobate (MgO:PPLN) crystal in the beam path. This crystal has a "fan-out" poling periodicity giving it a linear variance in poling period along its width. The crystal can be translated up and down in the cavity, changing the poling period the beam in the cavity encounters. Passing the pump beam through the cavity produces three beams of different frequencies: the residual pump beam, the cavity-resonant "signal" beam, and the "idler" beam which is used for spectroscopy. Changing the frequency of the signal beam changes the frequency of the idler beam, so tuning of the beam in the instrument is effected by tuning the frequency which is resonant in the OPO's cavity. The OPO system as a whole is tunable over the $2700 - 3125\ cm^{-1}$ range for the "C" module system used, though other Aculight OPO modules are capable of operating at up to $4300\ cm^{-1}$.

References

(1) Harms, J.; Toennies, J. P.; Knuth, E. L. Droplets formed in helium free-jet expansions from states near the critical point. *J. Chem. Phys.* **1997**, *106*, 3348–3357.

(2) Toennies, J. P.; Vilesov, A. F. Superfluid Helium Droplets: A Uniquely Cold Nanomatrix for Molecules and Molecular Complexes. *Angew. Chem. Int. Ed.* **2004**, *43*, 2622–2648.

(3) Lewerenz, M.; Schilling, B.; Toennies, J. A new scattering deflection method for determining and selecting the sizes of large liquid clusters of 4He. *Chem. Phys. Lett.* **1993**, *206*, 381–387.

(4) Buchenau, H.; Knuth, E. L.; Northby, J.; Toennies, J. P.; Winkler, C. Mass spectra and time-of-flight distributions of helium cluster beams. *J. Chem. Phys.* **1990**, *92*, 6875–6889.

(5) Toennies, J. P.; Vilesov, A. F. Spectroscopy of Atoms and Molecules in Liquid Helium. *Annu. Rev. Phys. Chem.* **1998**, *49*, 1–41.

(6) Raston, P. L. HeNDS: A program for calculating average Helium NanoDroplet Sizes. *SoftwareX* **2021**, *14*, 100703.

(7) Knuth, E. L.; Henne, U. Average size and size distribution of large droplets produced in a free-jet expansion of a liquid. *J. Chem. Phys.* **1999**, *110*, 2664–2668.

(8) Callegari, C.; Lehmann, K. K.; Schmied, R.; Scoles, G. Helium nanodroplet isolation rovibrational spectroscopy: Methods and recent results. *J. Chem. Phys.* **2001**, *115*, 10090–10110.

(9) Scheidemann, A.; Toennies, J. P.; Northby, J. A. Capture of neon atoms by ^{4}He clusters. *Phys. Rev. Lett.* **1990**, *64*, 1899–1902.

(10) Lewerenz, M.; Schilling, B.; Toennies, J. P. Successive capture and coagulation of atoms and molecules to small clusters in large liquid helium clusters. *J. Chem. Phys.* **1995**, *102*, 8191–8207.

(11) Brink, D.; Stringari, S. Density of States and Evaporation Rate of Helium Clusters. *Z. Phys. D* **1990**, *15*, 257–263.

(12) Hartmann, M.; Miller, R. E.; Toennies, J. P.; Vilesov, A. Rotationally Resolved Spectroscopy of SF_6 in Liquid Helium Clusters: A Molecular Probe of Cluster Temperature. *Phys. Rev. Lett.* **1995**, *75*, 1566–1569.

(13) Nauta, K.; Miller, R. E. Solvent mediated vibrational relaxation: Superfluid helium droplet spectroscopy of HCN dimer. *J. Chem. Phys.* **1999**, *111*, 3426–3433.

(14) Paesani, F.; Whaley, K. B.; Douberly, G. E.; Miller, R. E. Rovibrational Spectra for the HCCCN·HCN and HCN·HCCCN Binary Complexes in 4He Droplets. *J. Phys. Chem. A* **2007**, *111*, 7516–7528.

(15) Raston, P. L.; Liang, T.; Douberly, G. E. Infrared spectroscopy of HOOO and DOOO in 4He nanodroplets. *J. Chem. Phys.* **2012**, *137*, 184302.

(16) Franke, P. R.; Brice, J. T.; Moradi, C. P.; Schaefer, H. F.; Douberly, G. E. Ethyl + O2 in Helium Nanodroplets: Infrared Spectroscopy of the Ethylperoxy Radical. *J. Phys. Chem. A* **2019**, *123*, 3558–3568.

(17) Fröchtenicht, R.; Henne, U.; Toennies, J. P.; Ding, A.; Fieber-Erdmann, M.; Drewello, T. The photoionization of large pure and doped helium droplets. *J. Chem. Phys.* **1996**, *104*, 2548–2556.

(18) Buchenau, H.; Toennies, J. P.; Northby, J. A. Excitation and ionization of 4He clusters by electrons. *J. Chem. Phys.* **1991**, *95*, 8134–8148.

(19) Scheidemann, A.; Schilling, B.; Toennies, J. P. Anomalies in the reactions of helium(1+) with sulfur hexafluoride embedded in large helium-4 clusters. *J. Phys. Chem.* **1993**, *97*, 2128–2138.

(20) Fröchtenicht, R.; Toennies, J.; Vilesov, A. High-resolution infrared spectroscopy of SF6 embedded in He clusters. *Chem. Phys. Lett.* **1994**, *229*, 1–7.

(21) Hartmann, M.; Mielke, F.; Toennies, J. P.; Vilesov, A. F.; Benedek, G. Direct Spectroscopic Observation of Elementary Excitations in Superfluid He Droplets. *Phys. Rev. Lett.* **1996**, *76*, 4560–4563.

(22) Morrison, A. M.; Liang, T.; Douberly, G. E. Automation of an "Aculight" continuous-wave optical parametric oscillator. *Rev. Sci. Inst.* **2013**, *84*, 013102.

Chapter 3

Helium Droplet Infrared Spectroscopy of the Butyl Radicals

Kale E. King[1], Peter R. Franke[2,1], Gregory T. Pullen[1], Henry F. Schaefer III[1,3], and Gary E. Douberly[1]

1. Department of Chemistry, University of Georgia, Athens, GA, 30602

2. Department of Chemistry, University of Florida, Gainesville, FL, 32611

3. Center for Computational Quantum Chemistry, University of Georgia, Athens, GA 30602

Submitted to the Journal of Chemical Physics (in revision)

Abstract

Butyl radicals (*n-*, *s-*, *i-*, and *tert*-butyl) are formed from the pyrolysis of stable precursors (1-pentyl nitrite, 2-methyl-1-butyl nitrite, isopentyl nitrite, and azo-*tert*-butane, respectively). The radicals are doped into a beam of liquid helium droplets and probed with infrared action spectroscopy from $2700 - 3125$ cm^{-1}, allowing for a low temperature measurement of the CH stretching region. The presence of anharmonic resonance polyads in the $2800 - 3000$ cm^{-1} region complicates its interpretation. To facilitate spectral assignment, the anharmonic resonances are modeled with two model Hamiltonian approaches that explicitly couple CH stretch fundamentals to HCH bend overtones and combinations: a VPT2+K normal mode model based on CCSD(T) quartic force fields and a semi-empirical local mode model. Both of these computational methods provide generally good agreement with the experimental spectra.

3.1 Introduction

The butyl radical systems represent the smallest hydrocarbon radical systems that may contain branching in the carbon skeleton and include all three types of carbon-centered radical site: primary, secondary, and tertiary (see Fig. 3.1). These radicals are of interest in the low-temperature combustion scheme, with the barrierless association of butyl radicals and molecular oxygen forming $C_4H_9OO\cdot$, which can then decompose into bimolecular products or rearrange to form a carbon-centered (QOOH) radical [1, 2]. Hydroperoxyalkyl QOOH radicals are critical species within low-temperature hydrocarbon oxidation mechanisms, as their reactions with molecular oxygen represent branching points leading to exponential radical growth. While propyl peroxy radicals are the smallest radicals capable of forming QOOH species through intramolecular rearrangement, *n*-butyl radicals have been suggested as more archetypical of a generalized combustion scheme, as *n*-butyl is more apt to form six-membered rings during the hydrogen abstraction process [3]. There have been previous computational and experimental probes of butyl+O_2 and its dissociation or rearrangement into QOOH species [1, 4–6].

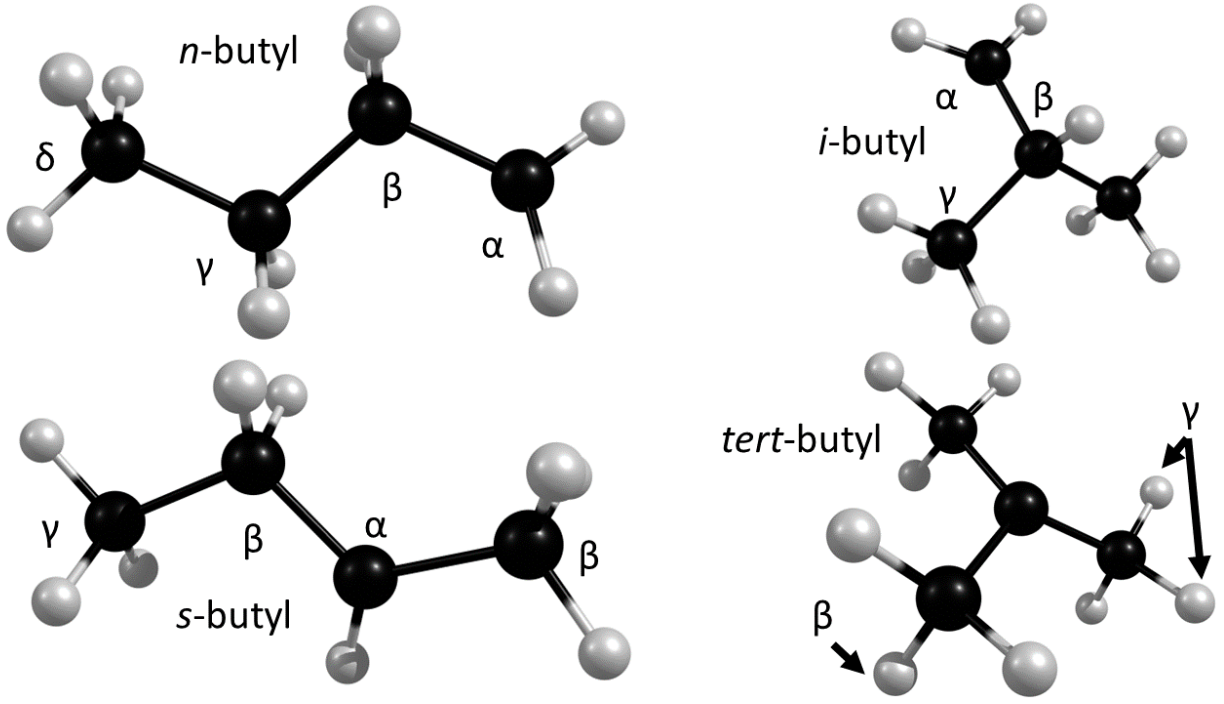

Figure 3.1: The four butyl radicals, with carbon centers and hydrogens labeled where applicable.

Pacansky's argon matrix isolation research on the *n*-, *i*-, and *tert*-butyl radicals is the most complete infrared spectroscopic work to date on the butyl radicals [7–9]. In two separate experiments, dipentanoyl peroxide and diacyl peroxide were deposited into an argon matrix and irradiated with UV light, photolyzing into *n*- and *i*-butyl radicals, respectively. In another experiment, *tert*-butyl radical was formed through flash vacuum pyrolysis of azoisobutane and deposited into an argon matrix. Pacansky reported characteristic α-CH_2 stretches at 3105.0 (antisymmetric) and 3017.5 cm^{-1} (symmetric) for *n*-butyl and 3115.0 (antisymmetric) and 3023.0 cm^{-1} (symmetric) for *i*-butyl, with characteristic β-CH stretches of 2800.0 and 2820.0 cm^{-1} for *n*- and *i*-butyl, respectively, where α is defined as the carbon center with the radical site, β is one carbon center away from the radical site, γ is two centers away, and so on [8]. The profound red-shifts of β-CH stretches are a consequence of the parallel alignment of the β-CH bonds with the unpaired electron on the alpha carbon. Because of this, we prefer a different naming scheme for

the CH stretches of *tert*-butyl radical, in which one CH bond per methyl group is oriented parallel (or axial) to the unpaired electron and the other two CH bonds are in equatorial positions, rotated about 45 degrees from the unpaired electron. The influence of the radical site breaks the symmetry of the methyl stretches; the stretching vibrations of the axial CH appear at low frequency, so we will refer to them as β-CH stretches. Pacansky identified one β-CH stretching band at 2825.0 cm^{-1} [8]. The equatorial CH_2 stretches will be referred to as γ, despite stretching at somewhat lower frequency than the γ-CH stretches in the naming scheme for the other butyl radicals.

Photoelectron spectroscopy has also been applied to all four butyl radicals [10–12]. In a pair of experiments, butyl radicals were generated by vacuum pyrolysis of nitrite precursors and photoionized with a capillary discharge lamp. Ionization potentials and heats of formation were determined, with the primary *n*- and *i*-butyl radicals having greater ionization potentials and heats of formations than the secondary or tertiary butyl radicals [10, 11]. Later photoelectron spectroscopy has determined ionization potentials and heats of formation for the *s*- and *tert*-butyl radicals greater than those from the earlier report [13, 14]. Photoionization mass-spectrometry of butyl radicals generated through photodissociation of butyl halides has corroborated the thermochemical trends found in the photoelectron spectra, though with some minor differences in the determined heats of formation [15]. The general trends were attributed to hyperconjugation, with more hydrogen atoms present at the radical site leading to stronger hyperconjugation effects.

There are sparse computational studies on the infrared spectra of the butyl radicals. Pacansky carried out UHF/6-31G* studies on the vibrational spectrum of the *n*-butyl radical [16] and semi-empirical INDO studies on *tert*-butyl radical's vibrational spectrum [17]. These computations generally reflect the argon matrix isolation infrared spectra well, though only the *trans* rotamer of the *n*-butyl radical was accounted for, ignoring possible contributions from the *gauche* rotamer. Spectra for the *s*-butyl radical have also been computed at the UHF/6-31G* level [18].

An interesting albeit esoteric aspect of alkyl radicals is the complicated shape of their electronic potential energy surfaces in the torsional and large-amplitude bending degrees of freedom. Primary alkyl

radicals (e.g., ethyl, *n*-propyl, and longer analogues) are known to have low barriers to α-CH_2 rotation. Ethyl radical possesses a small six-fold torsional barrier of around 30 cm^{-1}. The longer members have two-fold torsional barriers a few times higher, and these potentials often appear convoluted with shallow minima and maxima in the vicinity of the expected maxima and minima, respectively [19, 20]. For the longer members of the primary alkyl radicals, this finer structure appears to have little influence upon the torsional energy level structure. It may be shown that the ground torsional wavefunction is delocalized over the top of the shallow maxima or alternatively that zero-point correction of the potential curve "washes out" the shallow stationary points, leading to a more conventional looking potential surface [21–23]. Thus, the *n*-propyl radical and the *trans* rotamers of longer primary alkyl radicals are expected to possess effective C_s symmetry, although they may have only C_1 symmetry electronic minima. This is the expected symmetry of the *trans-n*-butyl radical.

Large-amplitude bending of the α-CH (and coupled skeletal bending motion) of secondary alkyl radicals has received somewhat less theoretical attention. In previous research, we showed that harmonic zero-point correction of an intrinsic reaction path between the C_s electronic minima of *i*-propyl radical and a low-lying C_{2v} transition state was sufficient to eliminate the barrier, reducing the double-well potential to a single well [23]. In a follow-up study on cyclobutyl radical, we took the alternative approach, showing that the ground state wavefunction in a vibrationally-adiabatic large-amplitude bending potential is delocalized over the low-lying C_{2v} transition state [24]. Chen and Wang conducted a theoretical study of *s*-butyl's central C-C torsional degree of freedom, which connects the *trans* and *gauche* rotamers [25]. They identified a third electronic minimum, which they called *cis*, separated from *gauche* by a shallow barrier. Upon zero-point correction of the stationary points, this barrier vanished; however, much ambiguity remains about the structure of the C_1 symmetry rotamers. Zero-point correction of the entire potential curves was not performed; moreover, a cusp is present on most of their potentials in the vicinity of the *cis* and *gauche* minima, casting doubt on the suitability of their coordinate system. The zero-point correction also removes the barrier separating the pair of C_1 symmetry *trans-sec*-butyl electronic minima, suggesting effective C_s symmetry.

The structure of the *tert*-butyl radical has been investigated computationally by Pacansky and coworkers [26]. Pacansky and Yoshimine computed, with the HF-SCF method, hindering barriers to methyl rotation ranging from 1.5-1.9 kcal/mol, depending on whether an individual methyl group rotates or whether multiple methyl groups rotate in a concerted manner [27]. Carmichael, using UHF/3-21G, predicted that the barrier to inversion was 1.7 kcal/mol and that the minimum energy inversion pathway was strongly coupled to the internal rotations of the methyl groups. He illustrated this with a two-dimensional potential surface of the skeletal inversion and symmetrical methyl torsional motion [28]. Schaefer and coworkers conducted an investigation of the barriers with convergent *ab initio* methods [29]. They found barriers of 0.7 kcal/mol for inversion and 0.9 kcal/mol for rotation of a single methyl group. The computational chemistry consensus is that *tert*-butyl radical has a nonplanar carbon skeleton and C_{3v} symmetry. This is consistent with the results of electron-spin resonance experiments [30, 31].

Choosing a meaningful reference structure is one aspect in the design of semi-empirical local mode simulations. Local mode computations have proved a useful tool for modeling the CH stretches of hydrocarbons and hydrocarbon radicals [32–34]. The simplified local mode model of Sibert and coworkers [33] starts with the computation of a Cartesian Hessian matrix, typically with a DFT method, at a stationary point. Local mode coordinates are obtained by iteratively increasing the masses of all atoms not involved in the desired local coordinate, in order to decouple the motions, and then diagonalizing the Hessian. Anharmonic contributions to this model are handled through the introduction of fixed parameters that couple CH stretches with the overtones and combinations of HCH scissor modes. This method has been applied to a variety of systems, with the modeling of alkyl benzenes [33] and alkyl benzyl radicals [34] of particular relevance, as both systems are well-modeled with the same coupling parameters. The extensibility of these parameters to new systems is of great interest: if these parameters are well-suited to a broad range of alkyl radical systems, they would represent an attractive, low-cost method for computing vibrational spectra of hydrocarbon radicals. We have used the local mode model in the past to model the stretch-bend coupling of the propyl radicals, yielding results in good agreement with experimental spectra [23].

In this work, we report infrared spectra in the CH stretching region for all four butyl radicals, which includes the first experimental spectra in this region for the *s*-butyl radical. These radicals were produced by vacuum pyrolysis, doped into helium nanodroplets [35–40], and analyzed with a mass spectrometer and tunable infrared laser. The spectra obtained are relatively well-resolved, revealing a wealth of anharmonic coupling interactions between the CH stretches and overtones and combinations of HCH bending modes. We have predicted the spectra of these radicals with both local mode and VPT2+K effective Hamiltonian methods. These predicted spectra, when combined with the minimally-perturbed helium droplet spectra, have allowed us to characterize the origins of the anharmonic couplings and assign spectral regions to specific carbon centers.

3.2 Experimental Methods

The methodology of HElium NanoDroplet Isolation (HENDI) has been reviewed [41–44]. Droplets of liquid He are formed by the expansion of $35\ bar$ of gaseous He into vacuum through a $5\ \mu m$ orifice cooled to $17\ K$, resulting in droplets having an average size of 4500 He atoms. After expansion, the beam of droplets is passed through a $0.4\ mm$ conical skimmer into a differentially-pumped vacuum chamber. In the second chamber, the beam passes through a $1\ cm$ region containing butyl radicals at a density of roughly $10^{10}\ cm^{-3}$. These radicals are generated by pyrolysis of precursor molecules in a high-temperature, effusive pyrolysis source which consists of a quartz tube wrapped with a tantalum filament. As precursor molecules collide with the heated quartz, they decompose, and the decomposition products (pyrosylate) effuse into the path of the droplet beam. The pyrosylate molecules that collide with droplets embed in the droplets, which cool the hot pyrosylate to $0.4\ K$ through rapid evaporation of He atoms.

Precursor nitrite molecules are synthesized from a variety of $C_5H_{11}OH$ alcohols by forming a solution of the alcohol and sulfuric acid. Sodium nitrite is added to this solution, converting the alcohol moiety into nitrite. When pyrolyzed, these $C_5H_{11}ONO$ nitrites decompose into nitric oxide, formaldehyde, and a butyl radical. Specifically, isopentyl nitrite is pyrolyzed into the *i*-butyl radical, pentyl nitrite into *n*-butyl radical, and 2-methyl-1-butyl nitrite into *s*-butyl radical. Azo-*tert*-butane is used as a precursor for

the *tert*-butyl radical. Upon pyrolysis it decomposes into molecular nitrogen and two *tert*-butyl radicals, offering higher doping efficiency than a nitrite.

The droplets are analyzed in an electron ionization quadrupole mass spectrometer oriented perpendicular to the droplet beam. A detailed description of the method of dopant ionization is available elsewhere [42, 45]. Briefly, the droplet is ionized and the charge migrates to the center of the droplet, transferring charge to the dopant, which desolvates and fragments the dopant. The geometric cross-section of the droplets affects the chances of droplet ionization.

The mid-infrared output from the idler of a continuous-wave optical parametric oscillator (cw-OPO) is directed along the same axis as the droplet beam in a counter-propagating orientation. The tuning and operation of the cw-OPO have been discussed in detail previously [46]. When the cw-OPO is tuned into resonance with a vibrational transition of the dopant, the dopant is excited, and this excitation is then transferred into the droplet, which cools through He evaporation. This energy transfer and evaporation is rapid in comparison to movement of the droplets along the beam axis, so excitation of the dopants is observed as a reduction in the ionization cross-section of the He droplets and a reduction in ion signals associated with mass channels corresponding to the excited dopant. This dip in ionization signal constitutes the "action" component of HENDI. By chopping the laser beam at $80\ Hz$ and coupling the mass spectrometer signal into a lock-in amplifier, background-free depletion signals are recorded with a resolution of approximately $20\ MHz$. Selection of a proper mass channel in the mass spectrometer allows for quasi-species-selective IR spectra to be gathered. In the case of all four radicals, $m/z = 41$ $(C_3H_5)^+$ was chosen, as this mass channel maximized signal of CH stretches that were directly attributable to the radicals.

3.3 Theoretical Methods

3.3.1 Potential Energy Surfaces

Analogous to the propyl radicals, the butyl radicals exhibit multiple shallow minima and maxima (on the order of tens of wavenumbers) on their α-CH_2 torsion and α-CH wagging electronic potential energy surfaces [22]. Consequently, the electronic minimum energy structures of *trans-n*-butyl and *trans-sec*-butyl are C_1 rather than C_s symmetry. Although, the effective structures of these systems are presumably of C_s symmetry when vibrational effects are considered.

To better understand the symmetry of these radicals, we computed relaxed potential energy surfaces for the α-CH_2 torsion of *n*-butyl and *i*-butyl and the out-of-plane α-CH wag of *s*-butyl. Computations were performed using the CFOUR package [47, 48]. The butyl radicals were described with the CCSD(T) method based on Unrestricted Hartree-Fock (UHF) references [49–53]. Exploratory computations did not reveal a strong reference dependence for these radicals. The frozen-core approximation was made. Constrained optimizations for relaxed potential energy surfaces used the double-zeta ANO0 basis set, and single-point energies were evaluated at optimized geometries with the triple-zeta ANO1 basis set [54].

From the optimized structures, we also determined the kinetic energy functions and used them in variational computations of the vibrational bound-states [55]. For *trans-* and *gauche- s*-butyl, large geometry relaxation was observed in the skeletal torsion (i.e., the isomerization coordinate). This sudden relaxation manifests in the kinetic energy function as a near-singularity, which precludes an accurate determination of the bound-states. To remedy this, we described both *s*-butyl radicals with a single 2D torsion-wagging potential. Unfortunately, substantial geometry relaxation was also observed for this relaxed potential, now in the torsion of the methyl group adjacent to the radical CH. Multidimensional bound state computations were not attempted; in the case of *s*-butyl, we simply report the potential surface.

One-dimensional torsional potential and kinetic energy functions were fit to cosines or both cosines and sines, as appropriate given the symmetry, and the matrix representation of the Hamiltonian was set up in the free-rotor basis [56, 57]. Hamiltonian matrix elements were evaluated analytically. At most,

even/odd symmetry was exploited to block-diagonalize the Hamiltonian. The pseudopotential contribution was neglected [56].

3.3.2 Normal Mode Simulations

A similar vibrationally anharmonic analysis was performed here as was applied previously to the propyl radicals [23]. Two kinds of anharmonic simulation were applied. The first kind entailed a traditional Vibrational Perturbation Theory (VPT) simulation based on the normal-coordinate Watson Hamiltonian and *ab initio* quartic force fields [58]. All normal-coordinate force field computations were carried out with CFOUR [47, 48]. Quadratic force constants and first derivatives of the dipole moment were computed at CCSD(T)/ANO1 by numerical differentiation of analytic gradients. Cubic and quartic force constants were computed by numerical differentiation of CCSD(T)/ANO0 analytic second derivatives [59]. These force constants were combined into a hybrid force field [60, 61]. Specifically, the harmonic frequencies of the CCSD(T)/ANO0 force field were substituted with the corresponding CCSD(T)/ANO1 values [62]. This approximation is most appropriate when the normal coordinates associated with the different levels of theory are similar. This is generally the case for the butyl radicals, with the largest differences seen for *gauche-n*-butyl and *gauche-sec*-butyl.

Predictions of the CH stretching spectra were made using Second-Order Vibrational Perturbation Theory with Resonances (VPT2+K). Detailed descriptions of this method have been given previously [24, 62–64]. VPT2+K is applied in a similar form to what was described in the "Large Effective Hamiltonian Simulations" section of Reference [62], including all of the singly-excited CH stretches and doubly-excited HCH scissors. The simulations were designed such that VPT2+K included at least the same degree of explicit stretch/bend coupling as the local mode simulations. For *n*-butyl and *i*-butyl, additional triply- and quadruply-excited states were included to treat connected-resonances of the bends [62]. These do not manifest in the local-mode model, but treating them in VPT2+K can be important for a more accurate description of the essential coupling between singly- and doubly-excited states. Connected resonances were identified using the Martin Test [65], using a threshold value of 1 cm^{-1} and an additional zeroth-order

energy difference threshold of 250 cm^{-1}. States excited in torsional or large-amplitude bending coordinates were not considered to be in resonance. Diagonalization of the effective Hamiltonian yields the anharmonic transition frequencies. VPT2+K was implemented in Mathematica [66].

Intensity was derived from the linear harmonic oscillator transition moments, avoiding use of the VPT2 transition moments, which are highly sensitive to anharmonic resonances. The matrix representation of the harmonic oscillator transition moments, in the original basis, was transformed with the eigenvectors of the VPT2+K effective Hamiltonian, accounting for most of the strong mechanical anharmonicity but none of the electrical anharmonicity [67]. As an aside, in a symmetric top such as *tert*-butyl, the vibrational degeneracy patterns are not precisely reproduced by the conventional formulation of VPT2, appropriate for asymmetric tops [68, 69]. However, inclusion of the Darling-Dennison coupling is sufficient to correct this [70]. Small (on the order of 0.1 cm^{-1}) splittings of formally degenerate transitions still exist, caused by numerical errors in the force constants.

3.3.3 Local Mode Simulations

To complement the VPT2+K normal coordinate simulations, anharmonic predictions were also made with the semi-empirical local mode model of Sibert and coworkers [23, 33, 34]. This allowed us to investigate whether the local mode model is extensible from propyl to butyl radicals. In particular, the *tert*-butyl radical possesses no α hydrogens, making it distinct from other organic radicals to which the local mode model has been previously applied.

The local mode simulations began with a B3LYP/6-311++G** harmonic frequency computation from Gaussian 09 [71]. The Cartesian Hessian was extracted. It was mass-weighted and diagonalized to obtain the normal coordinates and harmonic frequencies. The mass-weighted normal coordinates were scaled to become dimensionless. We use a different procedure to localize the coordinates than the one used by Sibert and coworkers. Elements of the 1st-order L-tensor (derivatives of the internal coordinates with respect to the dimensionless normal coordinates) were evaluated by finite differences [72]. Blocks of the L-tensor associated with CH stretching and HCH bending were separately orthogonalized to obtain unitary

transformation matrices. The CH stretching and HCH bending harmonic frequencies were separately transformed, yielding blocks of localized force constants. The stretching block served as the singly-excited stretching block of the effective Hamiltonian. The matrix elements of the doubly-excited bending block were computed from a generalized form of the harmonic oscillator Hamiltonian, which involves non-diagonal, localized harmonic frequencies, ω_{ij}, and position and momentum operators having the usual matrix elements [73].

$$\hat{H}_{local} = \frac{\hbar^2}{2} \sum_{ij} \omega_{ij} (q_i q_j + \hat{p}_i \hat{p}_j) \tag{3.1}$$

The bending block comprised all possible doubly-excited bending states in the HCH scissor coordinates, to which each CH_3 group contributed three coordinates and each CH_2 group contributed one. According to the numerical recipe for the simplified local mode model [33], the following changes were made to the Hamiltonian. The diagonal bending frequencies were scaled by 0.975, and 9.6 cm^{-1} was further subtracted from those corresponding to overtones (i.e., doubly-excited in the same coordinate). Diagonal stretching frequencies were scaled by 0.96 if localized on a CH_2 group; otherwise, they were scaled by 0.961. Finally, a coupling of -4.5 cm^{-1} was inserted between bending overtones localized on the same methyl group. Fermi coupling parameters were included only between stretches and bends localized on the same carbon site. These take on four different values depending on the orientation, depicted in Figure 3 of Reference [33]. A matrix element of 22 cm^{-1} couples a CH stretch to the adjacent HCH bend overtone. A smaller coupling element of 2.5 cm^{-1} was included between a CH stretch on a methyl group and the bend overtone associated with the other two, uninvolved hydrogen atoms. Also specific to methyl groups are Fermi couplings between a CH stretch and an HCH bend combination. These matrix elements were set to 1.5 cm^{-1} when the stretching hydrogen was involved in both bend coordinates and 5.6 cm^{-1} when it was only involved in one [33].

Anharmonic frequencies were determined by diagonalizing the effective Hamiltonian. To obtain intensities, the linear harmonic oscillator transition moments of the stretching fundamentals were first transformed into localized coordinates in the same manner as the stretching frequencies. Then they were further transformed with the effective Hamiltonian eigenvectors. (In this model, all doubly-excited bends

have vanishing zeroth-order transition moments.) This has the effect of distributing intensity into the various strongly-mixed stretching/bending transitions. The local mode Hamiltonian model was implemented in Mathematica [66].

For local-mode simulations, we elected to use the higher symmetry stationary points (i.e., the shallow transition states) for *trans-sec*-butyl and *trans-n*-butyl. It was expected that these structures would be more representative of the average structures of the radicals. This was motivated by the variational computations for *trans-n*-butyl, indicating the delocalization of the ground state wavefunction over the high symmetry transition state. For VPT2+K, we used the lower symmetry electronic minima so that it was not necessary to use reduced dimensionality, which completely neglects the coordinate with the imaginary frequency. Neglect of torsional degrees of freedom in rectilinear VPT can introduce large errors in the CH stretching frequencies, so we prefer not to do this [23]. For *tert*-butyl, we made additional local-mode predictions at the C_{3h} symmetry inversion transition state.

So-called "dipole decompositions" are given for both normal mode and local mode anharmonic simulations [23, 33]. This allows for the simple, visual depiction of transition intensity arising from different molecular sites, avoiding tedious written descriptions of anharmonic mixing. In the *i*-butyl simulation, for instance, the transition moments of the β-CH and γ-CH_3 stretches could be zeroed out, leaving the α-CH_2 stretches as the sole source of spectral intensity.

In some cases, the separation scheme for the dipole decompositions of the same radical differed between normal coordinates and local coordinates. In *tert*-butyl radical, the normal coordinates divide themselves into A+E pairs of symmetric and antisymmetric CH_3 stretches, depending on their phase relationship. However, with local modes, the spectrum is decomposed into transitions arising from axial hydrogens, whose bonds are aligned with the unpaired electron, stretching at lower frequency, and transitions arising from the remaining, equatorial hydrogens, which stretch in the middle-CH stretching region, around 2950 cm^{-1}. The normal coordinates do reflect this to some extent, as the lower frequency symmetric stretches involve more axial CH stretch amplitude than equatorial; the inverse is true of the antisymmetric stretches.

3.4 Results

3.4.1 Potential Energy Surfaces

The α-CH_2 torsional potentials of *i*-, *trans-n*-, and *gauche-n*-butyl are shown in Fig. 3.2. The squared ground state wavefunction is plotted in each potential. Note the delocalization of the ground state above the shallow electronic potential barrier in *trans-n*-butyl radical, consistent with *n*-propyl radical. However, the influence of the barrier can be seen in the shape of the probability distribution; there is a small dimple at 90 degrees rather than a maximum. In this model, if the barrier were to be increased slightly, the probability would become divided evenly into both wells. The shallow well at 180 degrees cannot support a bound-state; it would likely become an energy maximum if zero-point corrections were applied to the potential curve. The torsional potentials of *gauche-n*-butyl and *i*-butyl are different in appearance, having shelves rather than small minima and maxima.

The 2D potential surface, describing the torsional interconversion of the *s*-butyl radicals and the out-of-plane wag of their α-CH, is shown in Fig. 3.3. The global minima on this surface are the two C_1 symmetry *trans-sec*-butyl stationary points, which are separated by a small, 42 cm^{-1} barrier. The *gauche* wells represent local minima, 77 cm^{-1} higher in energy than the *trans* wells; they are separated from the *trans* domain by a 166 cm^{-1} forward barrier and a 243 cm^{-1} reverse barrier. The most energetically unfavorable orientation is the 0 degree *cis* structure, situated at 443 cm^{-1} above the *gauche* wells. This potential lacks the cusp found previously in the one-dimensional torsional potential [25]. The cusp may have been caused by an unintended inversion at the α-CH group during subsequent constrained optimizations.

3.4.2 Experimental Results

We describe in this section the qualitative features of the experimental butyl radical spectra, focusing on the assignments of features that can be attributed to vibrations arising predominately from CH stretching on α, β, γ or δ carbon centers. With the pyrolysis source active, the experimental spectra exhibit distinctive

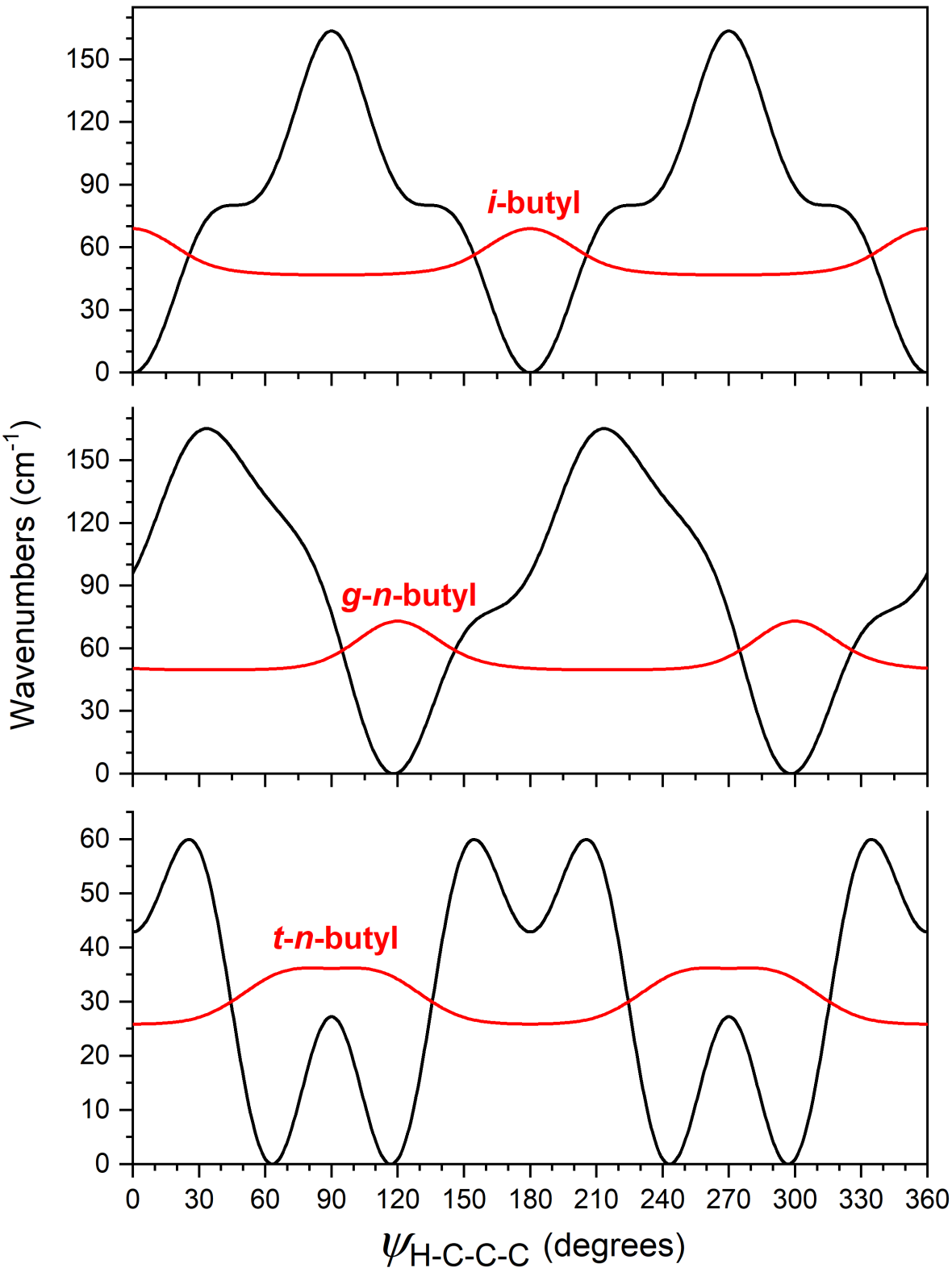

Figure 3.2: Relaxed potential curves for the α-CH_2 torsion of *n*- and the *i*-butyl radicals.

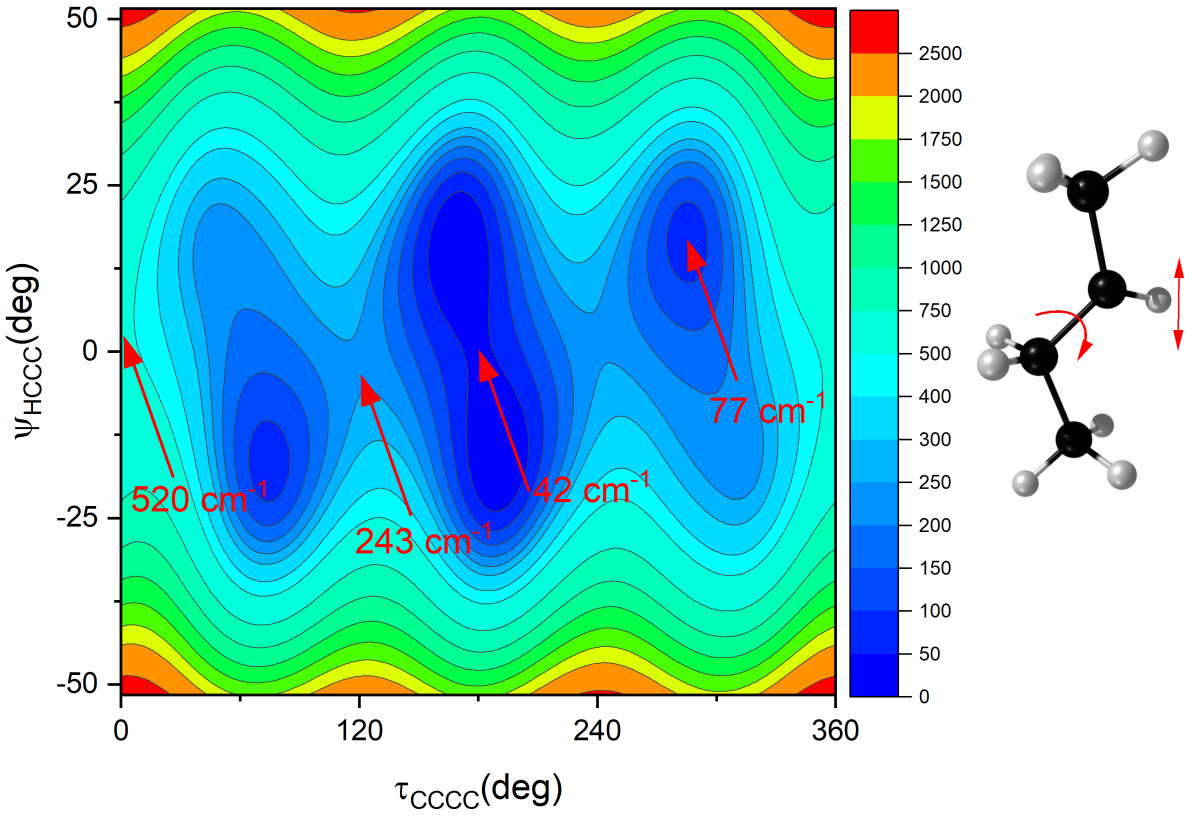

Figure 3.3: The skeletal torsion + out-of-plane α-CH wagging potential of the *s*-butyl radical. CCSD(T)/ANO1 electronic energies are given for stationary points, evaluated at CCSD(T)/ANO0 optimized structures.

changes in CH stretch absorption bands compared to those spectra recorded without the pyrolysis source active. All precursor nitrite spectra are characterized by broad absorption features in the 2900 to 2975 cm^{-1} region, typical of sp^3 hybridized alkane-type CH stretches. The appearance of α-CH stretches to the blue of 3000 cm^{-1} in those radicals with α-CH centers is the predominant change in going to the radical species, along with the appearance of β-CH stretches below 2850 cm^{-1}, which are also common to all butyl radical spectra. The spectra of all four butyl radicals show considerable resonance contributions in the region around and below 2950 cm^{-1}. This complicates the spectra to the extent that a prediction based on the harmonic oscillator model is insufficient to describe the CH stretch region of these radicals, even in a qualitative manner. Figure 3.4 shows a comparison between our experimental *i*-butyl spectra and the harmonic and anharmonic predictions. These comparisons reveal the common result that extensive anharmonic coupling between stretching fundamentals and bending combinations and overtones leads to additional spectral features between approximately 2700 and 2950 cm^{-1}. Throughout this section, the analysis of band positions relies on comparisons between experimental spectra and computations using the VPT2+K anharmonic model.

Figure 3.5 shows the experimental and computed spectra of the *n*-butyl radical. The HENDI spectra represent an improvement upon previous experimental spectra obtained in solid argon. Notably, both rotamers (*gauche* and *trans*) are observed in these new spectra, as is evidenced by the splitting present in the α-CH stretch bands centered at 3025 and 3110 cm^{-1}. This differs from the previous matrix isolation spectra reported by Pacansky, who reports single α-CH symmetric and asymmetric stretches at 3024 and 3105 cm^{-1}, respectively [7]. Pacansky also reported a β-CH stretch at 2886 cm^{-1}; this stretch is present in the new spectra as well, but it is unclear whether it is attributable to β-CH_2 stretching or γ, δ-$CH_{2,3}$ stretching. The broad features centered at 2973 cm^{-1} and the broad feature at 2949 cm^{-1} appear attributable to stretches centered at the γ and δ-CH centers, respectively. There is some contamination of the spectra contributed by 1-butene and formaldehyde at 3100 and 2784 cm^{-1}, respectively, though these contaminant peaks are minor and easily distinguishable from the radical spectra.

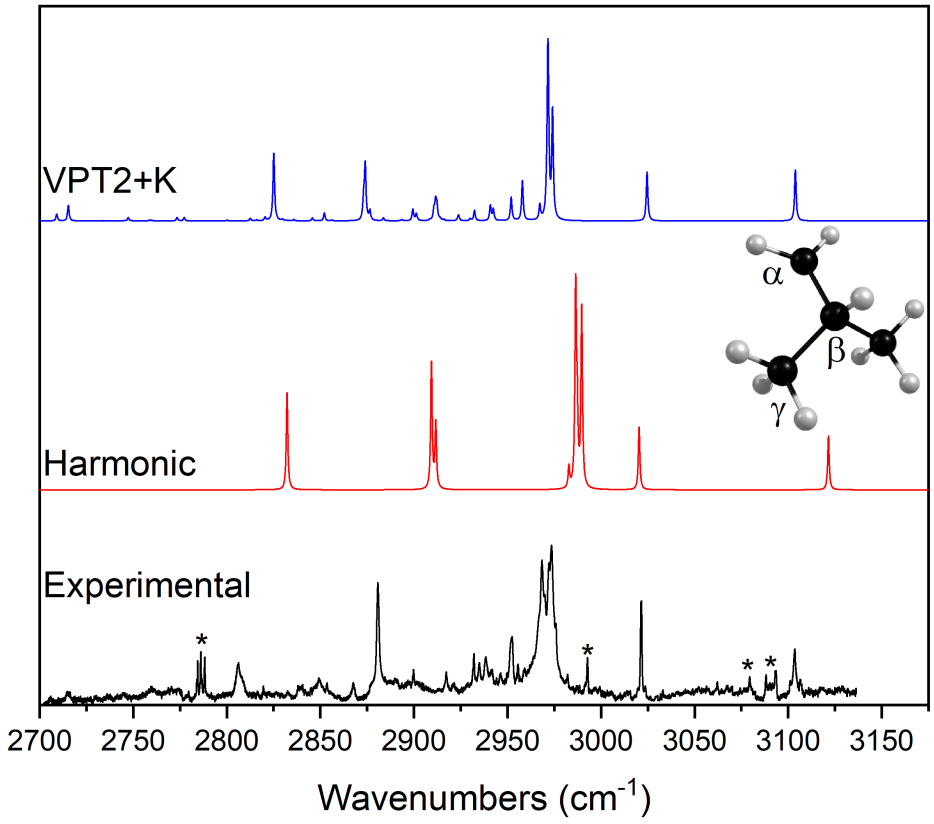

Figure 3.4: The VPT2+K spectrum of the *i*-butyl radical in comparison to the scaled harmonic and experimental spectra. The harmonic spectrum was scaled by 0.961, to reproduce the α-CH_2 symmetric stretch at 3020 cm^{-1}. The asterisks mark contamination from isobutene and formaldehyde.

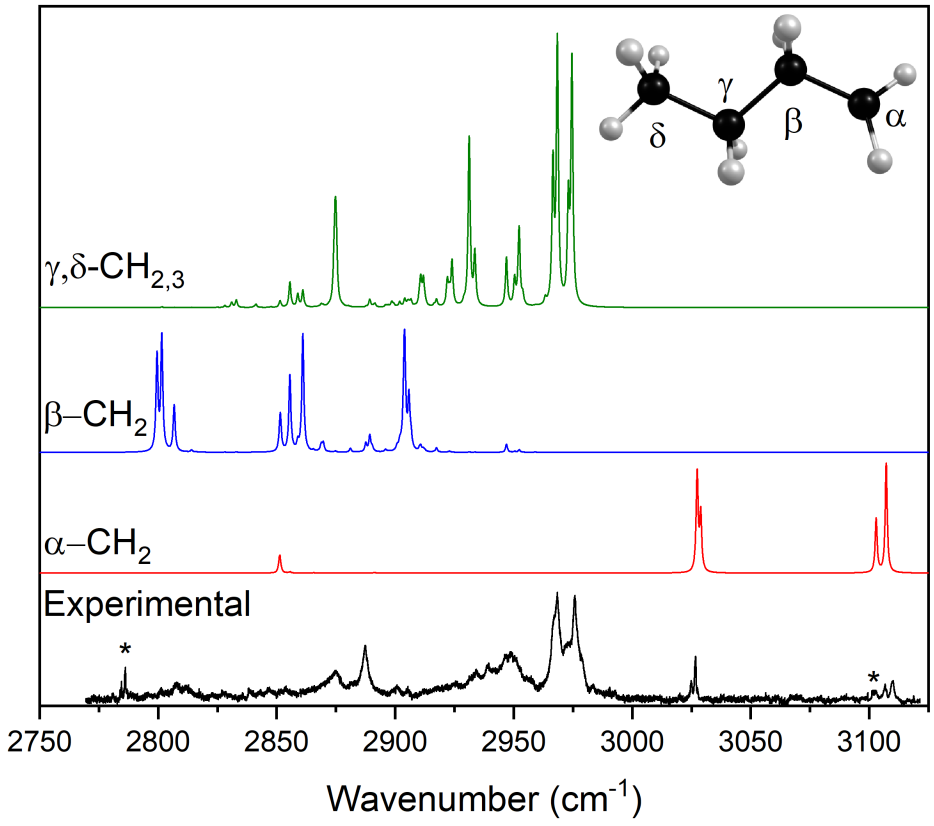

Figure 3.5: The VPT2+K dipole decomposition compared to the experimental spectrum of the *n*-butyl radical. The asterisks mark contamination from 1-butene and formaldehyde.

For the *i*-butyl radical spectra shown in Figure 3.6, the clearest spectral features again arise from the α-CH stretches at 3105 and 3022 cm^{-1}. The antisymmetric α-CH_2 band is somewhat red-shifted from previous matrix-isolation studies that had identified it at 3115 cm^{-1} [8]. The γ-CH stretching region is bookended by prominent peaks at 2970 cm^{-1} and 2980 cm^{-1}, with broader, less distinct features in between. A broadened peak at 2807 cm^{-1} is also attributable to the β-CH stretch. Some contamination peaks from isobutene and formaldehyde are present, with the former appearing at 2980 cm^{-1} and the latter in the $3075 - 3100$ cm^{-1} range.

The *s*-butyl spectra shown in Figure 3.7 represent the first vibrational spectra of this species. The lower-frequency contributions of the β- and γ-CH stretches are quite complex; the distinctive α-CH stretch is sharp and well-resolved. The presence of two conformers evidently increases the spectral complexity greatly, particularly with regard to the features around 2975 cm^{-1}. This complexity is less present in the α-CH stretching region, with no detectable splitting on the 3043 cm^{-1} feature. Either the stretches of both conformers overlap almost completely or the stretching band of the less-dominant conformer appears near the baseline level at ca. 3030 cm^{-1} or 3060 cm^{-1}. The broad triplet appearing at 2975 cm^{-1} contains contributions from both CH_3 centers, while the triplet at 2950 cm^{-1} is predicted to be a blend of the γ-CH_3 and both β-CH_X centers. Peaks to the red of 2950 cm^{-1} are not as easily assignable due to broadening and the overlapping stretches from three alkyl centers. The spectra are slightly contaminated with 1-butene and formaldehyde, at 2989 cm^{-1} and 2784 cm^{-1}, respectively.

Figure 3.8 shows the comparison between experimental and computed spectra of the *tert*-butyl radical. The experimental spectrum is somewhat less congested than those of the less symmetric butyl isomers. Distinct antisymmetric stretches are evident at 2952 and 2926 cm^{-1}, with the latter appearing as a doublet. These peaks bracket those found by Pacansky and Chang, who assign a peak at 2931 cm^{-1} to the antisymmetric CH stretch [9]. Symmetric stretches are also easily assignable, with a prominent doublet centered at 2810 cm^{-1}. These features are somewhat to the red of the symmetric stretch previously seen at 2825 cm^{-1} [9]. The spectra are notably contaminated with isobutene, though the spectral features arising from this

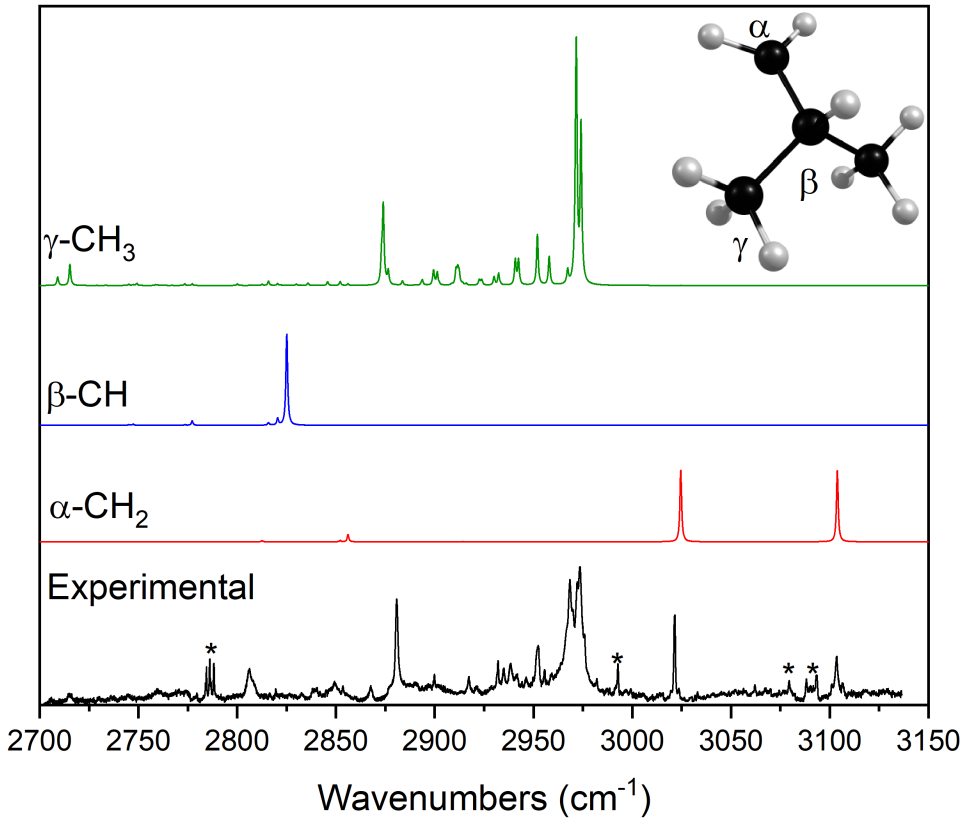

Figure 3.6: The VPT2+K dipole decomposition compared to the experimental spectrum of the *i*-butyl radical. Note the high-frequency contributions of the α-CH stretches. The asterisks mark contamination from isobutene and formaldehyde.

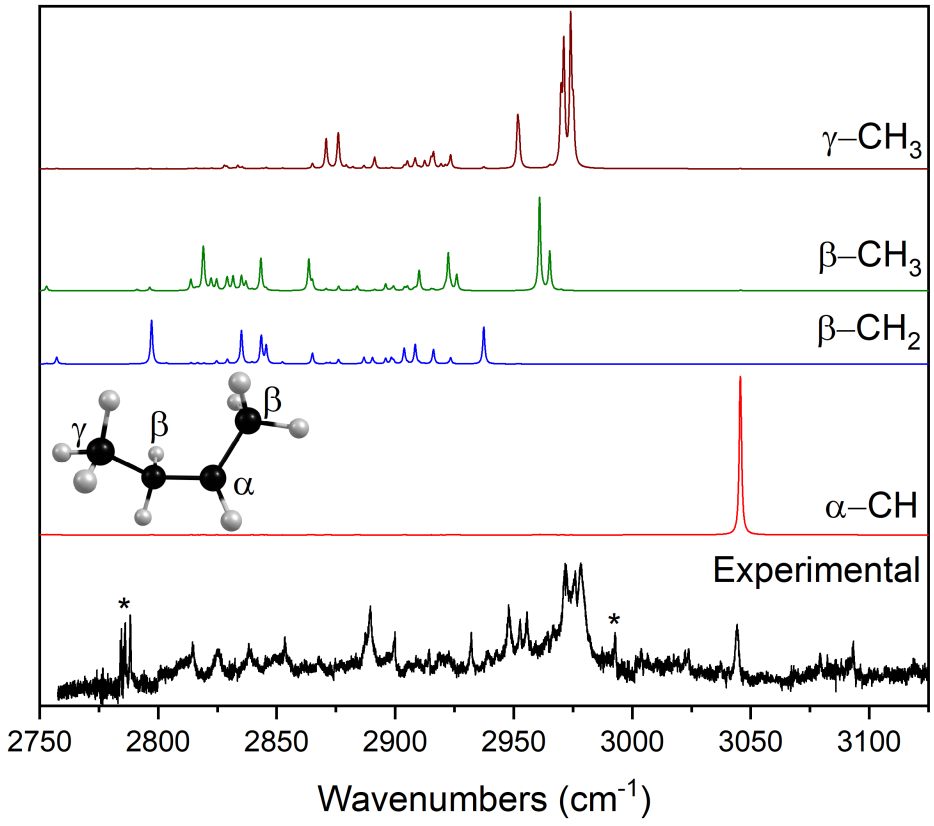

Figure 3.7: The VPT2+K dipole decomposition compared to the experimental spectrum of the *s*-butyl radical. The asterisks mark contamination from 1-butene and formaldehyde.

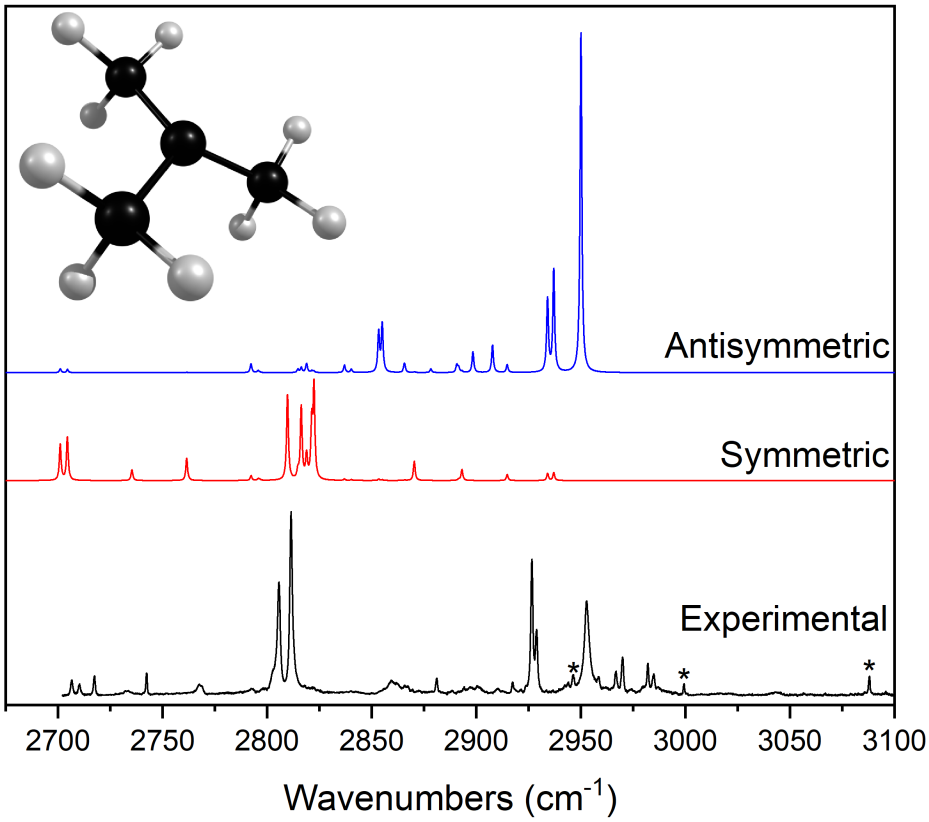

Figure 3.8: The VPT2+K dipole decomposition compared to the experimental spectrum of the *tert*-butyl radical. The asterisks mark contamination from isobutene.

contamination are generally of higher frequency than would be expected from the β or γ-CH stretches of the *tert*-butyl radical.

3.5 Discussion

3.5.1 Symmetry and Effective Structures

Trans-sec-butyl likely possesses effective C_s symmetry. Consider that the C_s transition state structure separates the equivalent C_1 minima by only about 50 cm^{-1} (Fig. 3.3). Previous experiments have assigned the α-CH wag fundamental of *i*-propyl radical at about 360 cm^{-1}. Assuming that the α-CH wag of *s*-butyl has a similar frequency, and assuming that the zero-point energies of these motions are roughly half the fundamentals, this implies 180 cm^{-1} of ZPVE. Therefore, it is reasonable to expect the ground state wavefunction to be delocalized above the shallow transition state. At the CCSD(T)/ANO1 level of theory, the high-symmetry structure is 49 cm^{-1} higher in energy than the electronic minimum. After including the harmonic zero-point energy of the orthogonal degrees of freedom, the energy ordering reverses. The high-symmetry structure is then 78 cm^{-1} lower in energy than the low-symmetry structure.

Previous theoretical work found a third distinct potential energy minimum, ("*cis*") for the *s*-butyl radical, albeit only at certain levels of theory [25]. It appeared at C-C-C-C dihedral angle values of around 50 degrees and was separated from *gauche-sec*-butyl by a small barrier. Upon zero-point correction, the small barrier vanished, and the third minimum merged with *gauche*. In our computations, we were unable to locate a third minimum. It probably does not exist at the levels of theory we employed. Our 2D potential energy surface is rather flat in the vicinity of the *gauche* structure. It seems most reasonable to conclude that there are only two rotamers of *s*-butyl, *trans* and *gauche*. The average ground-state C-C-C-C dihedral angle of the *gauche* rotamer would be difficult to determine computationally. It probably would require at least a 3-dimensional description, involving the skeletal torsion, α-CH wag, and one, or perhaps both, methyl torsional degrees of freedom.

Trans-n-butyl also possesses effective C_s symmetry based firstly on the delocalized appearance of its ground torsional wavefunction (Figure 3.2). Moreover, the barrier on the electronic potential energy surface is 28 cm^{-1} at the CCSD(T)/ANO1 level of theory. Upon zero-point correction for the orthogonal degrees of freedom, the barrier vanishes, making the symmetric structure 3 cm^{-1} lower in energy than the

electronic minimum. Furthermore, *trans-n*-butyl is left with about 50 cm^{-1} of zero-point energy in the torsional coordinate.

The symmetrical nature of *i*-butyl's electronic potential surface may be surprising. In *i*-butyl and *gauche-n*-butyl, in which the carbon chains are in closer proximity to the radical CH_2 groups, the torsional barriers are more than twice as high as *trans-n*-butyl and more than 1.5x as high as *n*-propyl. The adjacent, symmetrically-oriented methyl groups are likely sufficient to steepen the potential surface and force the *i*-butyl radical into C_s symmetry. We performed computations on cyclopropylmethyl radical at CCSD(T)/ANO1 and found that it also has a C_s symmetry electronic minimum. It is also worth noting that Pacansky found neopentyl radical has a C_s electronic minimum (with HF-SCF) [74]. Neopentyl is analogous to isobutyl with the β hydrogen substituted with a methyl group. It would seem that C_1 symmetry electronic minima do not occur if the carbon-chain branches adjacent to the radical CH_2 group.

The effective structure of the *tert*-butyl radical is a more settled question. It is generally agreed to have C_{3v} symmetry. In agreement with previous theoretical work, we find *tert*-butyl radical to have a C_{3v} symmetry electronic minimum and C_{3h} symmetry at its inversion transition state. It is instructive to compare local-mode predictions made at the C_{3v} minimum and the higher symmetry C_{3h} structure (Fig. 3.9). At the C_{3h} structure, the spectrum is a far poorer match to experiment, providing an additional piece of evidence that *tert*-butyl adopts C_{3v} symmetry. In the C_{3h} simulation, the high frequency region only contains a single band around 2950 cm^{-1}, corresponding to the antisymmetric stretch of the in-plane C-H bonds. The bands centered around 2925 cm^{-1} in the experiment are absent. The bands centered at 2800 cm^{-1} are also missing in the C_{3h} simulation. These features arise from the C-H bonds aligned parallel with the unpaired electron; at the C_{3h} structure, no C-H bonds are aligned in such a way. The profound differences between the C_{3v} and C_{3h} predictions illustrate the sensitivity of the C-H stretches adjacent to a radical site to the torsional orientation [34]. The predictions of the inversion barrier by Schaefer and coworkers are more rigorous than what we have attempted, but we provide our own predictions for the sake of completeness [29]. At CCSD(T)/ANO1, the electronic potential barrier is 517 cm^{-1}, which lowers to 386 cm^{-1} after orthogonal zero-point correction. A further 131 cm^{-1} of harmonic inversion ZPVE gives a

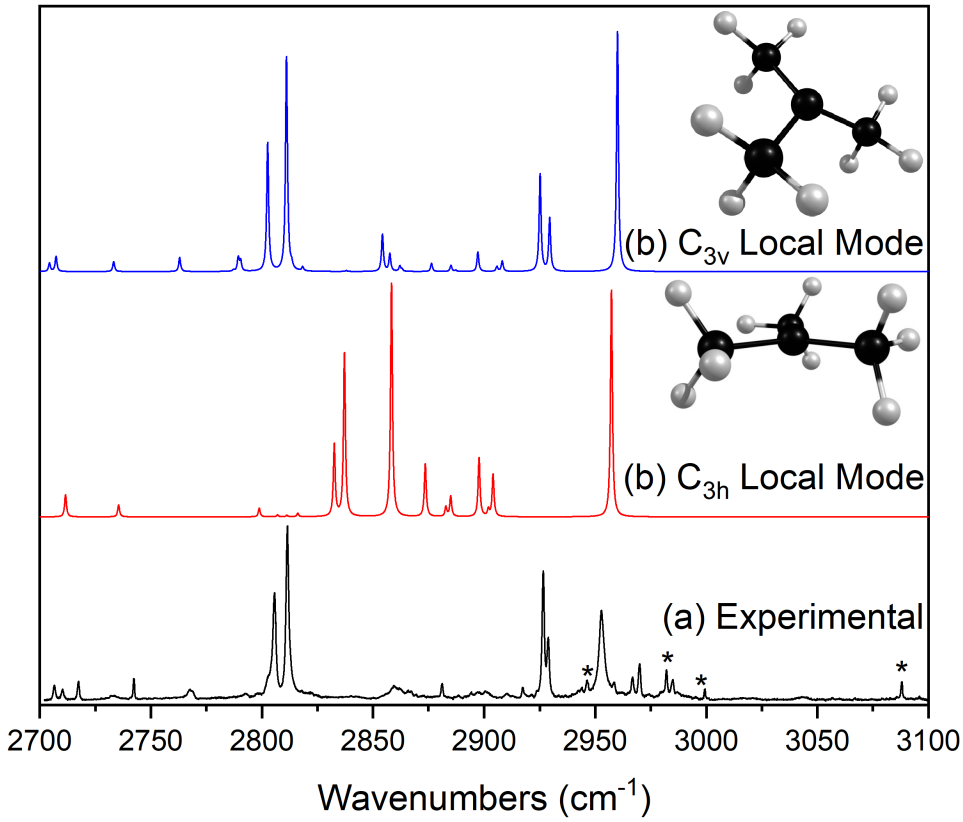

Figure 3.9: Comparison of the experimental spectrum of the *tert*-butyl radical to a local-mode spectrum of the *tert*-butyl radical based on the C_{3h} and C_{3v} stationary points.

v=0 to top-of-the-barrier energy difference of 255 cm^{-1}. This is in very close agreement with Schaefer and coworkers.

3.5.2 Comparisons Between Anharmonic Models

Both computational methods (the semi-empirical local-mode and pure theory VPT2+K) match the experimental spectra of the radicals with reasonable accuracy. One method or the other may match the experimental spectrum of any given radical more closely, but the most prominent spectral features are

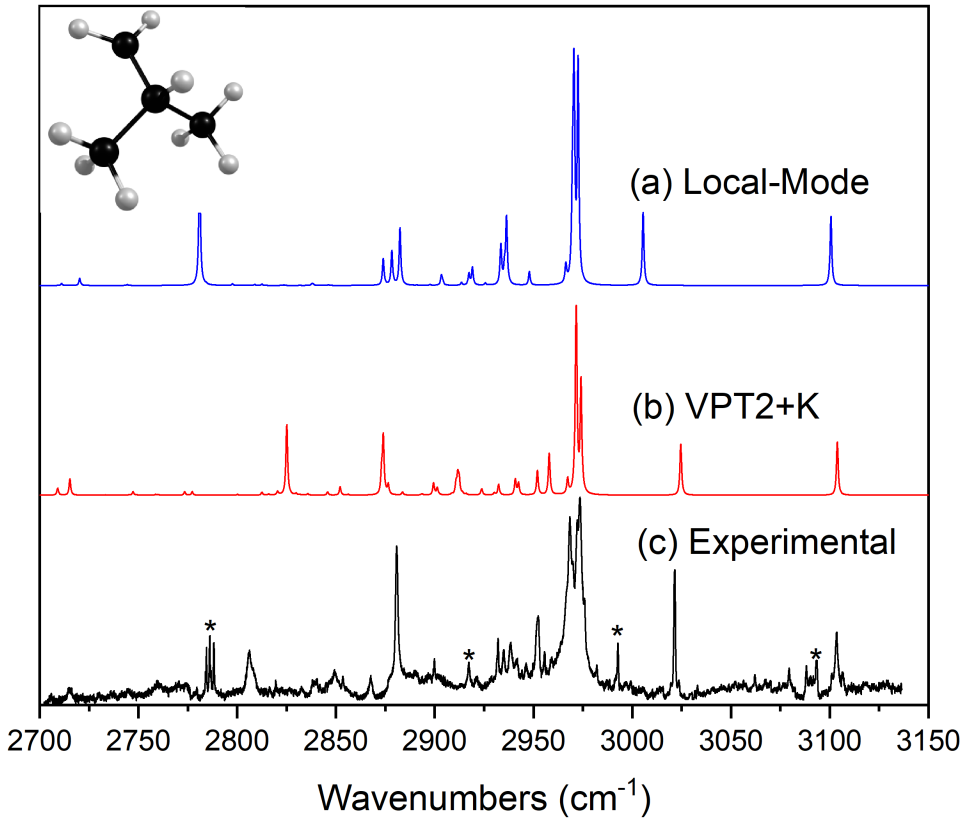

Figure 3.10: The local-mode and VPT2+K computed spectra compared to the experimental spectrum of the *i*-butyl radical. The asterisks mark contamination from isobutene and formaldehyde.

reproduced in both methods. The most illustrative example of this would be *i*-butyl (see Fig. 3.10), where both methods predict the α-CH_2 and γ-CH_3 stretches quite well, with the β-CH stretch qualitatively correct as well. The Supporting Information shows figures containing comparisons between VPT2+K and local mode predictions not shown in the main text.

The VPT2+K method does a particularly good job at predicting the α-CH_x stretches, matching to within 5 cm^{-1} for all those molecules with CH stretches originating at the radical site. The method also reproduces the stretches contributed by the γ and δ-CH_x centers generally well, with the higher frequency

contributions in the vicinity of 2970 cm^{-1} being particularly well-predicted. Agreement with lower-lying stretches is less consistent. This is best illustrated in the straight-chain *n*- and *s*-butyl radicals, which have complex spectra further complicated by the presence of two conformers. This greatly congests the region below 2960 cm^{-1} with a multitude of overlapping features that are not as neatly assignable with relation to the VPT2+K predictions.

Local-mode computations are remarkably good at predicting the spectrum of the *tert*-butyl radical, as shown in Figure 3.11. In this particular case, the local-mode model outperforms the VPT2+K model, particularly with regard to the β-CH stretches. The poor prediction of *tert*-butyl radical's β-CH stretches by VPT2+K is worthy of a detailed analysis. In Figure 3.12, we show the effect of different resonance treatments on the VPT2+K simulation. In the "minimal" resonance treatment, only the Fermi resonances with Martin diagnostic values of 1 cm^{-1} or higher and zeroth-order energy difference of 250 cm^{-1} or smaller are considered active [65]. This criterion leads to a VPT2+K effective Hamiltonian treatment of only the symmetric CH_3 stretches (primarily β-CH motion) and eight doubly-excited HCH bends. The remaining antisymmetric CH_3 stretches are predicted with conventional VPT2. The simulation matches the experiment rather well, and no strong anharmonic mixing occurs among the A_1 or E symmetric methyl stretching fundamentals. The only notable deficiency is the absence of weak overtones and combination bands. This is due to our use of linear harmonic oscillator transition moments; non-resonant multiply-excited transitions have zero intensity.

Lowering the Martin diagnostic threshold to 0.5 cm^{-1} leads to the "moderate" simulation. The lowest frequency, doubly-degenerate, antisymmetric CH_3 stretch fundamental joins the resonance polyads, and its fundamental frequency increases from 2916 to 2933 cm^{-1} through a strong mixing with a combination of antisymmetric bends. The E symmetry symmetric stretch also increases, from 2803 to 2814 cm^{-1} due to coupling with a symmetric bending, i.e., umbrella-like, combination. The frequency of the A_1 symmetric stretch is stable and remains uncoupled, decreasing by only 1 cm^{-1}. The region from 2840 to 2900 cm^{-1} is also sensitive to changes in the resonance treatment; however, again, this is partly a consequence of our intensity treatment. Doubly-excited transitions begin to appear below 2800 cm^{-1} as well.

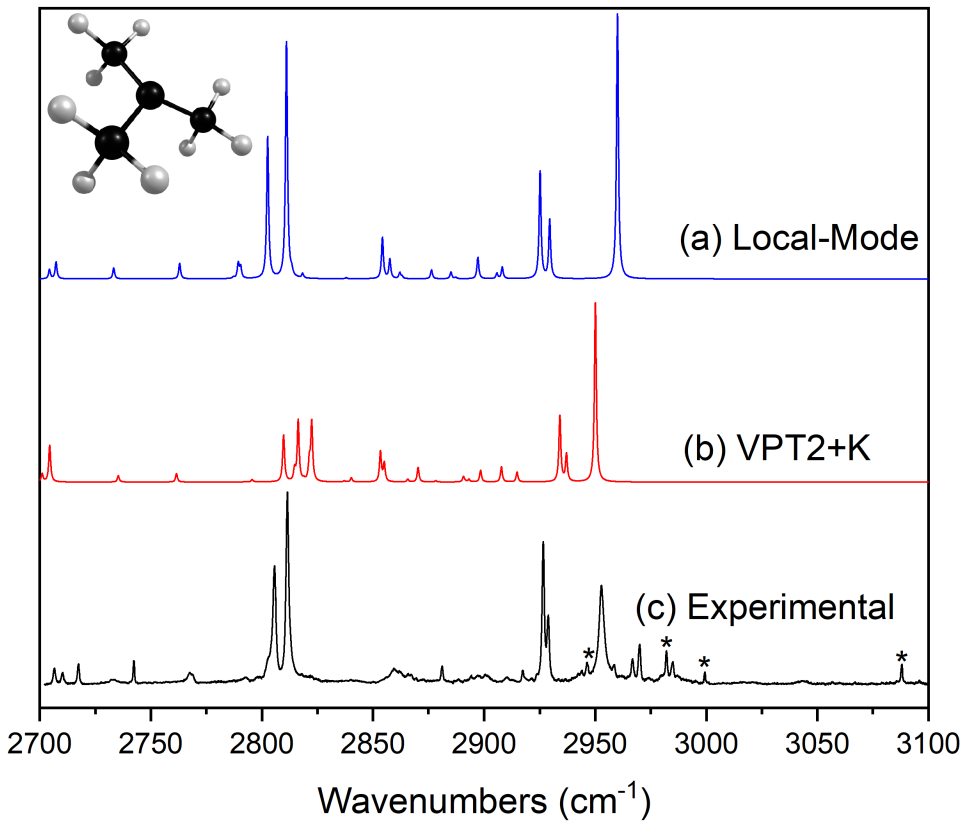

Figure 3.11: CH stretching spectra of the *tert*-butyl radical, with comparison between the VPT2+K and local mode models. The asterisks mark contamination from isobutene.

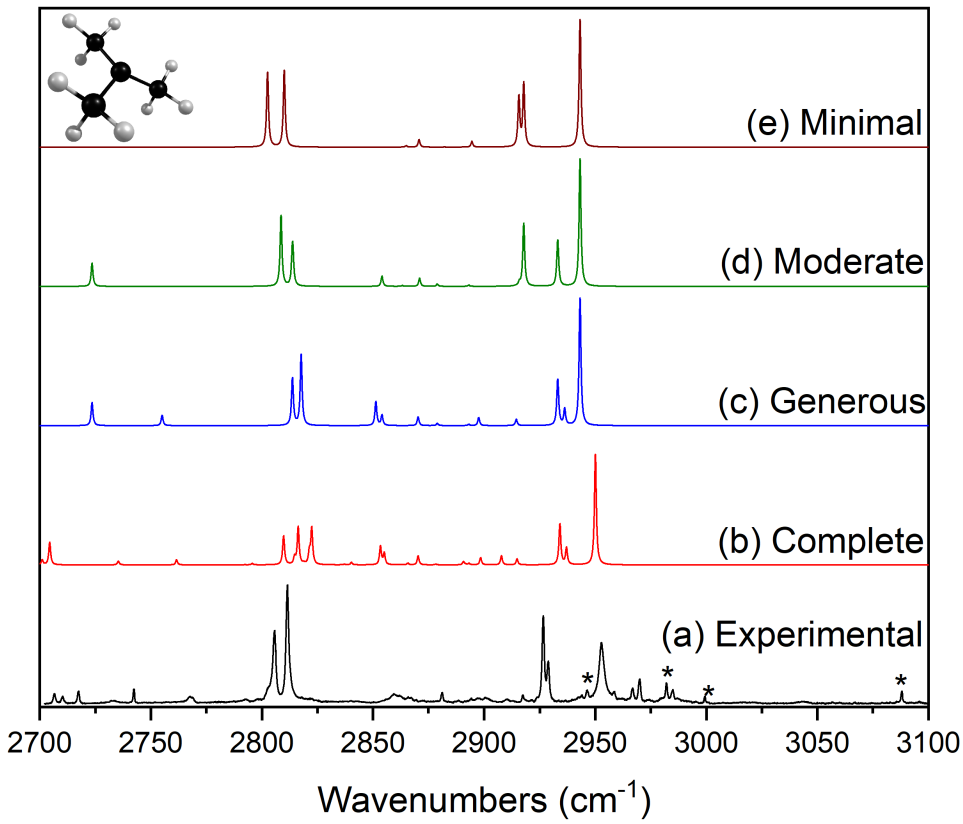

Figure 3.12: Experimental and VPT2+K spectra of the *tert*-butyl radical with varying Martin diagnostic thresholds. Minimal, moderate, and generous correspond to cut-off values of 1.0, 0.5, and 0.1 cm^{-1}, respectively, for identification of Fermi Resonances between singly-excited CH stretches and doubly-excited HCH bends.

At the rather "generous" Martin diagnostic threshold of 0.1 cm^{-1}, many more states join the polyads, including the A_1 symmetry antisymmetric CH_3 stretch. Its frequency increases from the VPT2 value of 2918 cm^{-1} to 2936 cm^{-1}. The E symmetry fundamentals do not change more than 1 cm^{-1}; however, now the A_1 symmetric stretch begins to mix strongly with the overtone of the symmetric CH_3 umbrella and increases in frequency from 2809 to 2818 cm^{-1}. At this point, only the two highest frequencies, the A_2 and E symmetry CH stretching fundamentals are not polyad members, and the A_2 symmetry fundamental is not relevant to infrared spectroscopy. Again, more doubly-excited transitions appear between 2840-2900 and below 2800 cm^{-1}, borrowing small amounts of intensity from the fundamentals in the increasingly complicated polyads.

We then iterated through the nine CH_3 bending normal coordinates, starting from highest frequency and added any new doubly-excited states to the polyads which could be generated from the active bending coordinates. No notable changes to the simulation occurred until the bending states involving the very lowest frequency bending coordinate, of E symmetry, were added to the polyads. Now, the symmetric CH_3 stretches around 2820 cm^{-1} split into three bands, as seen in the "complete" simulation used elsewhere. The A_1 symmetry symmetric CH_3 stretch retains its mixing with the symmetric CH_3 umbrella overtone but begins to further mix with antisymmetric bend + umbrella combinations. It is split approximately into two transitions of equal intensity. The nearby E symmetry fundamental is split similarly, one transition at 2821 cm^{-1} overlapping with the 2822 cm^{-1} A_1 transition. The other E and A_1 components are at 2810 cm^{-1} and 2816 cm^{-1}, respectively, giving the appearance of three bands. Finally, adding the highest frequency stretch to the polyads increases its frequency from 2943 to 2950 cm^{-1}, increasing the splitting of the antisymmetric stretches in closer agreement with experiment.

Consistent with the other VPT2+K simulations, we ignored resonances involving the methyl torsions and the large-amplitude inversion in these predictions. We also find that the influence of Darling-Dennison coupling is consistently small, and it can be neglected in this context without introducing noteworthy error. Clearly, the CH stretching fundamentals of the *tert*-butyl radical are highly sensitive to the resonance treatment. Moreover, it is reasonable to assume that the simulation will also be particularly

sensitive to the quality of the force field. This is in contrast to the α-CH stretches of the other butyl radicals, which are straightforward to model. Perhaps a treatment such as VCI or VMP2+VCI, performed in a basis set of VSCF wavefunctions, would reduce the complexity of the Fermi coupling problem and allow for more reliable predictions.

Based on our *tert*-butyl results, one might be tempted to conclude that minimal resonance treatments in VPT are superior; however, this is not generally true. In the CH stretching spectra of propene and isoprene, for instance, large effective Hamiltonian resonance treatments prove to be essential for reproducing many strong features [62, 63, 75]. Even when combined with VPT2 transition moments, which can confer intensity to non-resonant overtones and combinations, minimal resonance treatments are inadequate [62].

In a previous study of propene, we found that subtle differences in the environment of helium droplets vs. *p*-H_2 matrix were sufficient to qualitatively change the intensities of anharmonically-coupled transitions in two regions of the CH stretching spectrum [75]. The effect of the droplet (or matrix) environment on the anharmonic coupling problem is not straightforward to model and is not accounted for by our computations. Based on the sensitivity of *tert*-butyl's low frequency CH stretching region to the resonance treatment (Fig. 3.12), it would not be surprising to find that the same region of its gas phase (or matrix-isolated) spectrum is qualitatively different in appearance.

Local mode computations of the *trans-n-* and *trans-s*-butyl radicals made at the C_s effective symmetry have yielded spectra that more closely match the experimental spectra than those made at the C_1 structures found when fully relaxing all degrees of freedom in those same radicals (see Figs. 3.3, 3.13, and 3.14). This effect is most visible with respect to the α- and β-CH_X, stretches with the fully relaxed structures underestimating the frequencies found in experimental spectra. This serves as further evidence for the delocalized, symmetrical nature of the wavefunctions at the α-CH_X centers. Sibert and coworkers previously found that the β-CH stretches of alkylbenzyl radicals were profoundly sensitive to their torsional orientation with respect to the unpaired electron on the α-site [34].

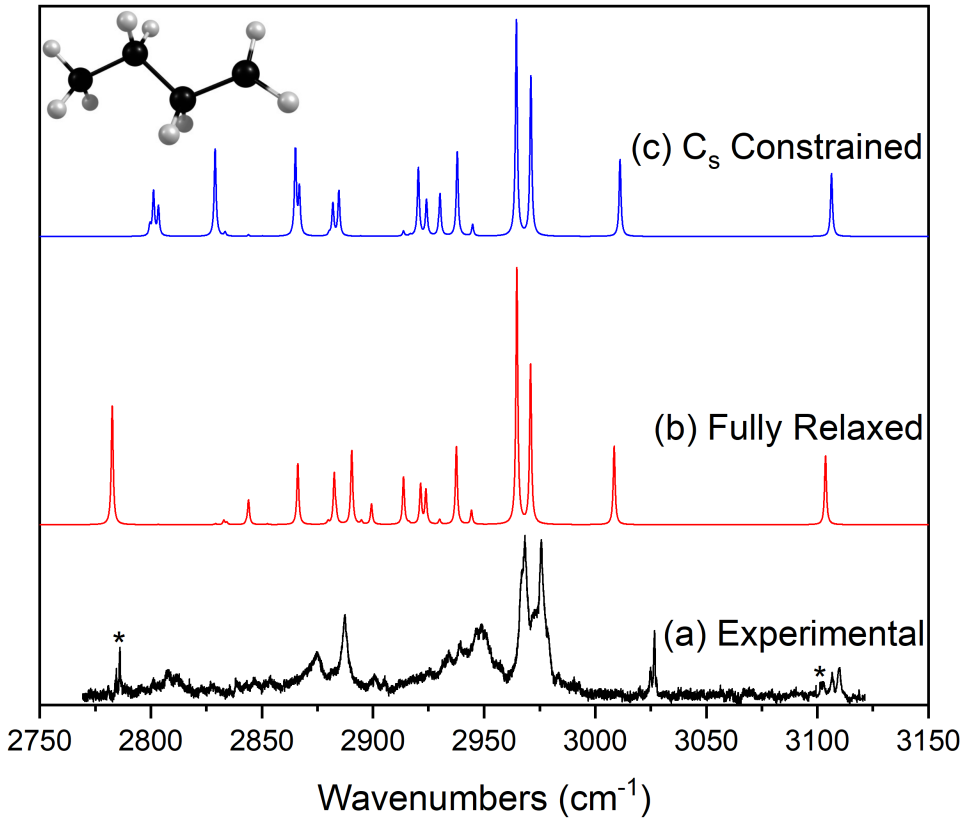

Figure 3.13: A comparison of local mode spectra of the *trans-n*-butyl radical computed at the C_1 local minimum (b) and the effective C_s structure (c). The asterisks mark contamination from 1-butene and formaldehyde.

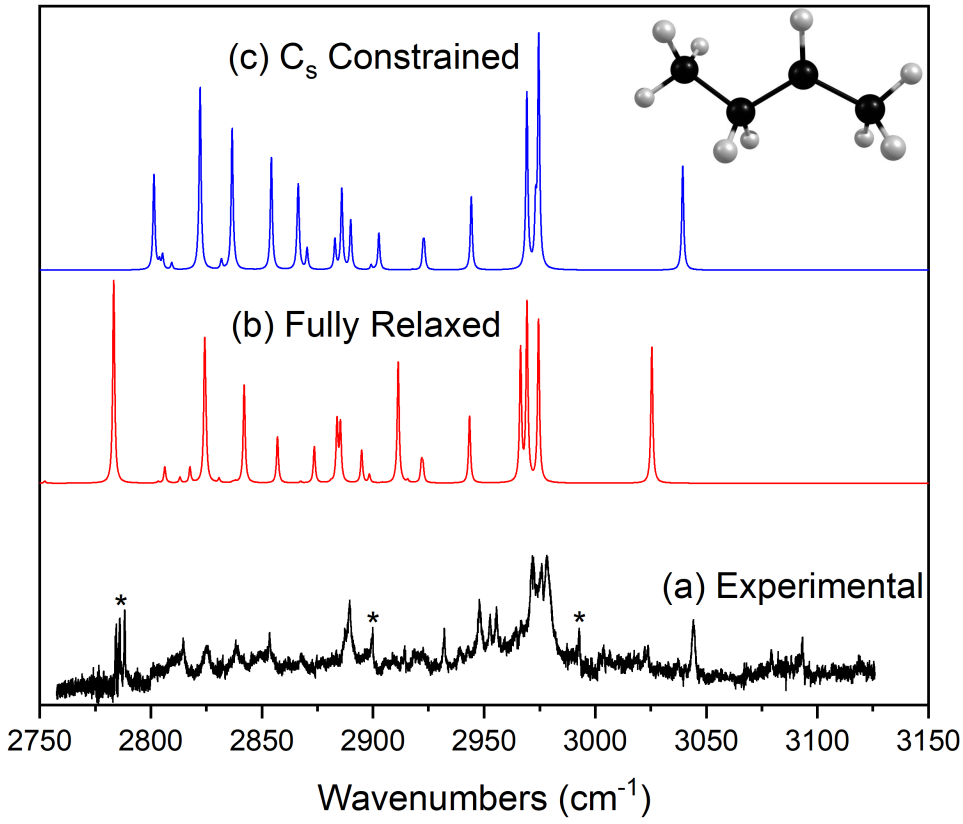

Figure 3.14: A comparison of local mode spectra of the *trans-sec*-butyl radical computed at the C_1 local minimum (b) and the effective C_s structure (c). The asterisks mark contamination from 1-butene and formaldehyde.

The harmonic frequencies corresponding to the α-CH_X stretches of the *trans-s*-butyl and *trans-n*-butyl radicals differ noticeably between their C_s and C_1 geometries. The stretch for the C_s *trans-s*-butyl radical exceeds its C_1 partner by 15 cm^{-1}, while the stretches of C_s *trans-n*-butyl are 3 cm^{-1} higher than the stretches of C_1 *trans-n*-butyl for both the symmetric and antisymmetric bands. There is a 127 cm^{-1} difference between the harmonic and local-mode treated asymmetric α-CH_2 stretch and a 122 cm^{-1} difference between harmonic and local-mode treated symmetric α-CH_2 stretch for the C_1 *trans-n*-butyl radical. This is compared to 127 and 122 cm^{-1} differences for those same respective stretches of the C_s *trans-n*-butyl radical. For the *trans-s*-butyl radical, the differences between harmonic and local-mode treated α-CH stretches is 123 cm^{-1} at both symmetries. These differences between the C_s and C_1 harmonic frequencies, in combination with the negligible (sub 1 cm^{-1}) differences between the anharmonic corrections of the C_s and C_1 species, indicate that the differences in the local mode spectra (see Figs. 3.13 and 3.14) are driven by basic differences in harmonic-level stretching frequencies. In addition, the lack of appreciable difference in the anharmonic correction indicates that the α-CH_X stretches do not greatly couple to any other modes, nor does the coupling change with rotation of the C-H bonds at the radical site.

3.6 Conclusions

Well-resolved infrared spectra were obtained for the *n-, i-, s-,* and *tert*-butyl radicals in the CH stretching region of the mid-infrared. These spectra were obtained with the HENDI technique, with radicals generated through the vacuum pyrolysis of nitrite and azo precursors. This work reports the infrared spectrum of the *s*-butyl radical for the first time. The spectra of all four butyl radicals were assigned by comparison to VPT2+K and local mode effective Hamiltonian methods.

The VPT2+K method has provided a reasonable treatment of alkyl radicals, performing particularly well for the isolated, radical-site CH stretches [23]. Sites directly adjacent to the radical carbon were not modeled as well, though this tendency was also seen with the local mode method. It is often stated that VPT, based on rectilinear coordinates, cannot accurately describe systems that undergo large amplitude motion. Examples of "hard" problems for VPT are numerous. Consider nitromethane and ethyl radical. It

is difficult to say, a priori, whether VPT will fail, as the answer depends not only on the nature of the large-amplitude coordinate(s) but on the degree of their coupling to the small-amplitude coordinates. In some cases, VPT may perform poorly for some transitions but very well for others, e.g., the α-CH_X stretches of alkyl radicals. Another unresolved question concerns the extensibility of large effective Hamiltonian VPT2+K simulations to the CH stretching spectra of larger saturated hydrocarbons. As molecules become larger and the density of states in this region increases, simulations become more sensitive to accidental resonances and consequently sensitive to the quality of the potential energy surface. To prevent spurious anharmonic mixings, it would be desirable to have diagonal matrix elements accurate to perhaps 1 cm^{-1}; however, this is a very difficult standard for molecules of more than a few atoms and is not likely to be achievable on systems like butyl radical for some time.

A local mode treatment based on an affordable (B3LYP/6-311++G**) quadratic force field yielded predicted spectra qualitatively in line with experimental spectra but didn't perform quantitatively for the radical-site CH stretches. This method appears to predict the spectra of the higher-symmetry *i*- and *tert*-butyl radicals more accurately than the straight-chain *n*- and *s*-butyl radicals with multiple conformers. In the case of the *tert*-butyl radical, local mode spectra clearly outperformed the higher-cost VPT2+K computations. We showed that this particular result was mostly fortuitous and related to the high density of vibrational states. When taken in consideration with the local-mode treatments of the propyl and alkylbenzyl radicals [23, 34], the local mode model appears to be a reliable, low-cost treatment of short-chain alkyl radicals. Spectra for all these species were all obtained using the same fixed scaling and coupling parameters from previous studies, suggesting that these parameters are applicable to a wide range of alkyl radical systems.

3.7 Acknowledgements

We acknowledge support from the US Department of Energy (DOE), Office of Science, Office of Basic Energy Sciences (BES) under Contract No. DE-SC0018412.

References

(1) Villano, S. M.; Huynh, L. K.; Carstensen, H.-H.; Dean, A. M. High-Pressure Rate Rules for Alkyl + O2 Reactions. 2. The Isomerization, Cyclic Ether Formation, and β-Scission Reactions of Hydroperoxy Alkyl Radicals. *J. Phys. Chem. A* **2012**, *116*, 5068–5089.

(2) DeSain, J. D.; Taatjes, C. A.; Miller, J. A.; Klippenstein, S. J.; Hahn, D. K. Infrared frequency-modulation probing of product formation in alkyl + O2 reactions. Part IV. Reactions of propyl and butyl radicals with O2. *Faraday Discuss.* **2002**, *119*, 101–120.

(3) Goldsmith, C. F.; Green, W. H.; Klippenstein, S. J. Role of O2 + QOOH in Low-Temperature Ignition of Propane. 1. Temperature and Pressure Dependent Rate Coefficients. *J. Phys. Chem. A* **2012**, *116*, 3325–3346.

(4) Villano, S. M.; Huynh, L. K.; Carstensen, H.-H.; Dean, A. M. High-Pressure Rate Rules for Alkyl + O2 Reactions. 1. The Dissociation, Concerted Elimination, and Isomerization Channels of the Alkyl Peroxy Radical. *J. Phys. Chem. A* **2011**, *115*, 13425–13442.

(5) Moore, K. B.; Turney, J. M.; Schaefer, H. F. The fate of the tert-butyl radical in low-temperature autoignition reactions. *J. Chem. Phys.* **2017**, *146*, 194304.

(6) Franke, P. R.; Moore, K. B.; Schaefer, H. F.; Douberly, G. E. tert-Butyl peroxy radical: ground and first excited state energetics and fundamental frequencies. *Phys. Chem. Chem. Phys.* **2019**, *21*, 9747–9758.

(7) Pacansky, J.; Gutierrez, A. Infrared spectra of the n-butyl and n-pentyl radicals. *J. Phys. Chem.* **1983**, *87*, 3074–3079.

(8) Pacansky, J.; Brown, D. W.; Chang, J. S. Infrared spectra of the isobutyl and neopentyl radicals. Characteristic spectra of primary, secondary, and tertiary alkyl radicals. *J. Phys. Chem.* **1981**, *85*, 2562–2567.

(9) Pacansky, J.; Chang, J. S. Infrared matrix isolation studies on the t-butyl radical. *J. Chem. Phys.* **1981**, *74*, 5539–5546.

(10) Schultz, J. C.; Houle, F. A.; Beauchamp, J. L. Photoelectron spectroscopy of 1-propyl, 1-butyl, isobutyl, neopentyl, and 2-butyl radicals: free radical precursors to high-energy carbonium ion isomers. *J. Am. Chem. Soc.* **1984**, *106*, 3917–3927.

(11) Houle, F. A.; Beauchamp, J. L. Photoelectron spectroscopy of methyl, ethyl, isopropyl, and tert-butyl radicals. Implications for the thermochemistry and structures of the radicals and their corresponding carbonium ions. *J. Am. Chem. Soc.* **1979**, *101*, 4067–4074.

(12) Noller, B.; Maksimenka, R.; Fischer, I.; Armone, M.; Engels, B.; Alcaraz, C.; Poisson, L.; Mestdagh, J.-M. Femtosecond Dynamics of the tert-Butyl Radical, t-C4H9. *J. Phys. Chem. A* **2007**, *111*, 1771–1779.

(13) Seetula, J. A.; Gutman, D. Kinetics and thermochemistry of the sec-butyl + hydrogen bromide ⇌ butane + bromine atom equilibrium. *J. Phys. Chem.* **1990**, *94*, 7529–7533.

(14) Seakins, P. W.; Pilling, M. J.; Niiranen, J. T.; Gutman, D.; Krasnoperov, L. N. Kinetics and thermochemistry of R + hydrogen bromide .dblarw. RH + bromine atom reactions: determinations of the heat of formation of ethyl, isopropyl, sec-butyl and tert-butyl radicals. *J. Phys. Chem.* **1992**, *96*, 9847–9855.

(15) A. Seetula, J.; R. Slagle, I. Kinetics and thermochemistry of the R+HBr⇌RH+Br (R=n-C3H7, isoC3H7, n-C4H9, isoC4H9, sec-C4H9 or tert-C4H9) equilibrium. *J. Chem. Soc. Faraday Trans.* **1997**, *93*, 1709–1719.

(16) Pacansky, J.; Waltman, R. J.; Barnes, L. A. Studies on the Vibrational Frequencies and Intensities of Primary Alkyl Radicals, CH3(CH2)nCH2•, for n = 1-6. *J. Phys. Chem.* **1996**, *100*, 16828–16834.

(17) Schrader, B.; Pacansky, J.; Pfeiffer, U. Calculation of the frequencies and intensities in the infrared spectra of matrix-isolated tert-butyl radical and isobutane. *J. Phys. Chem.* **1984**, *88*, 4069–4073.

(18) Chen, Y.; Rauk, A.; Tschuikow-Roux, E. Structure, barriers for internal rotation, vibrational frequencies, and thermodynamic functions of the sec-butyl radical: an ab initio study. *J. Phys. Chem.* **1990**, *94*, 6250–6254.

(19) Turovtsev, V.; Orlov, Y. D. Study of internal rotation of radical center in n-alkyl radicals. *Russ. J. Gen. Chem.* **2010**, *80*, 749–755.

(20) Claxton, T. A.; Graham, A. M. Ab initio study of propyl radicals. *J. Chem. Soc. Faraday Trans. 2* **1988**, *84*, 121–134.

(21) Allen, W. D.; Bodi, A.; Szalay, V.; Császár, A. G. Adiabatic approximations to internal rotation. *J. Chem. Phys.* **2006**, *124*, 224310.

(22) Li, C.; Agarwal, J.; Wu, C.-H.; Allen, W. D.; Schaefer III, H. F. Intricate internal rotation surface and fundamental infrared transitions of the n-propyl radical. *J. Phys. Chem. B* **2015**, *119*, 728–735.

(23) Franke, P. R.; Tabor, D. P.; Moradi, C. P.; Douberly, G. E.; Agarwal, J.; Schaefer, H. F.; Sibert, E. L. Infrared laser spectroscopy of the n-propyl and i-propyl radicals: Stretch-bend Fermi coupling in the alkyl CH stretch region. *J. Chem. Phys.* **2016**, *145*, 224304.

(24) Brown, A. R.; Franke, P. R.; Douberly, G. E. Helium Nanodroplet Isolation of the Cyclobutyl, 1-Methylallyl, and Allylcarbinyl Radicals: Infrared Spectroscopy and Ab Initio Computations. *J. Phys. Chem. A* **2017**, *121*, 7576–7587.

(25) Chen, Y. K.; Wang, Y. A. First-principles computational studies of the torsional potential energy surface of the sec-butyl radical. *Can. J. Chem.* **2011**, *89*, 1469–1476.

(26) Yoshimine, M.; Pacansky, J. Theoretical studies on the structure of isobutane and the tertiary-butyl radical. *J. Chem. Phys.* **1981**, *74*, 5168–5173.

(27) Pacansky, J.; Yoshimine, M. Theoretical Studies on the Barriers for internal Rotation of the Methyl Groups in the tert-Butyl Radical. *J. Phys. Chem.* **1986**, *90*, 1980–1983.

(28) Carmichael, I. Ab initio molecular orbital calculations on the tert-butyl radical, its isoelectronic neighboring radical ions and their third-row congeners. *J. Phys. Chem.* **1985**, *89*, 4727–4732.

(29) Sokolov, A. Y.; Mittal, S.; Simmonett, A. C.; Schaefer, H. F. Characterization of the t-Butyl Radical and Its Elusive Anion. *J. Chem. Theory Comput.* **2012**, *8*, 4323–4329.

(30) Wood, D. E.; Williams, L. F.; Sprecher, R. F.; Lathan, W. A. Electron paramagnetic resonance of free radicals in an adamantane matrix. IV. Structure of the tert-butyl radical. *J. Am. Chem. Soc.* **1972**, *94*, 6241–6243.

(31) Krusic, P.; Meakin, P. Barrier to pyramidal inversion in the tert-butyl radical by electron spin resonance. *J. Am. Chem. Soc.* **1976**, *98*, 228–230.

(32) Sibert, E. L.; Kidwell, N. M.; Zwier, T. S. A First-Principles Model of Fermi Resonance in the Alkyl CH Stretch Region: Application to Hydronaphthalenes, Indanes, and Cyclohexane. *J. Phys. Chem. B* **2014**, *118*, 8236–8245.

(33) Tabor, D. P.; Hewett, D. M.; Bocklitz, S.; Korn, J. A.; Tomaine, A. J.; Ghosh, A. K.; Zwier, T. S.; Sibert, E. L. Anharmonic modeling of the conformation-specific IR spectra of ethyl, n-propyl, and n-butylbenzene. *J. Chem. Phys.* **2016**, *144*, 224310.

(34) Korn, J. A.; Tabor, D. P.; Sibert, E. L.; Zwier, T. S. Conformation-specific spectroscopy of alkyl benzyl radicals: Effects of a radical center on the CH stretch infrared spectrum of an alkyl chain. *J. Chem. Phys.* **2016**, *145*, 124314.

(35) Morrison, A. M.; Agarwal, J.; Schaefer, H. F.; Douberly, G. E. Infrared Laser Spectroscopy of the CH3OO Radical Formed from the Reaction of CH3 and O-2 within a Helium Nanodroplet. *J. Phys. Chem. A* **2012**, *116*, 5299–5304.

(36) Raston, P. L.; Liang, T.; Douberly, G. E. Infrared spectroscopy of HOOO and DOOO in He-4 nanodroplets. *J. Chem. Phys.* **2012**, *137*, 184302.

(37) Morrison, A. M.; Raston, P. L.; Douberly, G. E. Rotational Dynamics of the Methyl Radical in Superfluid He-4 Nanodroplets. *J. Phys. Chem. A* **2013**, *117*, 11640–11647.

(38) Raston, P. L.; Agarwal, J.; Turney, J. M.; Schaefer, H. F.; Douberly, G. E. The ethyl radical in superfluid helium nanodroplets: Rovibrational spectroscopy and ab initio computations. *J. Chem. Phys.* **2013**, *138*, 194303.

(39) Moradi, C. P.; Morrison, A. M.; Klippenstein, S. J.; Goldsmith, C. F.; Douberly, G. E. Propargyl + O-2 Reaction in Helium Droplets: Entrance Channel Barrier or Not? *J. Phys. Chem. A* **2013**, *117*, 13626–13635.

(40) Leavitt, C. M.; Moradi, C. P.; Acrey, B. W.; Douberly, G. E. Infrared laser spectroscopy of the helium-solvated allyl and allyl peroxy radicals. *J. Chem. Phys.* **2013**, *139*, 234301.

(41) Callegari, C.; Lehmann, K. K.; Schmied, R.; Scoles, G. Helium nanodroplet isolation rovibrational spectroscopy: Methods and recent results. *J. Chem. Phys.* **2001**, *115*, 10090–10110.

(42) Toennies, J. P.; Vilesov, A. F. Superfluid Helium Droplets: A Uniquely Cold Nanomatrix for Molecules and Molecular Complexes. *Angew. Chem. Int. Ed.* **2004**, *43*, 2622–2648.

(43) Choi, M. Y.; Douberly, G. E.; Falconer, T. M.; Lewis, W. K.; Lindsay, C. M.; Merritt, J. M.; Stiles, P. L.; Miller, R. E. Infrared spectroscopy of helium nanodroplets: novel methods for physics and chemistry. *Int. Rev. Phys. Chem.* **2006**, *25*, 15–75.

(44) Stienkemeier, F.; Lehmann, K. K. Spectroscopy and dynamics in helium nanodroplets. *J. Phys. B: At. Mol. Opt. Phys.* **2006**, *39*, R127–R166.

(45) Scheidemann, A.; Schilling, B.; Toennies, J. P. Anomalies in the reactions of helium(1+) with sulfur hexafluoride embedded in large helium-4 clusters. *J. Phys. Chem.* **1993**, *97*, 2128–2138.

(46) Morrison, A. M.; Liang, T.; Douberly, G. E. Automation of an "Aculight" continuous-wave optical parametric oscillator. *Rev. Sci. Inst.* **2013**, *84*, 013102.

(47) Stanton, J. F.; Gauss, J.; Cheng, L.; Harding, M. E.; Matthews, D. A.; Szalay, P. G. CFOUR, Coupled-Cluster techniques for Computational Chemistry, a quantum-chemical program package, With contributions from A.A. Auer, A. Asthana, R.J. Bartlett, U. Benedikt, C. Berger, D.E. Bernholdt, S. Blaschke, Y. J. Bomble, S. Burger, O. Christiansen, D. Datta, F. Engel, R. Faber, J.

Greiner, M. Heckert, O. Heun, M. Hilgenberg, C. Huber, T.-C. Jagau, D. Jonsson, J. Jusélius, T. Kirsch, K. Klein, G.M. KopperW.J. Lauderdale, F. Lipparini, J. Liu, T. Metzroth, L.A. Mück, D.P. O'Neill, T. Nottoli, D.R. Price, E. Prochnow, C. Puzzarini, K. Ruud, F. Schiffmann, W. Schwalbach, C. Simmons, S. Stopkowicz, A. Tajti, J. Vázquez, F. Wang, J.D. Watts and the integral packages MOLECULE (J. Almlöf and P.R. Taylor), PROPS (P.R. Taylor), ABACUS (T. Helgaker, H.J. Aa. Jensen, P. Jørgensen, and J. Olsen), and ECP routines by A. V. Mitin and C. van Wüllen. For the current version, see http://www.cfour.de.

(48) Matthews, D. A.; Cheng, L.; Harding, M. E.; Lipparini, F.; Stopkowicz, S.; Jagau, T.-C.; Szalay, P. G.; Gauss, J.; Stanton, J. F. Coupled-cluster techniques for computational chemistry: The CFOUR program package. *J. Chem. Phys.* **2020**, *152*, 214108.

(49) Raghavachari, K.; Trucks, G. W.; Pople, J. A.; Head-Gordon, M. A fifth-order perturbation comparison of electron correlation theories. *Chem. Phys. Lett.* **1989**, *157*, 479–483.

(50) Hampel, C.; Peterson, K. A.; Werner, H.-J. A comparison of the efficiency and accuracy of the quadratic configuration interaction (QCISD), coupled cluster (CCSD), and Brueckner coupled cluster (BCCD) methods. *Chem. Phys. Lett.* **1992**, *190*, 1–12.

(51) Watts, J. D.; Gauss, J.; Bartlett, R. J. Open-shell analytical energy gradients for triple excitation many-body, coupled-cluster methods: MBPT(4), CCSD+T(CCSD), CCSD(T),and QCISD(T). *Chem. Phys. Lett.* **1992**, *200*, 1–7.

(52) Deegan, M. J.; Knowles, P. J. Perturbative corrections to account for triple excitations in closed and open shell coupled cluster theories. *Chem. Phys. Lett.* **1994**, *227*, 321–326.

(53) Stanton, J. F. Why CCSD(T) works: a different perspective. *Chem. Phys. Lett.* **1997**, *281*, 130–134.

(54) Almlöf, J.; Taylor, P. R. General contraction of Gaussian basis sets. I. Atomic natural orbitals for first- and second-row atoms. *J. Chem. Phys.* **1987**, *86*, 4070–4077.

(55) Meyer, R.; Günthard, H. H. General Internal Motion of Molecules, Classical and Quantum-Mechanical Hamiltonian. *J. Chem. Phys.* **1968**, *49*, 1510–1520.

(56) Lewis, J.; Malloy, T. B.; Chao, T. H.; Laane, J. Periodic potential functions for pseudorotation and internal rotation. *J. Mol. Struct.* **1972**, *12*, 427–449.

(57) Lewis, J.; Laane, J. Periodic potential energy functions with sine and cosine terms. *J. Mol. Spec.* **1977**, *65*, 147–154.

(58) Watson, J. K. Simplification of the molecular vibration-rotation hamiltonian. *Mol. Phys.* **1968**, *15*, 479–490.

(59) Gauss, J.; Stanton, J. F. Analytic CCSD(T) second derivatives. *Chem. Phys. Lett.* **1997**, *276*, 70–77.

(60) Green, W. H.; Jayatilaka, D.; Willetts, A.; Amos, R. D.; Handy, N. C. The prediction of spectroscopic properties from quartic correlated force fields: HCCF, HFCO, SiH+3. *J. Chem. Phys.* **1990**, *93*, 4965–4981.

(61) Schneider, H.; Vogelhuber, K. M.; Schinle, F.; Stanton, J. F.; Weber, J. M. Vibrational Spectroscopy of Nitroalkane Chains Using Electron Autodetachment and Ar Predissociation. *J. Phys. Chem. A* **2008**, *112*, 7498–7506.

(62) Franke, P. R.; Stanton, J. F.; Douberly, G. E. How to VPT2: Accurate and Intuitive Simulations of CH Stretching Infrared Spectra Using VPT2+K with Large Effective Hamiltonian Resonance Treatments. *J. Phys. Chem. A* **2021**, *125*, 1301–1324.

(63) Franke, P. R.; Douberly, G. E. Rotamers of Isoprene: Infrared Spectroscopy in Helium Droplets and Ab Initio Thermochemistry. *J. Phys. Chem. A* **2018**, *122*, 148–158.

(64) Rosnik, A. M.; Polik, W. F. VPT2+K spectroscopic constants and matrix elements of the transformed vibrational Hamiltonian of a polyatomic molecule with resonances using Van Vleck perturbation theory. *Mol. Phys.* **2014**, *112*, 261–300.

(65) Martin, J. M. L.; Lee, T. J.; Taylor, P. R.; François, J.-P. The anharmonic force field of ethylene, C2H4, by means of accurate ab initio calculations. *J. Chem. Phys.* **1995**, *103*, 2589–2602.

(66) Inc., W. R. Mathematica, Version 12, Champaign, IL, 2020.

(67) McCoy, A. B.; Guasco, T. L.; Leavitt, C. M.; Olesen, S. G.; Johnson, M. A. Vibrational manifestations of strong non-Condon effects in the H 3 O+· X 3 (X= Ar, N 2, CH 4, H2O) complexes: A possible explanation for the intensity in the "association band" in the vibrational spectrum of water. *Phys. Chem. Chem. Phys.* **2012**, *14*, 7205–7214.

(68) Califano, S., *Vibrational States*; A Wiley-Interscience publication; Wiley: 1976.

(69) Wang, X.; Turner, W. E.; Agarwal, J.; Schaefer, H. F. Twisted Triplet Ethylene: Anharmonic Frequencies and Spectroscopic Parameters for C2H4, C2D4, and 13C2H4. *J. Phys. Chem. A* **2014**, *118*, 7560–7567.

(70) Mendolicchio, M.; Bloino, J.; Barone, V. General Perturb-Then-Diagonalize Model for the Vibrational Frequencies and Intensities of Molecules Belonging to Abelian and Non-Abelian Symmetry Groups. *J. Chem. Theory Comput.* **2021**, *17*, 4332–4358.

(71) Frisch, M. J. et al. Gaussian 09 Revision A.02, Gaussian Inc. Wallingford CT 2009.

(72) Hoy, A.; Mills, I.; Strey, G. Anharmonic force constant calculations. *Mol. Phys.* **1972**, *24*, 1265–1290.

(73) Wilson, E.; Decius, J.; Cross, P., *Molecular Vibrations: The Theory of Infrared and Raman Vibrational Spectra*; Dover Books on Chemistry Series; Dover Publications: 1980.

(74) Pacansky, J.; Schubert, W. Theoretical calculations for the barriers to internal rotation in the neopentyl and isobutyl radicals. *J. Chem. Phys.* **1982**, *76*, 1459–1466.

(75) Pullen, G. T.; Franke, P. R.; Lee, Y.-P.; Douberly, G. E. Infrared spectroscopy of propene in solid para-hydrogen and helium droplets: The role of matrix shifts in the analysis of anharmonic resonances. *J. Mol. Spec.* **2018**, *354*, 7–14.

Supporting Information

3.7.1 Spectra of Butene Contaminants

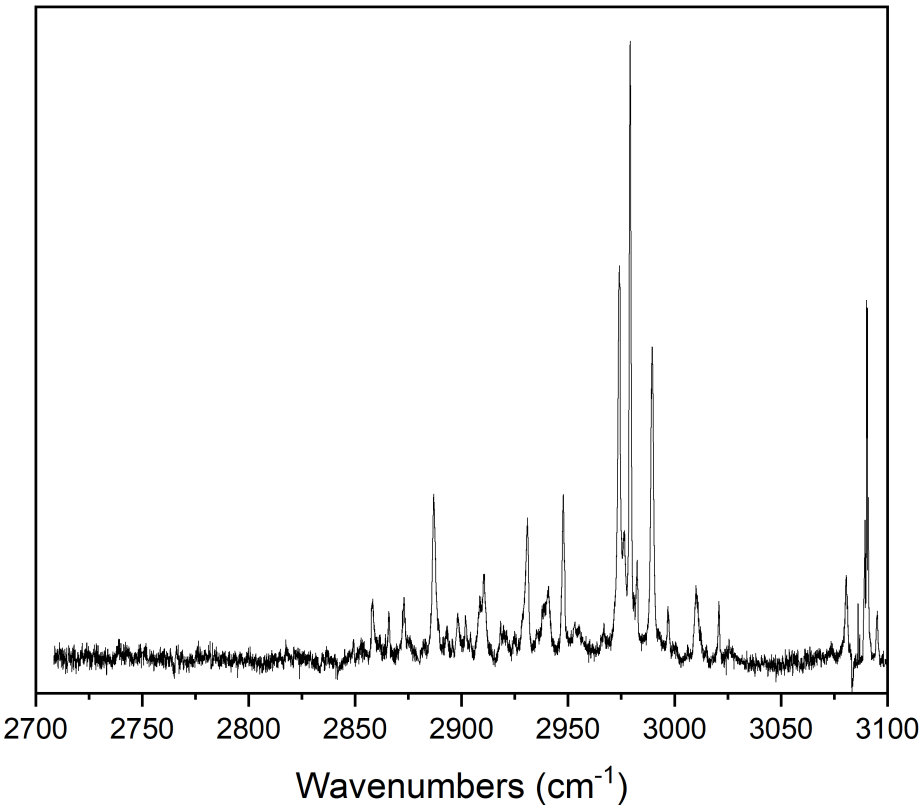

Figure 3.15: CH stretching spectum of 1-butene.

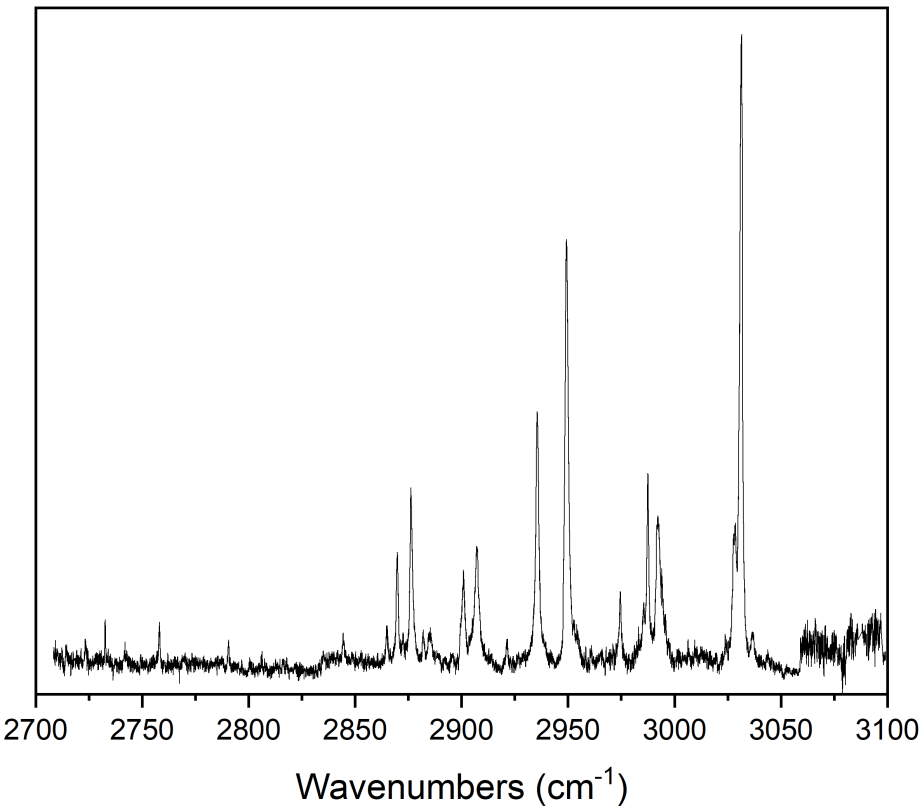

Figure 3.16: CH stretching spectum of *cis*-2-butene.

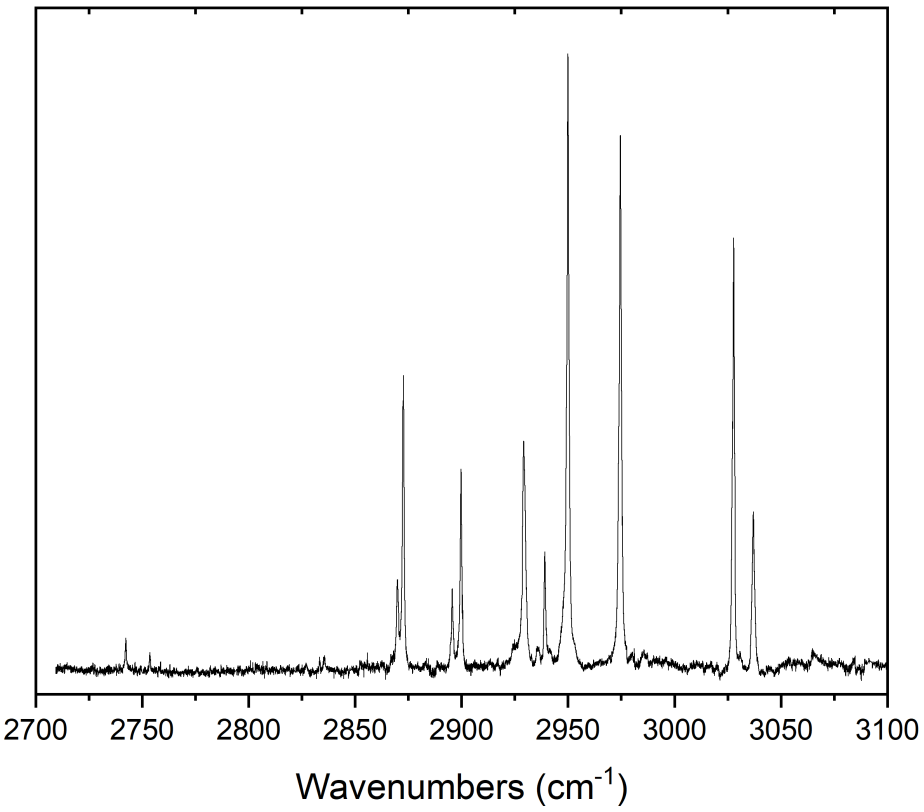

Figure 3.17: CH stretching spectum of *trans*-2-butene.

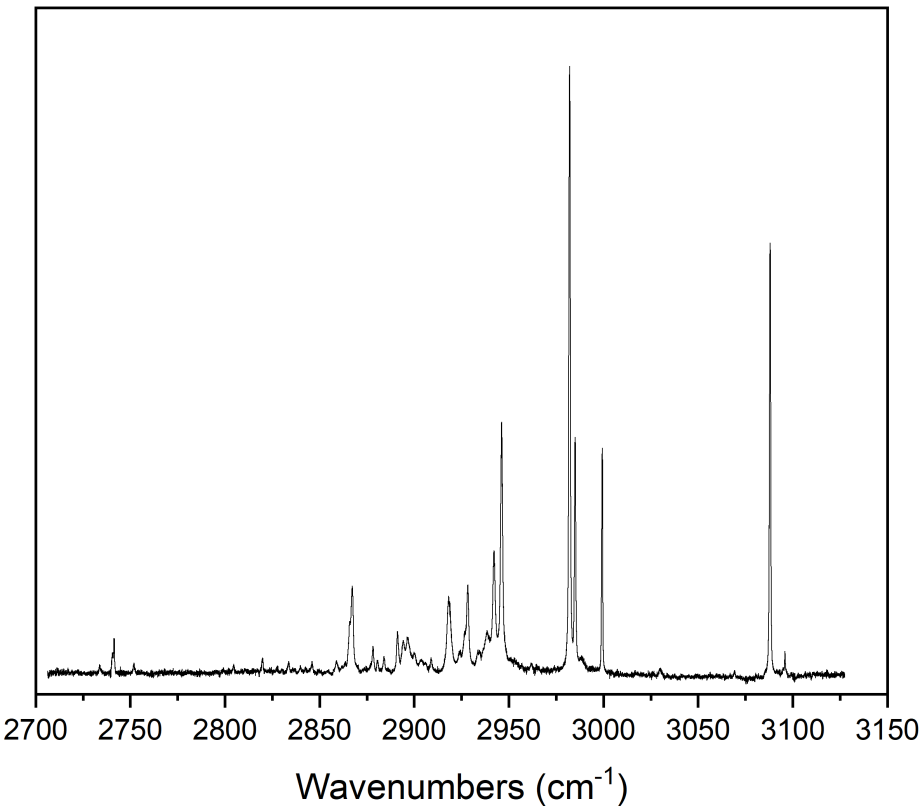

Figure 3.18: CH stretching spectum of isobutene.

3.7.2 Comparisons of anharmonic effective Hamiltonian models

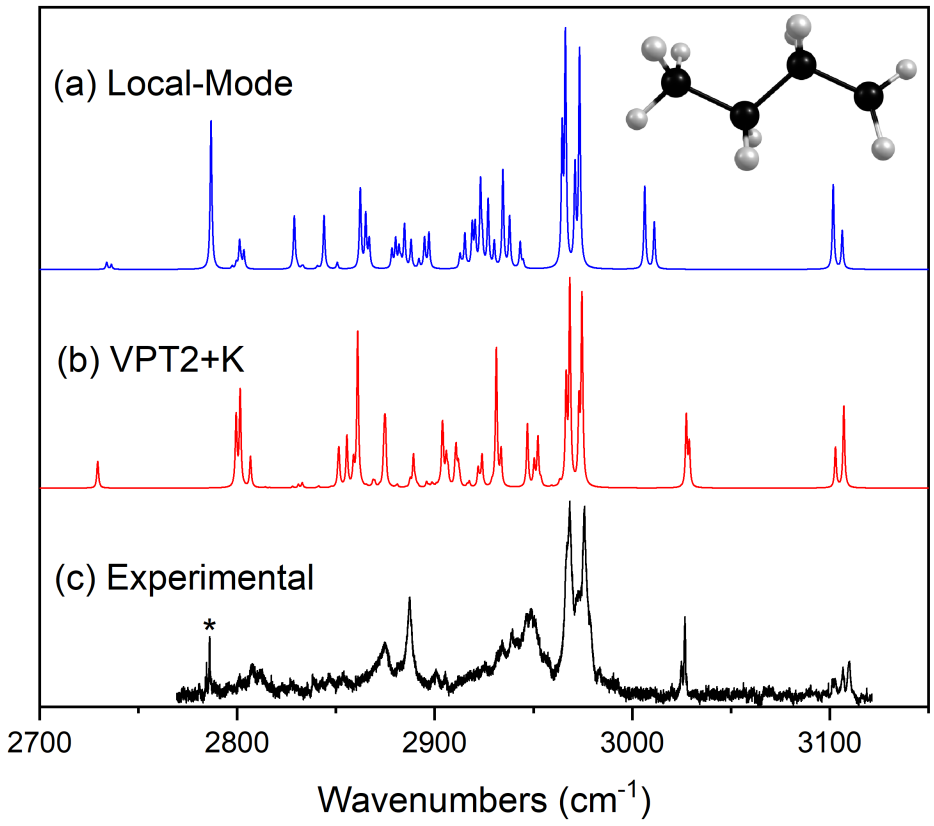

Figure 3.19: CH stretching spectra of the *n*-butyl radical. The asterisks mark contamination from 1-butene and formaldehyde.

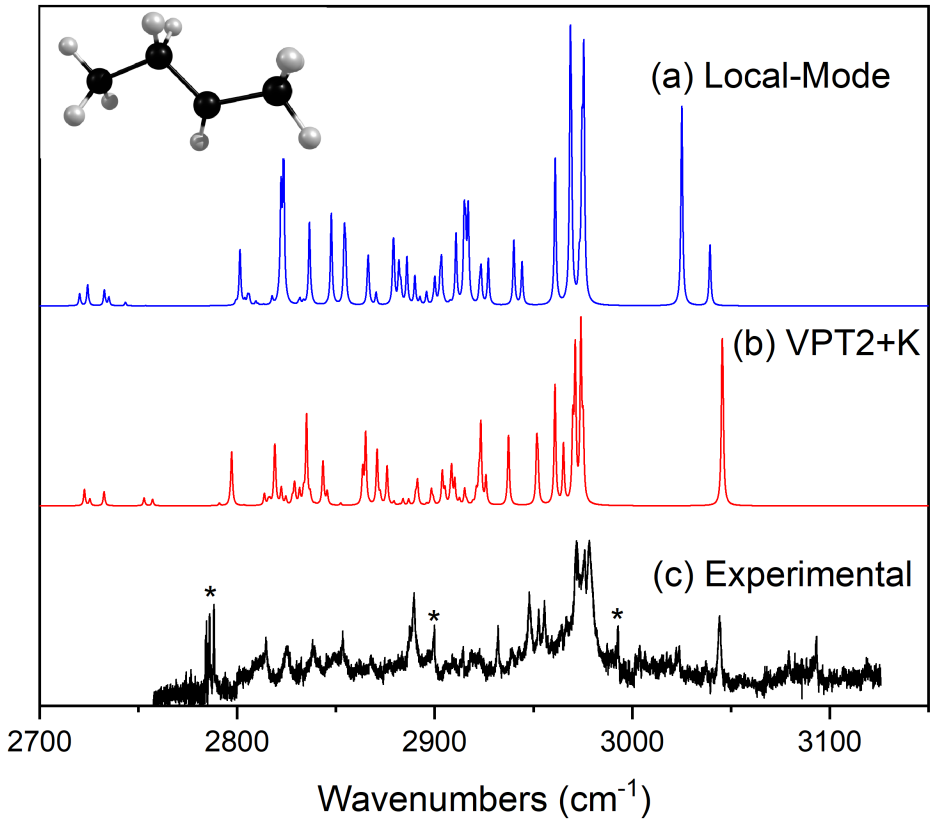

Figure 3.20: CH stretching spectra of the *s*-butyl radical. The asterisks mark contamination from 1-butene and formaldehyde.

3.7.3 Dipole decompositions of local mode effective Hamiltonian models

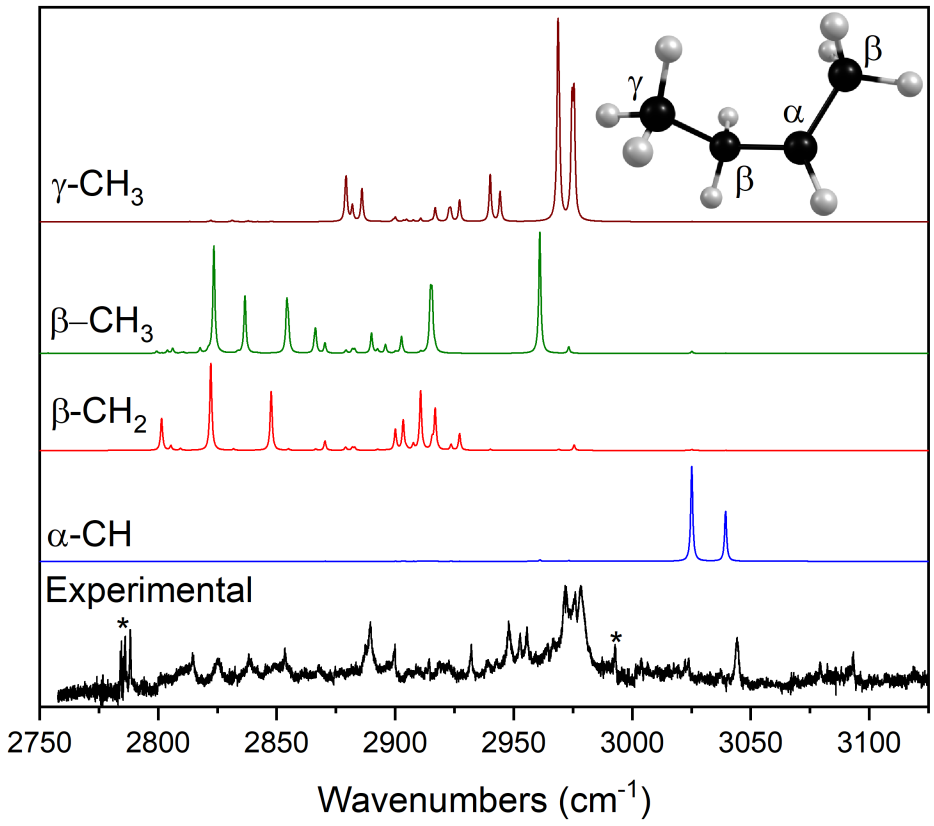

Figure 3.21: Dipole decomposition of the *s*-butyl radical local-mode spectrum. The asterisks mark contamination from 1-butene and formaldehyde.

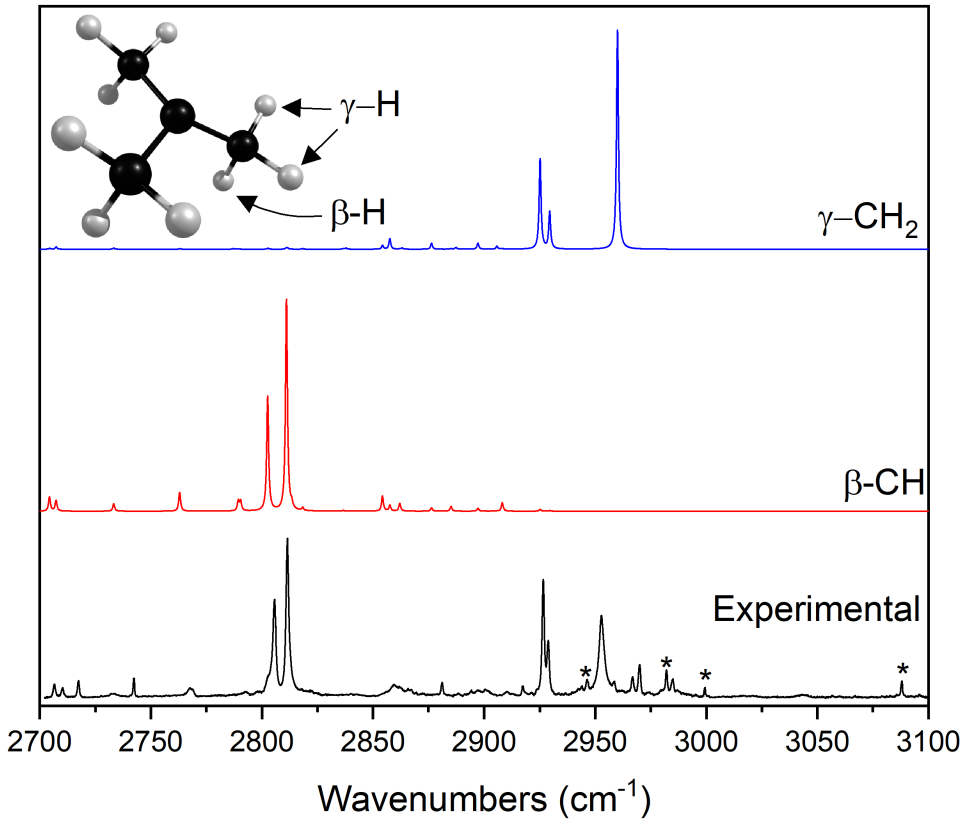

Figure 3.22: Dipole decomposition of the *tert*-butyl radical local-mode spectrum. The asterisks mark contamination from isobutene.

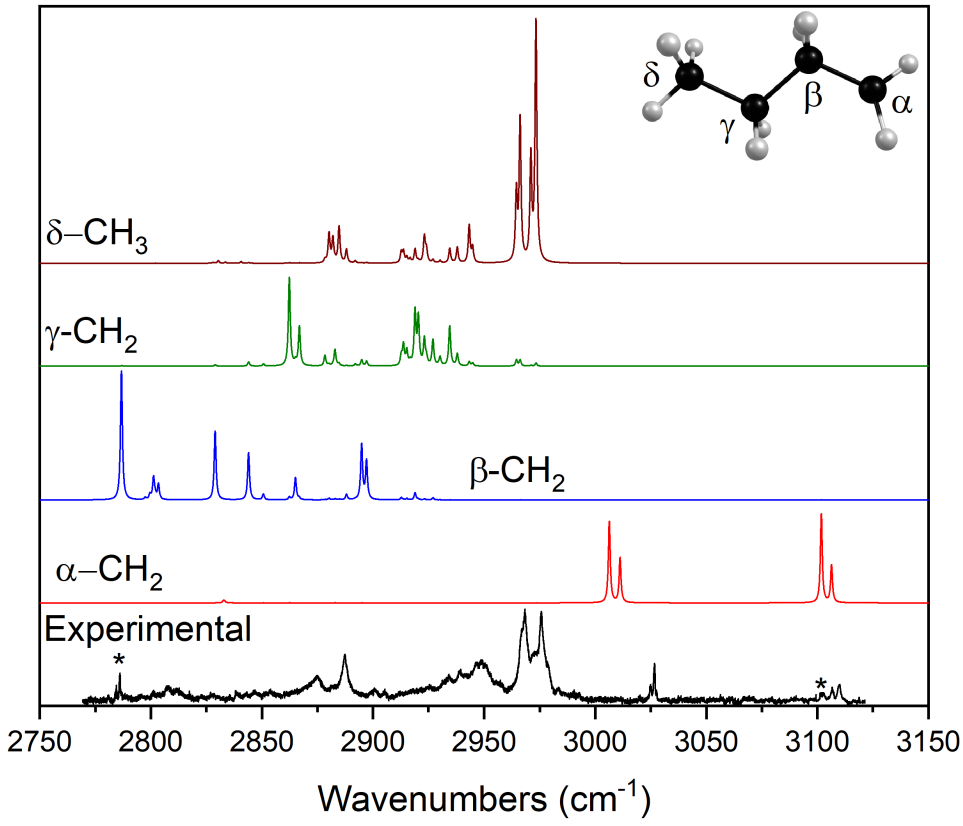

Figure 3.23: Dipole decomposition of the *n*-butyl radical local-mode spectrum. The asterisks mark contamination from 1-butene and formaldehyde.

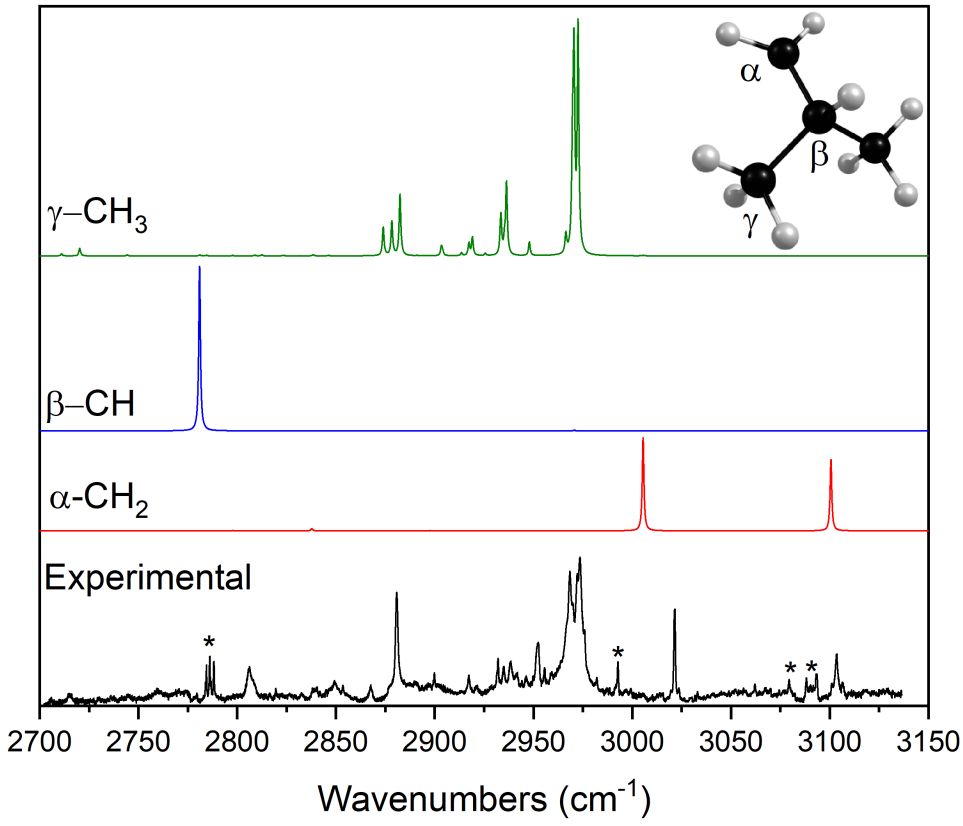

Figure 3.24: Dipole decomposition of the *i*-butyl radical local-mode spectrum. The asterisks mark contamination from isobutene and formaldehyde.

Chapter 4

Monte Carlo Electrostatic Deflection Simulations of Small, HCN-doped Helium Nanodroplets

4.1 Introduction

The superfluid properties of bulk liquid ^{4}He are well-established: as the bulk liquid is cooled, its heat capacity and viscosity drop, quite the opposite of any conventional fluid [1–3]. Landau and Tisza described this as a conversion of a "normal" fluid into a "superfluid," a continuous process in which increasing amounts of the bulk liquid become superfluid as the temperature approaches $0\ K$. The Andronikashvili experiments provided direct evidence of this process, as torsional pendulums suspended in the bulk helium experienced a reduction in rotational inertia as the temperature of the helium bath was lowered from the $4.12\ K$ boiling point of liquid helium [4].

There is evidence that this bulk description is extensible to nanodroplets formed of ^{4}He. Peter Toennies carried out the "Microscopic Andronikashvili Experiment," in which $0.15\ K$ droplets of ^{3}He doped with carbonyl sulfide (OCS) were co-doped with increasing levels of ^{4}He [5]. As increasing amounts of

^{4}He were doped in, the antisymmetric stretch of OCS began to resolve into distinct P- and R-branches. The appearance of these, alongside the absence of a Q-branch indicate that the rotational symmetry of the ^{4}He-solvated OCS is the same as that of free OCS. These rotational effects were attributed to ^{4}He forming a superfluid shell around OCS. Since ^{3}He and ^{4}He have near-identical interaction potentials with OCS, this behavior is attributed to the fact that ^{4}He can participate in long-range exchanges akin to a Bose-Einstein Condensate at the temperature inside the ^{3}He droplet. This is generally in line with computational studies of mixed ^{3}He/^{4}He droplets, doped or otherwise [6].

Theoretical study of small, finite sized clusters of ^{4}He have found evidence of superfluidity in clusters as small as 64 helium atoms [7]. More recent path-integral Monte Carlo [8] and Bosonic DFT [9] studies have examined the interaction between linear rotors such as OCS or hydrogen cyanide (HCN) and small, 64 atom and below, ^{4}He clusters . These studies found that small helium clusters of 1-5 atoms behave as one might expect, with the rotational constant of the system decreasing as helium atoms couple to the rotor. This behavior eventually reversed at a point dependent on the rotor, with the rotational constant returning to some asymptotic limit. Mateo et al. attributed this to the onset of some transition from a classical cluster to a one-dimensional superfluid [9].

This turn-around of the rotational constant in linear rotor-helium clusters has also been observed spectroscopically, in the case of OCS [10, 11]. These studies not only observed the turn-around behavior at 9 ^{4}He atoms clustered around OCS, but an increase in the rotational constant *above* that found in large ^{4}He droplets doped with OCS, and with a periodic oscillation with alternating local maxima and minima approximately every 12 ^{4}He atoms. These studies probed out to 72 ^{4}He atoms, but also found some evidence that OCS-^{4}He clusters with 100 ^{4}He atoms still did not exhibit the behavior seen in proper nanodroplets, in which the moment of inertia of the dopant is scaled by a constant factor of 3 [5].

This gap in experimentation between 100 ^{4}He atoms and a full-size droplet of around 1000 atoms is an area ripe for experimental study. It is not an area that is easy to address with the extant methods, however. Ideally, the behavior of embedded dopants should be probed with a cluster size specific technique across this 100 to 1000 helium atom range. Instead of forming doped clusters of ^{4}He through the expansion of

a seeded beam or through successive pickups with ^{3}He droplets, we propose to create a beam of helium nanodroplets through the standard supersonic expansion into vacuum, dope that beam with hydrogen cyanide and hydrogen cyanide oligomers, and then size-separate that beam with the application of an inhomogeneous electric field. Before constructing an instrument to do such, we have designed a set of simulations to probe the feasibility of separating out such a beam and then detecting it in a size-dependent manner.

4.2 Generating Inhomogeneous Electric Fields

The use of inhomogenous electric or magnetic fields for the manipulation of atoms and molecules is well-established, dating back to the famous Stern-Gerlach experiment of 1922's [12, 13]. Shortly after this, the idea was posited that an inhomogenous electric field might be usable to deflect a beam of polar neutral molecules, given the interaction of the field with the dipole of the molecules [14]. These deflectors follow a common design, in which an approximately semicircular channel is milled into a piece of metal stock and a solid metal cylinder is placed in parallel to this channel at several millimeters offset; static electric potentials are applied to each, generating an inhomogeneous electric field. These deflector types have been used to deflect beams of doped helium droplets, with the aim to determine the dipole of the embedded dopants and to examine reactions ocurring within those droplets [15–18]

Recently, a new geometry of deflector has been developed that is capable of generating greater electric field gradients for the same applied potentials on the electrodes, when compared to the Stern-Gerlach type deflectors. This deflector, termed the "BB" type deflector is constructed of a pair of rounded, milled electrodes which mirror each other [19]. This BB type deflector has been implemented for the deflection of neutral molecular beams [20, 21].

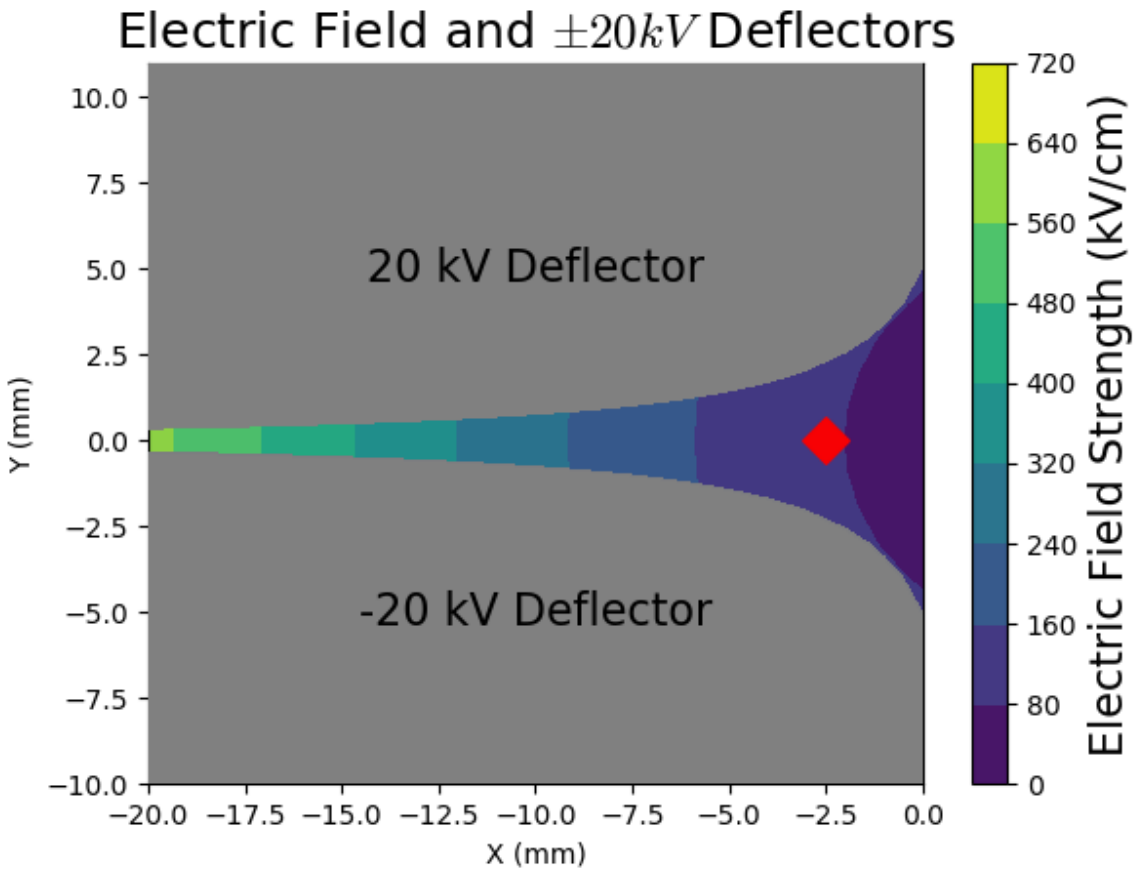

Figure 4.1: The BB-type deflector. The red diamond indicates the point where the beam enters the deflector, moving into the plane of the page.

4.2.1 Deflector Geometry

The physical form of a set of deflectors, of either type, is determined by computing a 2-dimensional electric potential surface and selecting two lines of equipotential. Once these lines of equipotential are selected, the two deflector electrodes are constructed around these. Applying the potentials that these electrodes are designed around to said electrodes produces an electric field in between the two. The two-dimensional potential that governs the potentials (and therefore electric field) is given by the multipole expansion [19]:

$$\Phi(x,y) = \Phi_0 \left(\sum_{n=1}^{\infty} \frac{a_n}{n} (\frac{r}{r_0})^n \cos(n\theta) + \sum_{n=1}^{\infty} \frac{b_n}{n} (\frac{r}{r_0})^n \sin(n\theta) \right) \tag{4.1}$$

In this expansion $r = \sqrt{x^2+y^2}$ and $\theta = \arctan(\frac{y}{x})$ represent the traditional cylindrical coordinates. The r_0 parameter influences the curvature of the deflector, while the Φ_0 parameter scales the strength of the field. The a_n and b_n constants are scaling constants that control the contribution of the $2n$ multipole, e.g. the dipole, quadropole, hexapole, etc. The a_n parameters influence the design of the Stern-Gerlach type deflectors and the b_n parameters influence the BB type deflectors; there is typically no combination of a_n and b_n factors, resulting in purely Stern-Gerlach and purely BB type geometries. The electric field is simple to calculate from the potential and is given by

$$\vec{\epsilon}(x,y) = \vec{\nabla}\Phi(x,y) \tag{4.2}$$

4.3 Interaction of Doped Droplets with Electric Fields

The largest interaction between a doped, uncharged droplet and an electric field comes from the Stark effect on the embedded dopant, as described by

$$W_{Stark} = -\epsilon_{mag} \sum_{g=x,y,z} \mu_g \Phi_{Zg} + \alpha \epsilon_{mag} \Phi_{Zg} \tag{4.3}$$

where ϵ_{mag} represents the magnitude of the electric field, μ_g represents the molecule-fixed intertial components of the permanent dipole moment of the molecule, Φ_{Zg} represents the direction cosine between the molecular axis g and the lab-frame axis Z, and α represents the polarizability tensor of the molecule. In practice, this first term regarding the permanent dipole dominates, with contributions by the polarizability at well below 1% of the total energy, particularly at greater field strengths. The effective dipole, which acts as the primary "handle" by which a droplet is manipulated is given by:

$$\mu_{eff} = -\frac{\partial W_{Stark}}{\partial \epsilon_{mag}} \tag{4.4}$$

The secondary "handle" on the droplet is the dipole induced in the helium of the droplet itself. Two electric fields act to induce this dipole in the helium: the external field generated by the deflector and the field generated by the dipole of the dopant at its center. It is useful to approximate the helium as a hollow shell with a point dipole at its center placed in a uniform electric field. With this approximation, the dipole induced in the helium can be expressed in Gaussian units as

$$\mu_{He} = \left(1 - \frac{a^3}{b^3}\right) \frac{b^3(2\varepsilon+1)(\varepsilon-1)E - 2(\varepsilon-1)^2\mu_{eff}}{(2\varepsilon+1)(\varepsilon+2) - 2\left(\frac{a}{b}\right)^3(\varepsilon-1)^2} \tag{4.5}$$

where a is the inner radius of the shell, b is the outer radius of the shell (the droplet's surface) and ε is the dielectric constant of helium [15]. The outer radius of the droplet is given by $b = 0.22 * N^{1/3}\ nm$, where N is the number of helium atoms in the droplet. At the size of the droplets of interest, the induced dipole is relatively small. For example, a 500 atom droplet, doped with a single HCN molecule with a dipole of $3\ D$, and placed at a point where the electric field is $500\frac{kV}{cm}$, the induced dipole is $0.09\ D$. As dipoles are superposable, the final dipole of the doped droplet is

$$\mu_{drop} = \mu_{eff} + \mu_{He} \tag{4.6}$$

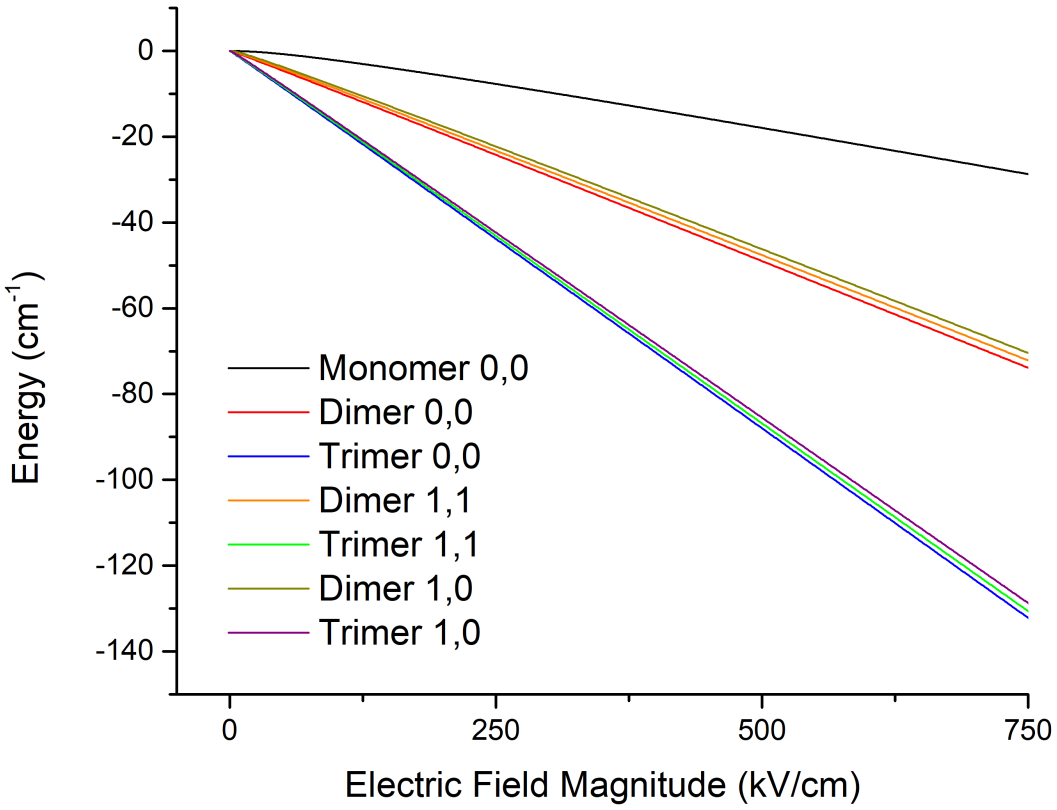

Figure 4.2: Stark energies of select accessible rotational states of HCN oligomers in helium nanodroplets; Numbers refer to the J, M state of the oligomer.

The electric field exerts force on the droplet through this dipole, as

$$\vec{F} = \mu_{drop}\vec{\nabla}\epsilon_{mag} \tag{4.7}$$

From the force, it is a relatively straightforward process to map out changes in a droplet's position over time with a numerical differential equation solver, such as an 4th order Runge-Kutta (RK4) method.

4.4 Droplet Trajectory Simulations

Hydrogen cyanide, as well as its dimer and trimer, were chosen as the dopants for these simulations, due to their well-established properties when solvated in helium droplets. This is due to the strong dipole of all these species, their established rotational constants in helium nanodroplets [22–24], and the known binding energies of the dimer and trimer [25]. The dipoles, helium-solvated rotational constants, and polarizabilities (as computed at the CCSD(T)/ANO1 level with CFOUR [26]) are given below:

	Monomer	Dimer	Trimer
Dipole (D)	2.98	6.0	10.6
Rotational Constant (cm^{-1})	1.18	0.0193	0.0072
$\alpha_{\parallel}$ $(e^2a_0^2/E_h)$	22.52	49.88	81.59
$\alpha_{\perp}$ $(e^2a_0^2/E_h)$	14.02	27.04	39.57

These values were used to variationally compute the Stark energies and induced dipoles of the respective HCN oligomers up to the $J = 20,\ M = \pm 20$ rotational states over the $1 - 1000\ \frac{kV}{cm}$ range of electric field magnitudes using a custom Python script. A subset of these Stark energies are shown in Figure 4.2. Additionally, the solvation energy of HCN in helium droplets was computed across a range of droplets of 50-2500 helium atoms with the Orsay-Paris helium density functional [27], using an array of HCN-helium interaction potentials, as calculated at the CCSD(T)/aug-PVTZ level with CFOUR.

There are three distinct sections of the simulation: the droplet production and pickup section, the deflection section, and a field-free section. The first two regions occupy the vast majority of the simulation and contain all parameters that are randomized.

4.4.1 Initial Droplet Parameters

The initial droplet parameters were selected to mimic those produced by a realistic expansion generated with a vacuum system and cryogenic nozzle construction common to continuous droplet stream experiments. These correspond to a nozzle diameter of $5\ \mu m$, a nozzle temperature of $22\ K$, and a helium

pressure of $45\ bar$ behind the nozzle. These correspond to an average droplet size of 2050 ^{4}He atoms with an average velocity of $363\ m/s$ [28]. Given the vast number of droplets produced in an expansion with these parameters (approximately 10^{14} droplets per second [29]) and the longer timescale of computation (roughly 500 droplets per hour) it is only feasible to simulate a small fraction of a beam within a reasonable computational timeframe. The data presented here represents simulations of 75000 individual droplets, spread between droplets doped with HCN monomers, dimers, and trimers, as well as droplets that did not pick up any dopants in the simulations.

4.4.2 Pickup Parameters

The pickup parameters in this simulation have been optimized to dope an average of one molecule in each droplet. These simulated a $2.0\ cm^{-1}$ long pick-up cell, filled uniformly with $10^{-4}\ torr$ of $300\ K$ of HCN. The dopants are treated as hard spheres for purposes of collision with droplets.

4.4.3 Deflector Parameters

The deflector producing the electric field in these simulations was generally modeled after the BB-type deflector used by the Küpper group to deflect seeded beams of OCS, with some modification [20]. These modifications included an increase of the r_0 parameter and a reduction of the Φ_0 parameter, in order to increase the open space between the deflector electrodes. This was done to provide a wider path for the droplet beam to transit. A two-dimensional image of the deflector is given in Figure 4.1, with the parameters governing deflector geometry listed below:

Deflector Parameter	Value
b_1	1.94
b_2	-4.80
b_3	1.00
r_0	$6.6\ mm$
Φ_0	$15\ kV$
Length	$20\ cm$
Deflector Voltage	$\pm 20\ kV$

4.4.4 Monte Carlo Treatment

The initial sampling parameters of the droplet are fairly straightforward. The droplet size is drawn from a log-normal distribution, based on the nozzle temperature, backing pressure, and nozzle diameter chosen. The velocity is drawn from a linear distribution, centered at the average velocity generated by the aforementioned nozzle parameters. The direction of the droplet's travel is randomly drawn from a solid angle distribution, representing a skimmer of a fixed diameter placed at a fixed distance away from the nozzle.

The pickup of dopants is not a true Poisson distribution at the scale of a single droplet. Rather, the probability of each pickup event is contingent on previous pickups, as each pickup reduces the size of the droplet, reducing the probability of a subsequent pickup. The number of pickups and change in droplet size at each pickup is computed as follows:

1. The length of the pickup region is set
2. A droplet is placed at the start of the pickup region.
3. A path is drawn from a distribution of free paths through the pickup region. This distribution is informed by:
    (a) The size of the droplet

(b) The velocity of the droplet

(c) The temperature and pressure of the dopant gas

4. The droplet is moved along the length of the pickup region by the length of the free path drawn

   (a) If the length of the free path exceeds the length remaining in the pickup region, no pickup occurs and the droplet exits the pickup region.

   (b) If the length of the free path does not exceed the length remaining in the pickup region, a pickup event occurs. This reduces the size of the droplet as a function of the energy the droplet must dissipate to return to $0.4\ K$. The process returns to step 3.

The amount of energy the droplet must dissipate through evaporation at each pickup event is the sum of several factors: the translational, rotational, and vibrational energy of the dopant before it enters the droplet; the size-dependent solvation energy of the dopant in a helium droplet; and the binding energy of multiple dopants, if the droplet contains a dopant before the pickup. This energy dissipation calculation is carried out one atom at a time, as the energy dissipated by the evaporation of a single helium atom is not constant over the range of droplet sizes of interest in the simulation. Energy dissipation can be modeled with the equation [30]:

$$\frac{E(N)}{N} = -5.01 + 12.31N^{-\frac{1}{3}} - 4.14N^{-\frac{2}{3}} \tag{4.8}$$

where the coefficients are in cm^{-1}.

The final randomized parameter governs the rotational state that the dopant is in while the dopant/-droplet system is transiting the deflector. This has direct effects on the force applied to the droplet, as the effective dipole is dependent on the rotational state the dopant occupies. This parameter is updated every $1\ \mu s$ until the droplet exits the $20\ cm$ deflection region, in the manner described below:

1. A Boltzmann distribution of Stark energy levels is generated based on the local electric field magnitude at the droplet's position and the $0.4\ K$ temperature of the droplet.

2. A Stark energy level is drawn from a the Boltzmann distribution.

3. A force vector is calculated based on the droplet's position and the effective dipole of the energy level drawn, as given by Eq. 4.7.

4. The droplet moves through space for the length of the 1 μs time step, based on its previous velocity and the force applied to it, as solved by an RK4 method.

5. After the force has been applied over the time step, the new velocity and position of the droplet are logged and the process repeats.

The selection of a new Stark state from a newly calculated Boltzmann at each time point is done to treat the adiabatic thermal redistribution of energy as the droplet moves through the deflection region. This is necessary for two reasons: first, energy transfer between the droplet and dopant occurs on the nanosecond timescale, far shorter than the time steps the code takes and second, the distribution of Stark energy levels is ϵ_{mag} dependent, with the motion of the droplet taking it to another spatial point with a different ϵ_{mag}.

After the droplet has exited the deflection region, it then travels through a 80 cm field-free region. The droplet's movement in this region is governed by its velocity, as calculated immediately after exiting the deflector. After traversing the field-free region, the droplet's position in space, size, and dopant within are logged for use in predicting the signal along the axis of deflection.

4.5 Signal to Noise Calculation

The signal calculated from the computations is drawn from the kinetic energy that would be imparted onto a detector from droplet collisions. We elected to model beam impacts with a Carolina Instruments bolometer, of the same specifications as those previously used in the Miller lab [29], as such a detector would provide excellent responsivity alongside a very low noise baseline.

The computed signal is drawn from 2 mm wide bins along the axis of deflection. This width was chosen as it matches the aperture of the Carolina Instruments bolometer. The signal in each of these bins is filtered for particles with a specific number of dopants. The sum of the kinetic energy that all particles of that specific doping level would transfer onto the bolometer is taken, then scaled to the number of

droplets that would impact this area over the course of one second. This power flux is then scaled by the $7.2 * 10^5 \ \frac{V}{W}$ responsivity of the bolometer.

The noise native to the bolometer itself is primarily thermal noise, $v_{noise} = \sqrt{4kTRB}$ where k is Boltzmann's constant, T is the temperature of the bolometer, R is the resistance of the bolometer, and B is the bandwitdth of the signal. The particular device here is held at $1.6 \ K$ and $20 * 10^6 \ \Omega$, leading to a r.m.s. noise level of $42 \ nV$. This low noise level (hence the selection of a bolometer as a detector) is necessary, as the droplet beam is dispersed over an appreciable distance along the axis of deflection and the individual droplets are very light, limiting the amount of kinetic energy a collision can impart.

4.6 Results and Discussion

4.6.1 Deflection of Droplets

The simulations carried out predict strong deflection of HCN-doped droplets, with a distinct dependence on droplet size and doping quantity, as shown in Figure 4.3. Deflection can cover a $10 \ cm$ scale, though ranges out to $50 \ mm$ produce usable signal (detailed below). For a specified doping level deflection can be fit to the function

$$g(n) = ae^{b/n} + ce^{d/n} \tag{4.9}$$

where $g(n)$ is the extent of deflection along the primary deflection axis, n is the droplet size in helium atoms, and a, b, c, and d are fitting parameters.

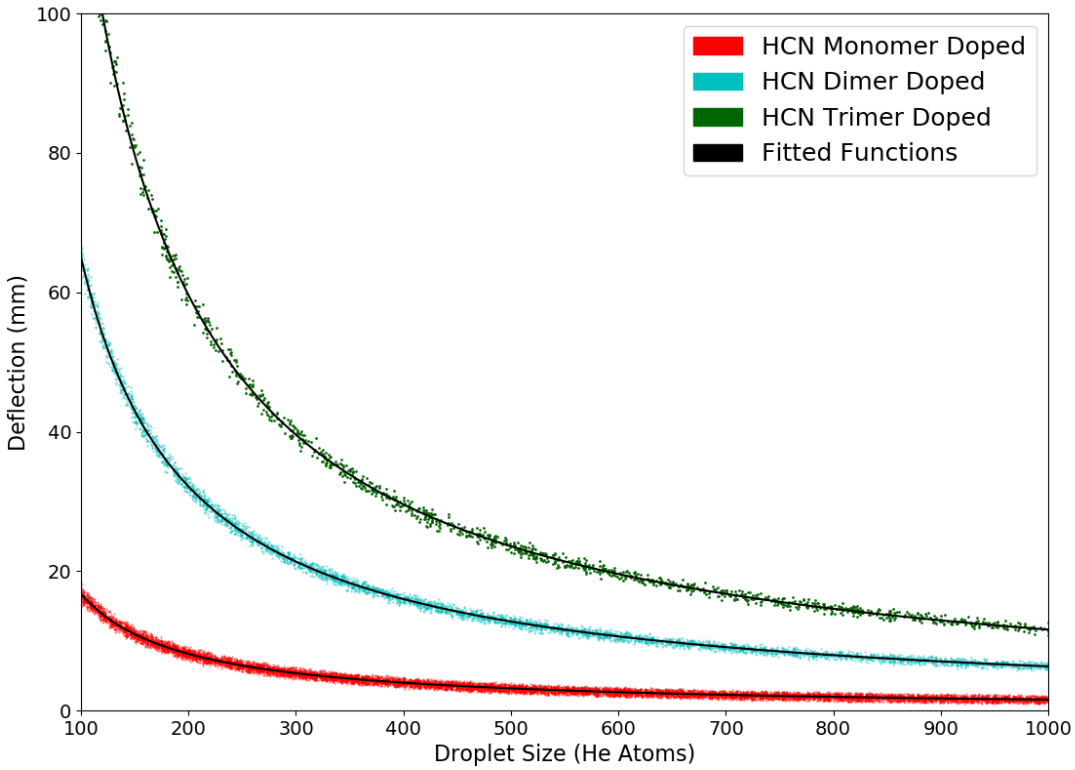

Figure 4.3: Droplet deflection as a function of dopant and droplet size

Predicted Signal-to-Noise

The predicted signal-to-noise, with reference to the thermal noise described in the previous section, shows that significant amounts of signal are expected over the 100-1000 helium atom range. Monomer-doped droplets exhibit strong signal across the 50-2000 atom range, though problems in resolving droplet sizes above 200 atoms may arise, as these sizes are not spread across a particularly wide range (see Figure 4.4). The dimer-doped droplets extend this usable range further, from roughly 150 atoms to 650 atoms, with larger droplets again encountering problems with size-resolution (see Figure 4.5). The trimer-doped droplets complete the range of interest, with droplets in the range of 550 to 1200 atoms accessible at acceptable signal-to-noise levels, without encountering problems with size-resolution (see Figure 4.6).

There are a few methods available to shift the signal to larger or smaller droplets or higher or lower doping levels, without having to change expansion or deflector parameters. Increasing the temperature of the dopant gas will force droplets to dissipate more energy after a pickup, making smaller droplets more prevalent, while decreasing the gas temperature will do the inverse. Increasing the gas pressure would increase the likelihood of doping dimers or trimers into the droplets, at the cost of introducing the possibility of doping HCN tetramers or larger oligomers, which are not accounted for in the current simulations. Another, cruder method to improve the calculated signal-to-noise ratio is to increase the simulated sampling time: since the transfer of energy from the droplets to the detector is continuous (on the timescale of an actual experiment), the signal-to-noise ratio will increase as the square root of the sampling time. As an example, increasing the sampling time from one second to ten seconds would increase the signal-to-noise ratio by a factor of slightly over three.

4.7 Conclusions

With the deflection positions and signal-to-noise ratios determined with the simulations described in the preceding sections, the construction of an experiment to disperse and detect HCN-doped helium droplets over the 100-1000 atom range in a size-dependent manner appears feasible. The parameters

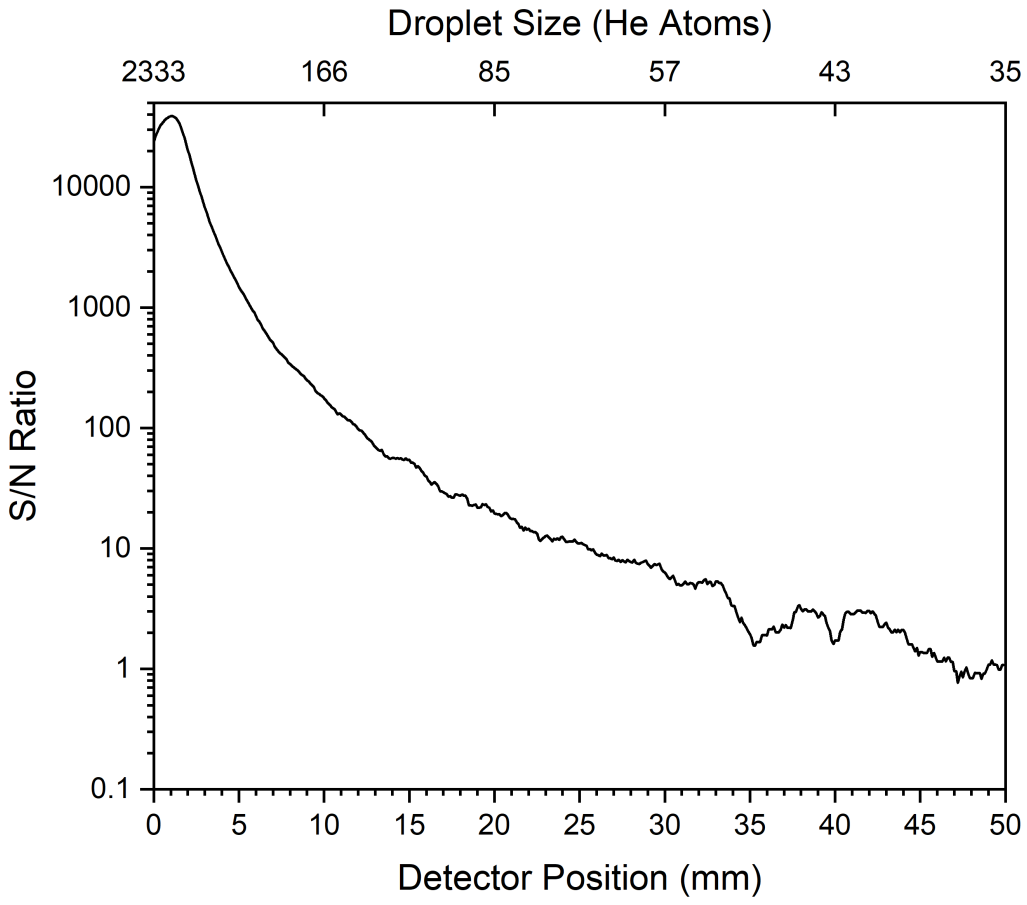

Figure 4.4: Predicted signal to noise ratio of HCN monomer-doped droplets

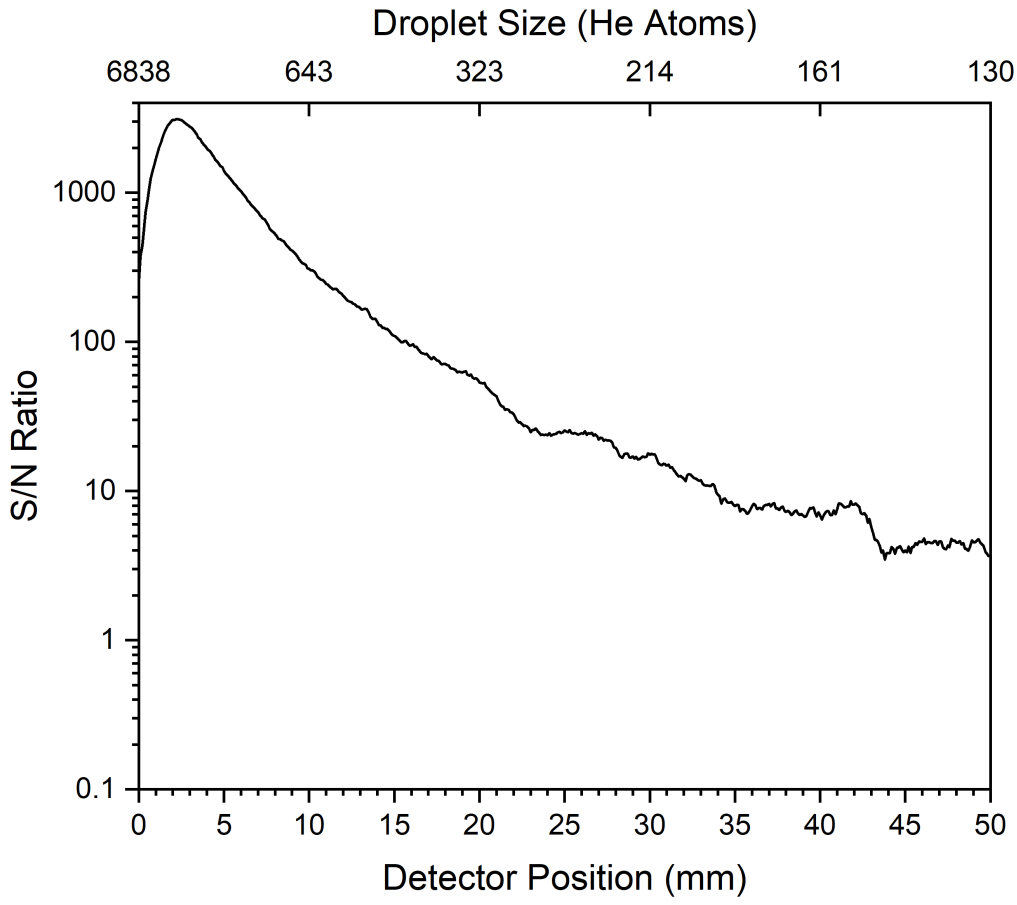

Figure 4.5: Predicted signal to noise ratio of HCN dimer-doped droplets

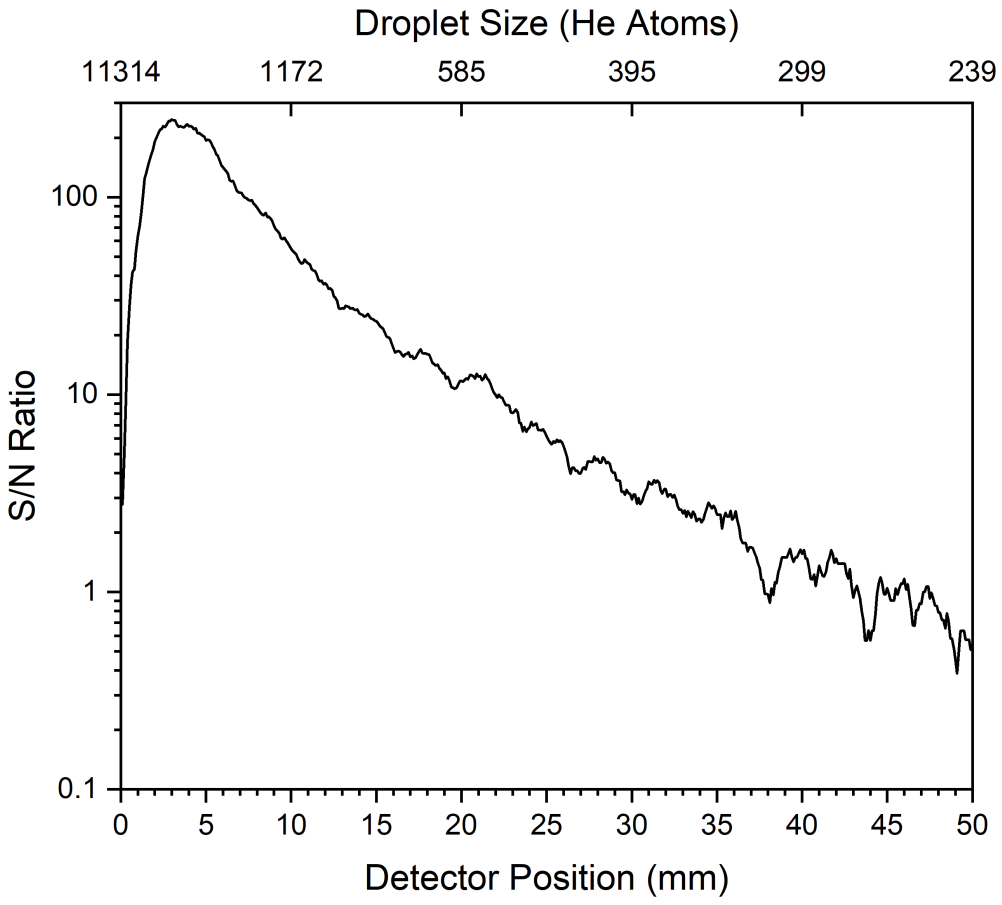

Figure 4.6: Predicted signal to noise ratio of HCN trimer-doped droplets

chosen to model the droplets produced (helium pressure, nozzle size, and nozzle temperature, etc.) are all those readily accessible with traditional droplet beam instruments [31, 32], as are the dopant pressures and pickup methods.

The most difficult portions of the simulation to implement in practice are likely the deflector and detector. There is precedent for the construction of a BB-type deflector [20, 21], though the deflector described in the simulations represents a modified geometry from these previous experiments. The implementation of a translating detector is established for droplet beam deflection experiments using a mass spectrometer as a detector [15, 16, 18], albeit for shorter deflection distances than those calculated here.

Even with these aforementioned departures from previous experimentation, the simulations carried out have shown that it is feasible to deflect doped droplets in a size-dependent, size-specific manner. Constructing or modifying an instrument with a BB-type deflector and a translating bolometer is a tractable task; with the addition of a tunable mid-infrared laser source, it should be possible to record droplet-size specific spectra of doped molecules.

With this experiment it may be possible to examine the effects that droplets of 100 atoms and above have on the ro-vibrational behavior of molecules doped inside them. As droplet sizes increase, one would reasonably expect to see the onset of homogeneous broadening, as larger droplets have a greater density of collective modes (phonons, rotons, ripplons, etc.) with which excitations of the dopant could more rapidly couple [33]. At what droplet sizes this broadening is properly established is still an outstanding question, as is the droplet size at which the rotational constant of a dopant converges to the large-droplet limit.

References

(1) Kapitza, P. Viscosity of liquid helium below the λ-point. *Nature* **1938**, *141*, 74.

(2) London, F. The λ-phenomenon of liquid helium and the Bose-Einstein degeneracy. *Nature* **1938**, *141*, 643–644.

(3) Landau, L. Theory of the Superfluidity of Helium II. *Phys. Rev.* **1941**, *60*, 356–358.

(4) Andronikashvili, E. L.; Malmaladze, Y. G. Quantization of Macroscopic Motions and Hydrodynamics of Rotating Helium II. *Rev. Mod. Phys.* **1966**, *38*, 567–625.

(5) Grebenev, S.; Toennies, J. P.; Vilesov, A. F. Superfluidity Within a Small Helium-4 Cluster: The Microscopic Andronikashvili Experiment. *Science* **1998**, *279*, 2083–2086.

(6) Barranco, M.; Pi, M.; Gatica, S. M.; Hernández, E. S.; Navarro, J. Structure and energetics of mixed ^{4}He-^{3}He drops. *Phys. Rev. B* **1997**, *56*, 8997–9003.

(7) Sindzingre, P.; Klein, M. L.; Ceperley, D. M. Path-integral Monte Carlo study of low-temperature ^{4}He clusters. *Phys. Rev. Lett.* **1989**, *63*, 1601–1604.

(8) Miura, S. Rotational fluctuation of molecules in quantum clusters. II. Molecular rotation and superfluidity in OCS-doped helium-4 clusters. *J. Chem. Phys.* **2007**, *126*, 114309.

(9) Mateo, D.; Gonzalez, F.; Eloranta, J. Rotational Superfluidity in Small Helium Droplets. *J. Phys. Chem. A* **2015**, *119*, 2262–2270.

(10) McKellar, A. R. W.; Xu, Y.; Jäger, W. Spectroscopic Exploration of Atomic Scale Superfluidity in Doped Helium Nanoclusters. *Phys. Rev. Lett.* **2006**, *97*, 183401.

(11) McKellar, A. R. W.; Xu, Y.; Jäger, W. Spectroscopic Studies of OCS-Doped 4He Clusters with 9-72 Helium Atoms: Observation of Broad Oscillations in the Rotational Moment of Inertia. *J. Phys. Chem. A* **2007**, *111*, 7329–7337.

(12) Gerlach, W.; Stern, O. Der experimentelle Nachweis der Richtungsquantelung im Magnetfeld. *Zeitschrift für Physik* **1922**, *9*, 349–352.

(13) Kallmann, H.; Reiche, F. Über den Durchgang bewegter Moleküle durch inhomogene Kraftfelder. *Z. Phys.* **1921**, *6*, 352–375.

(14) Wrede, E. Über die Ablenkung von Molekularstrahlen elektrischer Dipolmoleküle im inhomogenen elektrischen Feld. *Z. Phys.* **1927**, *44*, 261–268.

(15) Merthe, D. J.; Kresin, V. V. Electrostatic Deflection of a Molecular Beam of Massive Neutral Particles: Fully Field-Oriented Polar Molecules within Superfluid Nanodroplets. *J. Phys. Chem. Lett.* **2016**, *7*, 4879–4883.

(16) Niman, J. W.; Kamerin, B. S.; Merthe, D. J.; Kranabetter, L.; Kresin, V. V. Oriented Polar Molecules Trapped in Cold Helium Nanodropets: Electrostatic Deflection, Size Separation, and Charge Migration. *Phys. Rev. Lett.* **2019**, *123*, 043203.

(17) Niman, J. W.; Kamerin, B. S.; Kranabetter, L.; Merthe, D. J.; Suchan, J.; Slavicek, P.; Kresin, V. V. Direct detection of polar structure formation in helium nanodroplets by beam deflection measurements. *Phys. Chem. Chem. Phys.* **2019**, *21*, 20764–20769.

(18) Kamerin, B. S.; Niman, J. W.; Kresin, V. V. Electric deflection of imidazole dimers and trimers in helium nanodroplets: Dipole moments, structure, and fragmentation. *J. Chem. Phys.* **2020**, *153*, 081101.

(19) De Nijs, A. J.; Bethlem, H. L. On deflection fields, weak-focusing and strong-focusing storage rings for polar molecules. *Phys. Chem. Chem. Phys.* **2011**, *13*, 19052–19058.

(20) Kienitz, J. S.; Długołęcki, K.; Trippel, S.; Küpper, J. Improved spatial separation of neutral molecules. *J. Chem. Phys.* **2017**, *147*, 024304.

(21) Johny, M.; Onvlee, J.; Kierspel, T.; Bieker, H.; Trippel, S.; Küpper, J. Spatial separation of pyrrole and pyrrole-water clusters. *Chem. Phys. Lett.* **2019**, *721*, 149–152.

(22) Nauta, K.; Miller, R. E. Stark Spectroscopy of Polar Molecules Solvated in Liquid Helium Droplets. *Phys. Rev. Lett.* **1999**, *82*, 4480–4483.

(23) Nauta, K.; Miller, R. E. Solvent mediated vibrational relaxation: Superfluid helium droplet spectroscopy of HCN dimer. *J. Chem. Phys.* **1999**, *111*, 3426–3433.

(24) Callegari, C.; Lehmann, K. K.; Schmied, R.; Scoles, G. Helium nanodroplet isolation rovibrational spectroscopy: Methods and recent results. *J. Chem. Phys.* **2001**, *115*, 10090–10110.

(25) King, B. F.; Weinhold, F. Structure and spectroscopy of (HCN) n clusters: Cooperative and electronic delocalization effects in C–H· · · N hydrogen bonding. *J. Chem. Phys.* **1995**, *103*, 333–347.

(26) Stanton, J. F.; Gauss, J.; Cheng, L.; Harding, M. E.; Matthews, D. A.; Szalay, P. G. CFOUR, Coupled-Cluster techniques for Computational Chemistry, a quantum-chemical program package, With contributions from A.A. Auer, A. Asthana, R.J. Bartlett, U. Benedikt, C. Berger, D.E. Bernholdt, S. Blaschke, Y. J. Bomble, S. Burger, O. Christiansen, D. Datta, F. Engel, R. Faber, J. Greiner, M. Heckert, O. Heun, M. Hilgenberg, C. Huber, T.-C. Jagau, D. Jonsson, J. Jusélius, T. Kirsch, K. Klein, G.M. KopperW.J. Lauderdale, F. Lipparini, J. Liu, T. Metzroth, L.A. Mück, D.P. O'Neill, T. Nottoli, D.R. Price, E. Prochnow, C. Puzzarini, K. Ruud, F. Schiffmann, W. Schwalbach, C. Simmons, S. Stopkowicz, A. Tajti, J. Vázquez, F. Wang, J.D. Watts and the integral packages MOLECULE (J. Almlöf and P.R. Taylor), PROPS (P.R. Taylor), ABACUS (T. Helgaker, H.J. Aa. Jensen, P. Jørgensen, and J. Olsen), and ECP routines by A. V. Mitin and C. van Wüllen. For the current version, see http://www.cfour.de.

(27) Dalfovo, F.; Lastri, A.; Pricaupenko, L.; Stringari, S.; Treiner, J. Structural and dynamical properties of superfluid helium: A density-functional approach. *Phys. Rev. B* **1995**, *52*, 1193–1209.

(28) Raston, P. L. HeNDS: A program for calculating average Helium NanoDroplet Sizes. *SoftwareX* **2021**, *14*, 100703.

(29) Douberly, G. Infrared Laser Spectroscopy of Dopants In and On Helium Nanodroplets: Rotational and Vibrational Dynamics, Ph.D. Thesis, University of North Carolina Chapel Hill, 2006.

(30) Chin, S. A.; Krotscheck, E. Systematics of pure and doped ^{4}He clusters. *Phys. Rev. B* **1995**, *52*, 10405–10428.

(31) Stienkemeier, F.; Lehmann, K. K. Spectroscopy and dynamics in helium nanodroplets. *J. Phys. B: At. Mol. Opt. Phys.* **2006**, *39*, R127–R166.

(32) Choi, M. Y.; Douberly, G. E.; Falconer, T. M.; Lewis, W. K.; Lindsay, C. M.; Merritt, J. M.; Stiles, P. L.; Miller, R. E. Infrared spectroscopy of helium nanodroplets: novel methods for physics and chemistry. *Int. Rev. Phys. Chem.* **2006**, *25*, 15–75.

(33) Hansen, K.; Johnson, M. D.; Kresin, V. V. Density of states of helium droplets. *Phys. Rev. B* **2007**, *76*, 235424.

Chapter 5

Conclusions and Outlook

The previous chapters of this dissertation have given examples of the use of helium nanodroplets as a matrix for infrared spectroscopy, as well as a set of simulations designed to examine the feasibility of constructing a droplet-size specific probe of nanodroplet properties. The infrared spectroscopy of the butyl radicals in helium droplets probed the application of VPT2+K and semi-empirical local mode treatments to the infrared spectra of small radical systems. The Monte-Carlo simulations of hydrogen cyanide doped nanodroplets in inhomogeneous electric fields explored the size-separation of droplets over the range in which droplet-size effects are not well understood.

5.1 Helium Droplet Infrared Spectroscopy of the Butyl Radicals

All four butyl radicals (*n-*, *i-*, *s-*, and *tert*-butyl) were generated through the vacuum pyrolysis of precursor molecules and doped into helium nanodroplets. The infrared spectra of these radicals, as well the spectra of an assortment of closed-shell spectral contaminants, were obtained over the 2750-3150 cm^{-1} range; this includes the first reported C-H stretching spectra of the *s*-butyl radical. The spectra of these radicals were compared to spectra computed with VPT2+K and local mode effective Hamiltonian methods. The VPT2+K spectra, computed at the CCSD(T)/ANO[1,0] level, were found to model the α-CH stretches of the radicals well, though the CH stretches originating at carbons directly adjacent to the radical cen-

ter were not as accurately modeled. As a whole, the *n-, i-,* and *s*-butyl radicals were well-modeled with the VPT2+K method, though the most intensive treatments of resonances in the *tert*-butyl radical did not model its spectrum as accurately as the other radicals. Despite this caveat, VPT2+K treatments of harmonic spectra have again proven a powerful tool for making spectral assignments of CH stretches in hydrocarbon radicals.

The local mode spectra, computed from B3LYP/6-311++G** quadratic force fields and using the parameters used by Sibert et al., yielded qualitatively correct spectra for all radicals, though the method proved particularly adept at modeling the spectrum of the *tert*-butyl radical, to the extent of outperforming the VPT2+K method. As with the VPT2+K method, local mode computations also encountered difficulty in modeling the CH stretches originating at carbon centers adjacent to the radical centers of the *n-, i-,* and *s*-butyl systems. The results found here, when combined with the results found with the propyl and alkylbenzyl radicals, indicate that the local mode parameters that couple CH stretches to overtones and combinations of HCH scissor modes are generally transferrable to small hydrocarbon radical systems.

5.2 Monte Carlo Electrostatic Deflection Simulations of Small, HCN-doped Helium Nanodroplets

The feasibility of manipulating droplets in a size-dependent manner was investigated with a series of Monte Carlo simulations of doped droplets in inhomogeneous electric fields. A custom Python script was used to variationally compute the Stark energies and dipoles of HCN and small HCN oligomers over an array of electric field strengths. A second custom Python script was used to model the deflection of a beam of HCN-doped helium nanodroplets as they passed through an inhomogeneous electric fields generated by a BB-type deflector. These deflection computations contained a set of Monte Carlo parameters that governed the size of droplets, their dopants, and the rotational state of the dopants inside an electric field. Signal-to-noise calculations were carried out across the axis of beam deflection, using the results of 75000 individual simulated droplets scaled to the droplet flux that would be produced in a physical beam.

These simulations reveal that it is tractable to construct an instrument to separate out a doped droplet beam by size and probe the droplet size-dependent effects on the spectra of the dopants. Deflectors of the type used in the simulations are established and have been used succesfully to manipulate seeded beams of polar molecules . The use of a narrow linewidth, tunable mid-IR laser, such as an Aculight Argos system, should allow for the probe of the ro-vibrational structure of the dopants as a function of droplet size. Obtaining the spectra of dopants in droplets of known size, particularly over the region of 100-1000 helium atoms, should give insight into the onset of homogeneous broadening that occurs from coupling between the ro-vibrational transitions of dopants and the collective modes (phonons, ripplons, rotons, etc.) of the droplet, as well as the convergence of the rotational constant of the dopant to the large-droplet limit.

Appendix A

Stark Energy Calculation Code

Description of Code

This program was written in order to calculate the Stark energies of the linear molecules in an electric field. The values in the input sections correspond to those values for the helium-solvated HCN monomer, dimer, and trimer. This code was used to generate the Stark energies presented in Chapter 4.

This code was written in Python 2.7, using the Numpy 1.13.3 and Sympy 1.2 libraries, though it is fully compatible with Python 3.7+ and all Numpy and Sympy libraries available for Python 3.7+.

```
# Stark energy for linear molecules, including polarizability elements
import numpy as np
import sympy as sp
from sympy.physics.wigner import wigner_3j
# Input maximum electric field magnitude in kV/cm
Emax = 1000
# Input Jmax value
Jmax = 20
# Input permanent dipoles of the oligomers in Debye
muT = [2.98,6.0,10.6]
```

```
# Input rotational constants of the oligomers in cm**-1
BT = [1.18,0.0193,0.0072]
# Input the paralell polarizabilities of the oligomers in atomic units
Ppara = [22.52,49.88,81.59]
# Input the perpendicular polarizabilities of the oligomers in atomic units
Pperp = [14.02,27.04,39.57]

#### End input section

fileopen = "mueff_"
fileclose = ".txt"
for ol in range(0,3,1):
    # Input the permanent dipole of the molecule in debye
    mu = muT[ol]
    # Input B rotational constant in cm**-1
    B = BT[ol]

    # Preallocate space for an array of Stark energies vs electric field strength
    totstates = 0
    for i in range(0,8):
        totstates = totstates + (2*i +1)
    Wdat = np.zeros(shape=(Emax+1,totstates+1))
    for E in np.arange(-1,Emax+1,1):
        q = E*mu*0.0167932
        r = (E**2.0)*(8.312*10**-9)*(Ppara[0]-Pperp[0])
        s = (E**2.0)*(8.312*10**-9)*Pperp[0]
        # Creating the basis
            basis = []
            for k in range(0,Jmax+1):
                for j in range(-k,k+1):
                    basis.append([k,j])
            basis2=np.array(basis, dtype=float)
```

```
x=len(basis)
# Notes for the basis set:
# j indicates the bra, k indicates the ket
# Indices: 0 corresponds to quantum number j, 1 corresponds to quantum number m
# Therefore, [k,0] is equivalent to j, [k,1] is equivalent to m, [j,0] is equivalent to j', and [j,1] is equivalent to m'
# Yes, I know that's confusing. Cut me some slack, I coded this (at least) six years ago when I knew exacly nothing
    ↪ about good coding practice



# Preallocate space for the matrix
starkmatrix = np.zeros(shape=(x,x))
# Populate the matrix with values
for j in range(0,x):
    for k in range(0,x):
        # Compare m' to m
            if basis2[j,1]==basis2[k,1]:
                # Calculate the off-diagonal 1st (y) and 2nd order (yy)
                y = (-1)**(basis2[j,1]+1)*q*np.sqrt((2*basis2[k,0]+1)*(2*basis2[j,0]+1))*wigner_3j(basis2[j
                    ↪ ,0],1,basis2[k,0],(-1)*basis2[j,1],0,basis2[k,1])*wigner_3j(basis2[j,0],1,basis2[k
                    ↪ ,0],0,0,0)
                yy = ((-1)**(basis2[k,1]))*np.sqrt((2*basis2[k,0]+1)*(2*basis2[j,0]+1))*(-1.0*(r/3.0))*
                    ↪ wigner_3j(basis2[j,0],2,basis2[k,0],(-1)*basis2[j,1],0,basis2[k,1])*wigner_3j(basis2[
                    ↪ j,0],2,basis2[k,0],0,0,0)
                # Compare j' to j
                if basis2[j,0]==basis2[k,0]:
                    # Calculte the diagonal rigid rotor (rr) and 2nd order (yy) elements
                    rr = B*basis2[k,0]*(basis2[k,0]+1)
                    yy = -1.0*((r/3.0)+(s/2.0))
                    else:
                        rr=0
                    else:
                        y=0
```

```
                    rr=0
                    yy=0
                # Assign values to positions in the matrix
                starkmatrix[j,k] = rr+y+yy

        # Diagonalize the starkmatrix, assign names ev and ef to lists of eigenvalues and eigenvectors, respectively
        ev, ef = np.linalg.eigh(starkmatrix)
        # Map electric field strength to first column in matrix
        Wdat[E,0] = E
        # Map lowest energy (j=0) state to second column in matrix
        for i in range(1,totstates+1):
            Wdat[E,i] = ev[i-1]

if ol==0:
    olig = "monomer"
elif ol==1:
    olig = "dimer"
elif ol==2:
    olig = "trimer"
filename = olig + '_energies.csv'
np.savetxt(filename,Wdat,delimiter=',')
```

Appendix B

Droplet Simulation Code

Description of Code

This program was written in order to carry out serially carry out a user-defined number of simulations of doped helium nanodroplets travelling through inhomogeneous electric fields. It allows the user to specify the properties of the beam the droplets are drawn from, the deflector that generates the inhomogeneous electric field, and the properties of the dopant that is introduced into the droplet. The values in the input section correspond to the droplet beam, deflector, and pickup parameters described in Chapter 4. This program also relies on the Stark energies of the dopants, as computed with the code from Appendix A, to describe the effective dipole of the dopants in an electric field.

This code was written in Python 2.7, using the Numpy 1.13.3, Sympy 1.2, mpmath 1.0.0, and Scipy 1.0.0 libraries, though it is fully compatible with Python 3.7+ and all Numpy, Sympy, mpmath, and Scipy libraries available for Python 3.7+.

```
import numpy as np
import sympy as sp
import math
import mpmath as mp
```

```
import scipy as scp
from scipy.interpolate import CubicSpline
import pickle as pickle
#### Set the parameters that influence the shape of the deflector
# Define the constants that shape the electrostatic potential
# The potential scaling factor, in V
phio = 15000
# Set radial scaling factor, in m
ro = 0.0066
# Set the dipole/quadropole/hexapole contribution factors
a = [0, 0, 0]
b = [1.94, -4.80, 1.00]
# Set the length of the deflector in the z dimension (in m)
deflen = 0.20
# Set the length of the free drift in the z dimension (in m)
freelen = 0.80
# Set the distance between the nozzle and the deflector (in m)
doffset = 0.20

#### Set the parameters that influence the production of droplets and the pickup of dopants
# Set the mean size of the droplets (in # of He atoms)
Nmean = 2050
# Set the molar mass of the dopant molecule (in amu)
mm = 27.0
# Input the van der Waals b parameter of
vwb = 0.08806
# Set the time step size (in s)
tstep = 0.000001
# Define the velocity of the beam expansion (in m/s)
vexp = 363.0
# Set pick-up-cell length, in cm
pucL = 2.0
```

```
# Set the pressure in the pick-up-cell (in torr)
pucP = 1.0*10**-4
# Set the temperature of the gas in the pick-up-cell (in Kelvin)
pucT = 300.0
# Input the gas-phase rotational constant of the dopant molecule (in cm**-1)
bbar = 1.47822
# Input the normal mode vibrational frequencies for the dopant molecule (in cm**-1, as a list, include degenerate modes in
    ↪ list as many times as they occur)
vfund = [3311.47,711.98,2096.85]


#### Input the net binding energies of each oligomer in kcal/mol as a list. The first two entries will always have values of
    ↪ zero, representing n=0 and n=1
bindeng = [0,0,4.2,9.4,14.97]


#### Input energy values (in kelvin) that handle the solvation of a dopant
#### Input a list of droplet sizes
dsize = [50,100,200,300,400,500,1000,1500,2500]
#### Input a list of free droplet energies
dfree = [-133.45,-349.14,-840.88,-1369.96,-1919.80,-2483.55,-5420.33,-8464.34,-11567.97]
#### Input a list of monomer-doped droplet energies
ddope = [-312.07,-550.10,-1054.33,-1586.85,-2138.83,-2703.17,-5642.18,-8686.43,-11790.08]


#### Input the number of droplets you wish to simulate
ndrop = 2500


#### End input section
#### Don't change anything from here on out unless you wish to change how the script executes


# Convert the input van der Waals parameter into a radius (in m)
Vw = (vwb*0.001)/(6.022*10**23)
rw = np.cbrt(Vw*3.0/(np.pi*4.0))
# Convert the mass of a droplet into SI units (kg)
```

```
ms = mm/(1000*6.022*10**23)
# Convert the pressure in the PUC into SI units (Pa)
pucP = pucP*(101325.0/760.0)
#### Set some physical constants for the droplet and state distributions
# Set the Boltzmann constant in Cm**-1/K
bzc = 0.695034
# Set the temperature of the droplet in K
Tdrop = 0.37
#### The following section sets the parameters of the deflector and analytically determines the potential, field, and field
    ↪ gradients in two dimensions
# Define the dimensions that we're working in
x,y,EEx = sp.symbols('x y EEx')
# Switch to a cylindrical coordinate system
theta = sp.atan2(y,x)
r = sp.sqrt(x**2+y**2)
# Construct the expressions for the potential
# Preallocate memory for voltage calculations
phi = 0
# Calculating the voltages over 2d space
for i in range(len(a)):
    phi = phi + phio*(a[i]/(i+1))*((r/ro)**(i+1))*sp.cos((i+1)*theta)
for i in range(len(b)):
    phi = phi + phio*(b[i]/(i+1))*((r/ro)**(i+1))*sp.sin((i+1)*theta)
Phi = sp.lambdify((x,y),phi,"numpy")


# Find the electric field in both x and y dimensions
Ex = sp.diff(phi,x)
Ey = sp.diff(phi,y)
# Construct the electric field magnitude
Emag = sp.sqrt(Ex**2 + Ey**2)
Em = sp.lambdify((x,y),Emag,"numpy")
```

```
# For the HCN monomer
Starkmonarr = np.loadtxt("monomer_energies.csv",delimiter=",")
Starkmon = []
for i in range(1,np.size(Starkmonarr,1)):
    cs = CubicSpline(Starkmonarr[:,0],Starkmonarr[:,i])
    Starkmon.append(cs)

# For the HCN dimer
Starkdimarr = np.loadtxt("dimer_energies.csv",delimiter=",")
Starkdim = []
for i in range(1,np.size(Starkdimarr,1)):
    cs = CubicSpline(Starkdimarr[:,0],Starkdimarr[:,i])
    Starkdim.append(cs)

# For the HCN trimer
Starktriarr = np.loadtxt("trimer_energies.csv",delimiter=",")
Starktri = []
for i in range(1,np.size(Starktriarr,1)):
    cs = CubicSpline(Starktriarr[:,0],Starktriarr[:,i])
    Starktri.append(cs)



# Take electric field magnitude gradient
Egx = sp.diff(Emag,x)
Egy = sp.diff(Emag,y)
Exx = sp.lambdify((x,y),Egx,"numpy")
Eyy = sp.lambdify((x,y),Egy,"numpy")

#### These functions are for use in the dopant pickup Monte Carlo calculations
#### All of these functions require the use of base SI units, with no exceptions
def crossec(N,a):
        Rdrop = (2.22*10**-10)*np.cbrt(N)
```

```
        return np.pi*(Rdrop+a)**2


def numdens(P,T):
        return P/(T*(1.380649*10**-23))


def rfunc(v,sigma,ndens):
        a = sigma*ndens
        b = np.sqrt(2.0/np.pi)*np.exp(-(v**2)/2.0)
        c = (v+v**-1)*scp.special.erf(v/np.sqrt(2))
        return a*(b+c)


def vfunc(v):
        return (2.0*np.pi)**(-3.0/2.0)*np.exp(-(v**2)/2)


def lstep(v,sigma,ndens):
        return np.random.exponential(v/rfunc(v,sigma,ndens))


# Determine the internal energy of the droplets that will be dissipated by evaporation
# This section determines the internal energy of the molecule the droplet collides with (everything in cm**-1)
Etrans = (3.0/2.0)*(0.6950356)*pucT
Erot = ((0.6950356)*pucT)/bbar
Evib = 0
for i in range(0,len(vfund)):
        Evib += vfund[i]*0.5 + vfund[i]*np.exp(-vfund[i]/((0.6950356)*pucT))/(1-np.exp(-vfund[i]/((0.6950356)*pucT
            ↪ )))
Eint = Erot +Evib


bindeng = np.asarray(bindeng)*349.757


#### This function defines how much energy is dissipated with each evaporated He atom (in wavenumbers)
def engvap(n):
        return (-7.21+17.71*(n**(-1.0/3.0))-5.95*(n**(-2.0/3.0)))*0.6950356
```

```
#### This function defines how much energy is released upon solvation of a dopant (in wavenumbers)
dsize = np.asarray(dsize)
ddope = np.asarray(ddope)*0.6950356
dfree = np.asarray(dfree)*0.6950356
csdop = CubicSpline(dsize,ddope)
csfre = CubicSpline(dsize,dfree)

def solveng(n):
        return csdop(n)-csfre(n)

#### The following section deals with the actual movement of the droplets in space ####
# Set the approximate standard deviation of the droplet distribution
S = 0.65*Nmean
mu = np.log(Nmean)-(0.5)*np.log((S/Nmean)**2 + 1)
sigma = np.sqrt(np.log((S/Nmean)**2 + 1))

for I in np.arange(0,ndrop,1):
    #### Draw the number of helium atoms in the droplet from a lognormal distribution
    N = round(np.random.lognormal(mu,sigma))
    k=0
    #### Draw a velocity for the droplet within 3% of the expansion velocity
    vexp = vexp+vexp*((1.5+1.5)*np.random.random_sample()-1.5)/100.0
    #### This section starts the dopant pickup monte carlo segment
    #Set the initial travel through the pick-up cell (why would this ever be greater than zero?)
    puctrav = 0
    while puctrav<(pucL/100):
        seegma = crossec(N,rw)
        puctrav += lstep(vexp,seegma,numdens(pucP,pucT))
        if k>len(bindeng)-2:
            break
        if puctrav<(pucL/100.0):
```

```
            k += 1
            # The energy here is expressed in cm**-1, thus the strange factors pinned to the last term (converts J to
                ↪ cm**-1)
            Ecoll = Eint + Etrans + solveng(N) + (bindeng[k]-bindeng[k-1]) + ((ms/2*(vexp)**2)*(6.022*10**23)
                ↪ /1000)/0.01196266
            while Ecoll>0:
                if Ecoll<(-1.0*engvap(N)):
                    break
                Ecoll = Ecoll+engvap(N)
                N -= 1
                if N<=0:
                    break

        if N<=0:
            break
    if k == 0:
        # Skip to next droplet
        continue
    elif k > len(bindeng)-2:
        # Skip to next droplet
        continue
    else:
        pass


    if N <= 0:
        continue
    #### Dopant pickup finished

    # Find the dipole of a molecule given its position in the deflector and J,M state. Note that the constant found at the
        ↪ front of the equation is the conversion between wavenumber/(kV/cm) and Debye
    def Mu(a,b,J,M):
```

```
    if k == 1:
        return (0.0167932**-1)*(Starkmon[int(J*(J+1)+J-(2*M))](Em(a,b)/100000,1))
    if k == 2:
        return (0.0167932**-1)*(Starkdim[int(J*(J+1)+J-(2*M))](Em(a,b)/100000,1))
    if k == 3:
        return (0.0167932**-1)*(Starktri[int(J*(J+1)+J-(2*M))](Em(a,b)/100000,1))

# Find the dipole of the droplet, given the droplet size, electric field, and dipole of the dopant
def inddip(N,E,dip):
    b = (10.0**(-7.0))*0.2*N**(1.0/3.0)
    a = 10.0**(-7.0)
    d = 1.057
    ret1 = (1.0-(a**3.0/b**3.0))
    ret2 = (2.0*d+1.0)*(d+2.0)-2.0*((a/b)**3.0)*((d-1.0)**2.0)
    ret3 = (b**3.0)*(2.0*d+1.0)*(d-1)*(E*(10.0/2.998))-2.0*((d-1.0)**2.0)*(dip*10**-18.0)
    return (ret1*(ret3/ret2))/(10.0**-18.0)

# Find energy of a state given position in wavenumbers
def StateEng(a,b,J,M):
    if k == 1:
        return Starkmon[int(J*(J+1)+J-(2*M))](Em(a,b),0)
    if k == 2:
        return Starkdim[int(J*(J+1)+J-(2*M))](Em(a,b),0)
    if k == 3:
        return Starktri[int(J*(J+1)+J-(2*M))](Em(a,b),0)

# Determine the probability of any given (J,M) state at given instrumental conditions (temperature, position in
    ↪ deflector)
def StateProbs(x,y,T):
    if k == 1:
        statlist = len(Starkmon)
    elif k == 2:
```

```
        statlist = len(Starkdim)
    elif k == 3:
        statlist = len(Starktri)
    Partfunc = 0
    for i in range(statlist):
        if k == 1:
            Partfunc = Partfunc + mp.exp(-1.0*((Starkmon[i](Em(x,y)/100000.0,0)-Starkmon[0](Em(x,y)
                ↪ /100000.0,0)))/(T*bzc))
        elif k == 2:
            Partfunc = Partfunc + mp.exp(-1.0*((Starkdim[i](Em(x,y)/100000.0,0)-Starkdim[0](Em(x,y)
                ↪ /100000.0,0)))/(T*bzc))
        elif k == 3:
            Partfunc = Partfunc + mp.exp(-1.0*((Starktri[i](Em(x,y)/100000.0,0)-Starktri[0](Em(x,y)/100000.0,0)
                ↪ ))/(T*bzc))
    statweights = []
    for i in range(statlist):
        if k == 1:
            statwt = mp.exp(-1.0*((Starkmon[i](Em(x,y)/100000.0,0)-Starkmon[0](Em(x,y)/100000.0,0)))/(T*bzc
                ↪ ))/Partfunc
            statweights.append(statwt)
        elif k == 2:
            statwt = mp.exp(-1.0*((Starkdim[i](Em(x,y)/100000.0,0)-Starkdim[0](Em(x,y)/100000.0,0)))/(T*bzc))
                ↪ /Partfunc
            statweights.append(statwt)
        elif k == 3:
            statwt = mp.exp(-1.0*((Starktri[i](Em(x,y)/100000.0,0)-Starktri[0](Em(x,y)/100000.0,0)))/(T*bzc))/
                ↪ Partfunc
            statweights.append(statwt)
    return statweights


# Define a function to return integer square roots
def isqrt(n):
```

```
        x = n
        y = (x + 1) // 2
        while y < x:
            x = y
            y = (x + n // x) // 2
        return x


# Determine a starting J,M state
if k == 1:
        pf = 0
        for i in range(len(Starkmon)):
            pf = pf + mp.exp(-1.0*(Starkmon[i](0,0))/(Tdrop*bzc))
        stateprob = []
        for i in range(len(Starkmon)):
            statprob = mp.exp(-1.0*(Starkmon[i](0,0))/(Tdrop*bzc))/pf
            stateprob.append(statprob)
if k == 2:
        pf = 0
        for i in range(len(Starkdim)):
            pf = pf + mp.exp(-1.0*(Starkdim[i](0,0))/(Tdrop*bzc))
        stateprob = []
        for i in range(len(Starkdim)):
            statprob = mp.exp(-1.0*(Starkdim[i](0,0))/(Tdrop*bzc))/pf
            stateprob.append(statprob)
if k == 3:
        pf = 0
        for i in range(len(Starktri)):
            pf = pf + mp.exp(-1.0*(Starktri[i](0,0))/(Tdrop*bzc))
        stateprob = []
        for i in range(len(Starktri)):
            statprob = mp.exp(-1.0*(Starktri[i](0,0))/(Tdrop*bzc))/pf
            stateprob.append(statprob)
```

```
idx = np.random.choice(len(stateprob),1,p=stateprob)
J = isqrt(idx)
M = math.ceil(((J**2 + 2.0*J)-idx)/2.0)

# Define the expression for the force on a droplet. Note that the constant following the product of the dipole
# and electric field converts the force into N by converting Mu from Debye to Coulomb-Meters
def Fx(x,y,J,M,N):
    return -1.0*(Mu(x,y,J,M)+inddip(N,(Em(x,y)/100000.0),Mu(x,y,J,M)))*Exx(x,y)*(3.335641*(10**-30))
def Fy(x,y,J,M,N):
    return -1.0*(Mu(x,y,J,M)+inddip(N,(Em(x,y)/100000.0),Mu(x,y,J,M)))*Eyy(x,y)*(3.335641*(10**-30))


# Create filename
deflectionnamestart = 'deflection_values_'
velocitynamestart = 'velocity_'
statenamestart = 'JM_states_'
nameend = '.csv'
# This bit just pads the filenames with zeros so they're all of the same length
formatI = '{:0>5d}'.format(int(I))
deflectionfilename = deflectionnamestart+formatI+nameend
velocityfilename = velocitynamestart+formatI+nameend
statefilename = statenamestart+formatI+nameend
# Calculate the total mass of the cluster in kg
mg = (mm*k+N*4.0)*1.66054*(10**(-27))
# Define the starting point of the droplet/cluster
# Randomized over a small area
r = 100*np.random.random_sample()*10**-6
theta = 2*np.pi*np.random.random_sample()
dx = r*np.cos(theta)
dy = r*np.sin(theta)
deltat = np.sqrt(doffset**2+dx**2+dy**2)/vexp
```

```
dz = 0
# Define the starting velocity of the droplet/cluster
vx = dx/deltat
vy = dy/deltat
vz = doffset/deltat
# Calculate the total time for the droplet/cluster to exit the deflector field in the z direction (in s)
texit = deflen/vz
defdat = np.array([[dx,dy,dz]])
veldat = np.array([[vx,vy,vz]])
# Numerically solve the position of the particle via a coupled 1st order ODEs (leapfrog or 4th-order Runge-Kutta
    ↪ method)
for t in np.arange(0, texit, tstep):
    # This is the RK4 method
    k1 = tstep*np.array([[Fx(defdat[-1,0],defdat[-1,1],J,M,N),Fy(defdat[-1,0],defdat[-1,1],J,M,N),0.0]])/mg
    l1 = tstep*np.array([veldat[-1]])
    k2 = tstep*np.array([[Fx((defdat[-1,0]+l1[0,0]/2.0),(defdat[-1,1]+l1[0,1]/2.0),J,M,N),Fy((defdat[-1,0]+l1[0,0]/2.0)
        ↪ ,(defdat[-1,1]+l1[0,1]/2.0),J,M,N),0.0]])/mg
    l2 = tstep*(np.array([veldat[-1]])+k1/2.0)
    k3 = tstep*np.array([[Fx((defdat[-1,0]+l2[0,0]/2.0),(defdat[-1,1]+l2[0,1]/2.0),J,M,N),Fy((defdat[-1,0]+l2[0,0]/2.0)
        ↪ ,(defdat[-1,1]+l2[0,1]/2.0),J,M,N),0.0]])/mg
    l3 = tstep*(np.array([veldat[-1]])+k2/2.0)
    k4 = tstep*np.array([[Fx((defdat[-1,0]+l3[0,0]),(defdat[-1,1]+l3[0,1]),J,M,N),Fy((defdat[-1,0]+l3[0,0]),(defdat
        ↪ [-1,1]+l3[0,1]),J,M,N),0.0]])/mg
    l4 = tstep*(np.array([veldat[-1]])+k3)
    vn = veldat[-1]+(1.0/6.0)*(k1+2*k2+2*k3+k4)
    xn = defdat[-1]+(1.0/6.0)*(l1+2*l2+2*l3+l4)
    # Append updated positions/velocities to respective arrays
    defdat = np.append(defdat,xn,axis=0)
    veldat = np.append(veldat,vn,axis=0)
    # Generate a list of state probabilities at the new position in the deflector
    stateprob = StateProbs(defdat[-1,0],defdat[-1,1],Tdrop)
    # Take a weighted random from the list of states
```

```
    normfac = (np.asarray(stateprob)).sum()
    stateprob[:] = [ind / normfac for ind in stateprob]
    idx = np.random.choice(len(stateprob),1,p=stateprob)
    # Decompose the weighted random index into J and M quantum numbers
    J = isqrt(idx)
    M = math.ceil(((J**2 + 2.0*J)-idx)/2.0)



# Calculate time for droplet to traverse field-free region
tfin = texit + freelen/vz
vx, vy = veldat[-1,0],veldat[-1,1]
for t in np.arange(texit,tfin,tstep):
    xn = np.array([defdat[-1] + tstep*np.array([vx,vy,vz])])
    defdat = np.append(defdat,xn,axis=0)



defdat = np.append([[N,np.NaN,k]],defdat,axis=0)
np.savetxt(deflectionfilename,defdat,delimiter=",")
```